Summer 2020

Using Multispectral Imagery to Interrogate Deposition, Alteration, and Weathering Across Curiosity Rover's Traverse in Gale Crater, Mars

Christina Seeger
christina.seeg@gmail.com

Using Multispectral Imagery to Interrogate Deposition, Alteration, and Weathering Across Curiosity Rover's Traverse in Gale Crater, Mars

By

Christina Seeger

Accepted in Partial Completion
of the Requirements for the Degree
Master of Science

ADVISORY COMMITTEE

Dr. Melissa Rice, Chair

Dr. Brady Foreman

Dr. Allison Pfeiffer

GRADUATE SCHOOL

David L. Patrick, Interim Dean

Master's Thesis

In presenting this thesis in partial fulfillment of the requirements for a master's degree at Western Washington University, I grant to Western Washington University the non-exclusive royalty-free right to archive, reproduce, distribute, and display the thesis in any and all forms, including electronic format, via any digital library mechanisms maintained by WWU.

I represent and warrant this is my original work, and does not infringe or violate any rights of others. I warrant that I have obtained written permissions from the owner of any third party copyrighted material included in these files.

I acknowledge that I retain ownership rights to the copyright of this work, including but not limited to the right to use all or part of this work in future works, such as articles or books.

Library users are granted permission for individual, research and non-commercial reproduction of this work for educational purposes only. Any further digital posting of this document requires specific permission from the author.

Any copying or publication of this thesis for commercial purposes, or for financial gain, is not allowed without my written permission.

Christina Seeger

August 7, 2020

Using Multispectral Imagery to Interrogate Deposition, Alteration, and Weathering Across Curiosity Rover's Traverse in Gale Crater, Mars

A Thesis
Presented to
The Faculty of
Western Washington University

In Partial Fulfillment
Of the Requirements for the Degree
Master of Science

by
Christina Seeger
August 2020

Abstract

Since landing in 2012, the Mars Science Laboratory (MSL) Curiosity rover has explored over 20 kilometers of Gale crater, climbing almost 400 meters in elevation. The fluvio-deltaic, lacustrine, and aeolian sediments in the crater have been well documented by Curiosity's suite of in situ and remote science instruments. Indeed, they have traced chemical trends that track changes in lithology and diagenesis over the study area—though most instruments only sample individual rock, vein, and soil targets at a very small scale. The Mast Camera (Mastcam) has periodically acquired much larger (meter-scale) multispectral, visible to near-infrared observations of outcrops throughout this stratigraphic sequence, with the resulting spectra tracking iron-bearing minerals and oxidation states. These observations contextualize the precise chemistry measured by the other instruments, and allow interpretations about the landscape beyond the rover's traverse. In this study, I present the first comprehensive analysis of the spectral variability observed in Gale crater's rocks with Mastcam, from sol 750 (when Curiosity first entered the lacustrine deposits of the Murray formation at Pahrump Hills) through sol 2755. Characteristic spectral parameters can help distinguish Murray formation from Stimson formation, and also allows comparisons of spectral variations to changes in lithology; the Murray formation is highly variable, and spectral signatures are not always confined to member boundaries. Several of these spectral parameters are also measured by the Chemistry and Camera (ChemCam) instrument, which collects continuous spectra in passive mode from 400-840 nm. A quantitative comparison of the ChemCam passive and Mastcam datasets reveals that ChemCam's higher spectral resolution does not significantly affect measured spectral variability. Mineralogical interpretations based on Mastcam spectra, under the lens of this cross-instrument calibration, are an essential component of the suite of observations needed to characterize the diverse geology of Gale crater.

Acknowledgements

This research was made possible in part by support from the Geological Society of America graduate student grant program and the Western Washington University Geology Department, and would not have been possible without the MSL Participating Science Program and Mars 2020 Mastcam-Z Instrument Investigation. The data presented here were acquired due to the hard work of the MSL Science Team, as well as the calibration crew at Arizona State University; I am grateful to all parties involved for the continuous acquisition of multispectral observations, as well as my requests for specific observations over the course of this study.

The work presented in Sections 1-5 was supported by many contributing coauthors: Melissa Rice, Mason Starr, Cory Hughes, Jim Bell, Danika Wellington, Samantha Jacob, Jeff Johnson, Abby Fraeman, and Samuel Condon. I would like to offer particular thanks to Jeff Johnson and Abby Fraeman for providing ChemCam passive data and guidance, Sam Condon for his diligent help maintaining our database, and Mason Starr for writing an exceptional software program (and providing continued tech support long after graduating). I would also like to acknowledge Ashwin Narayan, whose mathematical and statistical expertise were invaluable in developing the inter-instrument comparison methodology presented here; not only was I inspired by his eagerness to tackle problems far outside his field of study, but I was absolutely delighted by the opportunity to collaborate scientifically with someone whose friendship and support have been instrumental in my success as a graduate student.

Thank you to the Western Mars Lab, which gave me so much scientific and emotional support; I have treasured my time in this research group, and am so grateful for the community we have built and maintained virtually. Thank you also to my WWU cohort (and officemates), for the friendship, commiseration, and memes that were necessary to get my research done and grow as a student. I was blessed to build an incredible community in Bellingham, both in and out of school, and I wouldn't have made it through this program without all of the amazing friends I have made in Washington.

Many thanks to my thesis committee, Brady Foreman and Allison Pfeiffer, for taking the time to provide valuable feedback as non-Martians and for being incredibly flexible and understanding given the unprecedented circumstances of a global pandemic and rash of reckoning with the racial injustice in our country, and in our field.

Lastly, thank you to my advisor, Melissa Rice, who managed to strike the perfect balance between challenging me and supporting me. As your student, I have learned so much about how to be both the scientist and mentor I aspire to be. I am so grateful for all of the opportunities and guidance you have given me in my time at WWU, and I look forward to a long career of continued collaboration and friendship.

Table of Contents

Abstract iv

Acknowledgements v

List of Tables and Figures vii

0. Overview 1

1. Introduction 6

2. Geologic Setting 7

3. Methods 13

4. Results 18

5. Discussion 37

6.. Post-VRR Analysis 44

7. Conclusion 52

References 54

List of Tables and Figures

Figure 1. Example laboratory spectra. 4
Figure 2. Context map of Curiosity's traverse 8
Figure 3. Schematic stratigraphic column 9
Figure 4. Mastcam multispectral coverage of Curiosity's traverse 19
Figure 5. Spectral variability of example dusty and dust-cleared targets. 20
Figure 6. Spectral variability of all dusty and dust-cleared rock targets 21
Figure 7. Spectral variability of float and in-place rocks. 23
Figure 8. Parameter space plot of float rocks and candidate meteorites 24
Figure 9. Spectral variability of example drill tailings 26
Figure 10. Spectral variability of all dusty rocks, DRT spots, and drill tailings 26
Figure 11. Spectral comparisons of Murray and Stimson formation 28
Figure 12. Mastcam ferric spectral parameter classes 30
Figure 13. Example ChemCam passive and Mastcam spectra 33
Figure 14. Spectrostratigraphic agreement between Mastcam and ChemCam passive data 34
Figure 15. Distant and proximal ROIs for Pettegrove Point member targets 36
Figure 16. Atmospheric effects on spectral "redness" 38
Figure 17. Spectrostratigraphic plots of all dusty and dust-cleared targets 40
Figure 18 Spectrostratigraphic plots for VRR dustyand dust-cleared rocks 41
Figure 19. Geologic context for Curiosity's traverse post-VRR 45
Figure 20. Spectral signatures of Glen Torridon Jura subfacies. 46
Figure 21. GT Jura subfacies in parameter space 47
Figure 22. Mastcam spectra of post-VRR drill tailings 48
Figure 23. Spectral variations across Greenheugh Pediment and underlying material 49
Figure 24. 676 nm absorption feature in dusty rocks, DRT spots, and drill fines. 50
Figure 25. Greenheugh Pediment region spectra in traverse context 51
Figure S1. Linear regresssion plots for covariance analysis 60

Table 1. Mastcam Filters 14
Table 2. Summary of spectral parameters used to characterize Mastcam spectra. 16
Table 3. Covariance analysis for Mastcam and ChemCam Passive spectra 34
Table S1. All multispectral observations 61

0. Overview

In 2012, the Mars Science Laboratory (MSL) Curiosity rover landed in Gale crater, a ~150 km diameter impact crater located on the Martian dichotomy boundary—a topographic border which separates northern lowlands from southern highlands. Based on crater counting in Gale crater's ejecta blanket, the impact is estimated to have occurred ~3.8 billion to 3.6 billion years ago (Thompson et al., 2011; Le Deit et al., 2013). Gale crater hosts a central mountain of sedimentary rocks reaching ~5 km above the crater floor named Aeolus Mons (informally, Mount Sharp) which has been the focus of much of Curiosity's ongoing mission (Golombek et al., 2012; Grotzinger et al., 2012). Geological inferences based on orbital mapping have been supplemented by remote and in situ observations by the rover, which provide imagery to assess geometry, texture, and grain size of strata, in addition to chemical compositions of select rock, vein, and soil "targets" of interest. Curiosity has been exploring Mars with a diverse instrument suite, including the Mast Camera (Mastcam; Bell et al., 2012), Chemistry and Camera (ChemCam; Maurice et al., 2012; Wiens et al., 2012), Chemistry and Mineralogy (CheMin) powder X-ray diffraction and fluorescence instrument (Blake et al., 2012), and Alpha Particle X-Ray Spectrometer (APXS; Campbell et al., 2012). Remote observations, acquired by Mastcam and ChemCam, are the least time and power intensive; therefore, several targets can be analyzed each time the rover stops in a new location, producing diverse datasets with the most individual targets analyzed. APXS is located on the turret at the end of the rover's arm, and usually requires the target rock to be brushed with the Dust Removal Tool (DRT) prior to APXS placement on the rock; typically one or two of these more time and power intensive observations are acquired at each rover stop. CheMin requires a drilled powder sample, which involves approximately one month's worth of activities to acquire; these drill campaigns are typically reserved for the most geologically significant targets, as well as bedrock documentation at consistent elevation intervals.

To date (July, 2020), Curiosity has traveled through nearly 400 vertical meters of sedimentary strata. Distinct stratigraphic units encountered along the traverse have been defined by the MSL team on the basis of outcrop morphology and chemical characteristics, and have been compiled into a schematic stratigraphic column with units demarked by elevation (Figure 2). This stratigraphic column, while a valuable reference, differs from traditional stratigraphic

columns in that it does not account for lateral variation among units, even though Curiosity has traveled over 10 horizontal kilometers in addition to the 400 vertical meters of elevation gain. Throughout this work, I refer to stratigraphic members and formations in the lower case, following an MSL team convention to indicate that these designations do not follow strict stratigraphic code guidelines (e.g., identifying a type locality for every formation and member).

Geologic History of Gale Crater Deposition

After its formation, Gale crater gradually filled with sediment. The rocks of the Bradbury group are the oldest Curiosity encountered, and are found near its landing site on Aeolis Palus. This group, along the crater floor plains northwest of Mount Sharp, is composed of small fluvio-deltaic complexes, which prograde into the predominantly subaqueous lacustrine deposits of the Murray formation, lying along the lower northwest slopes of Mount Sharp (Grotzinger et al., 2015; Stack et al., 2016). Orbital and ground-based observations suggest streams transported gravel and sand generated by the northern wall of the crater down into the center to form finer-grained (sand-sized), southward-advancing delta deposits, which then interfingered with an ancient series of lakes where fine (mud-sized) sediments were accumulating (e.g., Williams et el., 2013). Over an estimated timescale of 10^4 to 10^7 years, sediment accumulation in-filled the crater and its lake basin, until the wind-driven exhumation of these sediment deposits excavated the crater and left behind present-day Mount Sharp (Malin and Edgett, 2000; Grotzinger et al., 2015).

Mount Sharp's slopes also host hematite-, phyllosilicate-, and sulfate-bearing units (indicative of the complex aqueous history of the region), as well as the aeolian Stimson sandstone unit, which unconformably overlies the Murray formation and possibly the Bradbury group (Milliken et al., 2010; Fraeman et al., 2013; Bridges et al., 2015; Banham et al., 2018). Abundant occurrences of nodules, concretions, alteration halos, and fracture-filling veins indicate pervasive low-temperature post-depositional diagenesis, potentially in multiple episodes (e.g., Yen et al., 2017; Sun et al., 2019).

Mastcam & the Spectral Database

The Mastcam instrument—a multispectral, stereoscopic imager mounted on the rover's mast, approximately 2 meters above the Martian surface—can acquire spectra in 12 unique

wavelength positions from 445-1013 nm using its narrowband filter set (Malin et al., 2017). These spectra are calibrated based on pre-flight calibration coefficients and observations of a calibration target on the deck of the rover, and the resulting images are corrected for the angle of the sun at the time of image acquisition (Bell et al., 2017). Spectra acquired in this wavelength range are particularly useful for their sensitivity to iron-bearing minerals and oxidation phases; for example, the 867 nm and 527 nm band depths indicate the presence of iron oxidation, while the 937 nm band depth can indicate mafic iron-bearing minerals based on the presence of a broad absorption near 900 nm (Wellington et al., 2017). Figure 1 contains example laboratory spectra for several Fe-bearing minerals and Fe-oxides. The meter-scale Mastcam observations (of both the rocks right next to the rover, and distant outcrops) are accompanied by high-precision chemical data collected from individual rock, vein, and soil targets by the rest of Curiosity's instrument suite. Multispectral imagery places those spatially limited chemical analyses into a broader outcrop-scale context and expands chemical coverage of the rover's traverse (e.g., Bell et al., 2012).

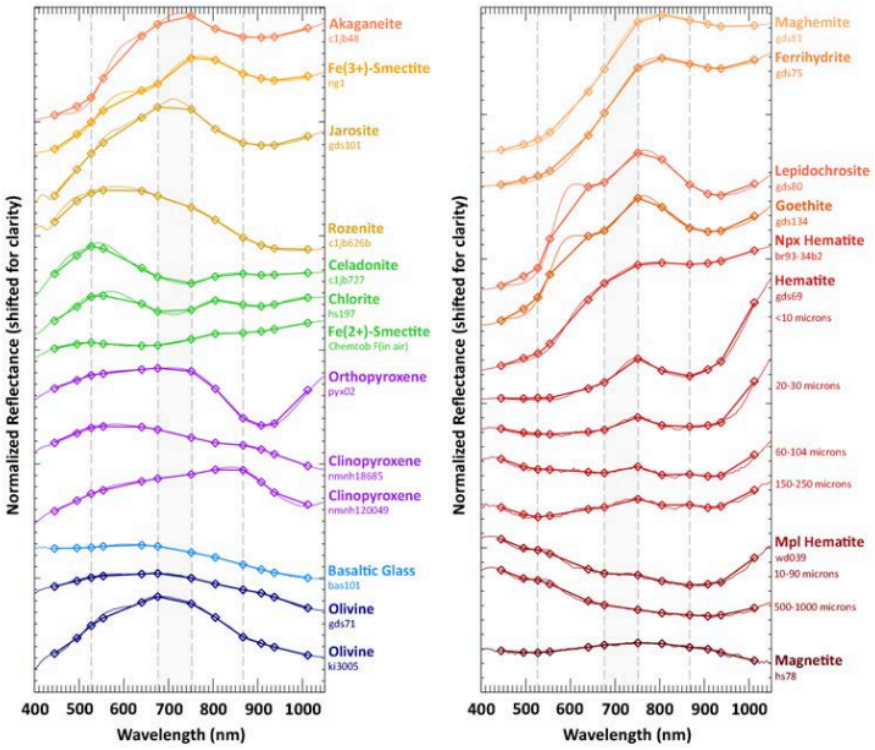

Figure 1. *From Horgan et al. (2020, Figure 3), example laboratory spectra of (a) common Fe-bearing minerals and (b) Fe-oxides, including hematite spectral variations with grain size and texture. Thin lines are original laboratory spectra, while points and connecting thick lines are the spectra convolved with Mastcam bandpasses. Vertical dashed lines highlight locations of absorption features discussed above, and gray box indicates the general location of a wide ~700 nm shoulder.*

All multispectral observations acquired by Curiosity, as well as the corresponding metadata, have been compiled into a database according to Rice et al. (2019) and Rice et al. (*in prep)*. By plotting the compiled observations in parameter space defined by different, geologically significant spectral parameters, I assess whether different stratigraphic units are spectrally distinct from each other. The resulting "spectrostratigraphic" plots are a convenient way to visualize spectral variations across stratigraphy, much like the common practice of mapping chemical variations within sediments via chemostratigraphy.

In this work, I describe the first comprehensive comparisons among Mastcam spectra of different regions, rock types, and soil across Curiosity's entire traverse, from 2012 to 2020. By convention, the MSL mission is measured in terms of Martian days, or "sols," rather than Earth years. The majority of these comparisons explore the rocks encountered from sols 750-2302 of the rover mission—from the first encounter with the Murray formation at the Pahrump Hills

locality to the end of Curiosity's exploration of the Vera Rubin ridge. In Sections 1-5, I present these results as a journal article to be submitted to *Journal of Geophysical Research – Planets* as a companion paper to Rice et al. (*in prep*), which details the methodology for creating the aforementioned database, and science results for the first 750 sols of the mission. The article is a collaborative endeavor incorporating data, analyses, and other inputs from the MSL Science Team (see Acknowledgements). Following the journal article, in Section 6, I present all work completed for this thesis that falls outside of the scope of the paper—namely, analyses of multispectral observations acquired from sols 2302-2755, as Curiosity traversed through the phyllosilicate-bearing Glen Torridon locality and overlying Greenheugh Pediment until its location as of the time of writing (July, 2020).

1. Introduction

The Mars Science Laboratory (MSL) Curiosity rover has traveled through nearly 400 vertical meters of sedimentary strata since landing in Gale crater in 2012. Its extensive traverse has generated data useful for evaluating chemical and stratigraphic relationships with implications for processes that shaped the aqueous history of Mars as a whole. From its landing site in a mudstone interval near Yellowknife Bay, the rover traversed through fluvio-deltaic deposits (comprising the Bradbury group) that prograde into the lacustrine deposits of the Murray formation found on the slopes of Aeolus Mons (informally, Mount Sharp), a ~5 km tall sedimentary mound in the center of the crater (e.g., Grotzinger et al, 2014, 2015). Distinct stratigraphic units encountered along the traverse have been defined on the basis of outcrop morphology and chemical characteristics, and have been compiled by the MSL team into a schematic stratigraphic column with units demarked by elevation (e.g., Edgar et al., 2020).

The Mast Camera (Mastcam) instrument has periodically acquired multispectral, visible to near-infrared (VNIR) observations of outcrops in this stratigraphic sequence. Spectra acquired in this wavelength range are particularly useful for their sensitivity to iron-bearing minerals and oxidation states; for example, the 867 nm and 527 nm band depths indicate the presence of iron oxidation, while the 937 nm band depth can indicate mafic iron-bearing minerals based on the presence of a broad absorption near 900 nm (Wellington et al., 2017). These meter-scale workspace and outcrop observations are often accompanied by high-precision chemical data from individual rock, vein, and soil targets collected by one or more of Curiosity's other in situ and remote science instruments: the Chemistry and Camera instrument (ChemCam; Maurice et al., 2012; Wiens et al., 2012), the Chemistry and Mineralogy instrument (CheMin; Blake et al., 2012), and the Alpha Particle X-Ray Spectrometer (APXS; Gellert & Clark, 2015). Multispectral imagery places those spatially-limited chemical analyses into a broader outcrop-scale context and expands their chemical interpretations from the rover's traverse (e.g., Bell et al., 2012).

Analyses of multispectral imagery to date have been focused on specific feature types such as drill targets (Wellington et al., 2017; Jacob et al., 2018), fracture-filling veins (Rice et al., 2018) meteorites (Wellington, 2018; Wellington et al., 2018, 2019), and high-SiO_2 material (Czarneki et al., 2020), or focused on specific locations, such as the Bagnold Dunes (Johnson et al., 2017, 2018), the Vera Rubin ridge (Fraeman et al., 2020; Horgan et al., 2017; Horgan et al.,

2020; Jacob et al., 2020), and distant Mt. Sharp strata (Fraeman et al., 2016; Fraeman et al., 2020). To date, no studies have yet described the full spectral variability seen by Mastcam across Curiosity's traverse, nor have any compared Mastcam spectral variations to changes in lithology. The rocks of Gale crater vary widely in lithology and diagenetic alteration through the stratigraphic section, and both ChemCam and APXS measurements track chemical trends throughout (e.g., Mangold et al., 2017). Adding Mastcam analyses to these trends is necessary to contextualize the spatially-limited observations within the broader Gale crater framework.

Here and in our companion paper (Rice et al., *this issue*; hereafter, Part I) we perform the first comprehensive comparisons among Mastcam spectra of different regions, rock types, and soil across the rover's entire traverse. This work specifically focuses on the sedimentary sequence on the flanks of Mount Sharp, observed from sol 750-2302. By defining spectral classes and correlating them with the well-defined stratigraphic sequence, we augment the existing parameters used to characterize lithologies and provide context for the high-resolution, but spatially limited, chemistry acquired by other instruments. We ultimately quantify the ways Mastcam spectra complement the rest of the MSL scientific payload to provide new methods to interrogate the history of aqueous deposition and alteration of sediments in Gale crater.

2. Geologic Setting

Since landing near Yellowknife Bay in 2012, Curiosity traversed over 20 km, gaining over 370 m in elevation. On sol 2302, it reached the southern edge of Vera Rubin ridge (VRR), a ~6.5 km long, ~200 m wide topographic ridge with a strong orbital spectral signature consistent with hematite (Fraeman et al., 2013, 2016, 2020) (Figure 2). Curiosity initially drove across the mudstones (Grotzinger et al., 2014), fluvial deposits (Edgar et al., 2018; Williams et al., 2013), and deltaic deposits (Grotzinger et al., 2015) of the Bradbury group, detailed in and the subject of Part I. Sol 750 marked a transition into the Mount Sharp group at the Pahrump Hills locality, and Curiosity has exclusively explored the Mount Sharp group and unconformably overlying Siccar Point group ever since (Banham et al., 2018). The Mount Sharp group to date is entirely composed of the Murray formation, a lacustrine mudstone sequence with subtle lithologic variations associated with the deposition and subsequent alteration of the rocks. Some mineralogical characteristics, such as abundant hematite, phyllosilicate, and Ca-sulfate, unite

deposits across the Murray formation (Achilles et al., 2020). North of VRR, the Murray formation is divided into five distinct stratigraphic members (Pahrump Hills, Hartmann's Valley, Karasburg, Sutton Island, and Blunts Point). VRR itself, while a distinct topographic ridge, is composed of Murray formation rocks divided into two members (Pettegrove Point and Jura) (Figure 3). Previous work has characterized the sedimentology of these units in detail, interpreting the Murray formation to be predominantly a mudstone succession deposited in a lacustrine or lake margin environment (e.g., Edgar et al., 2020; Grotzinger et al., 2015).

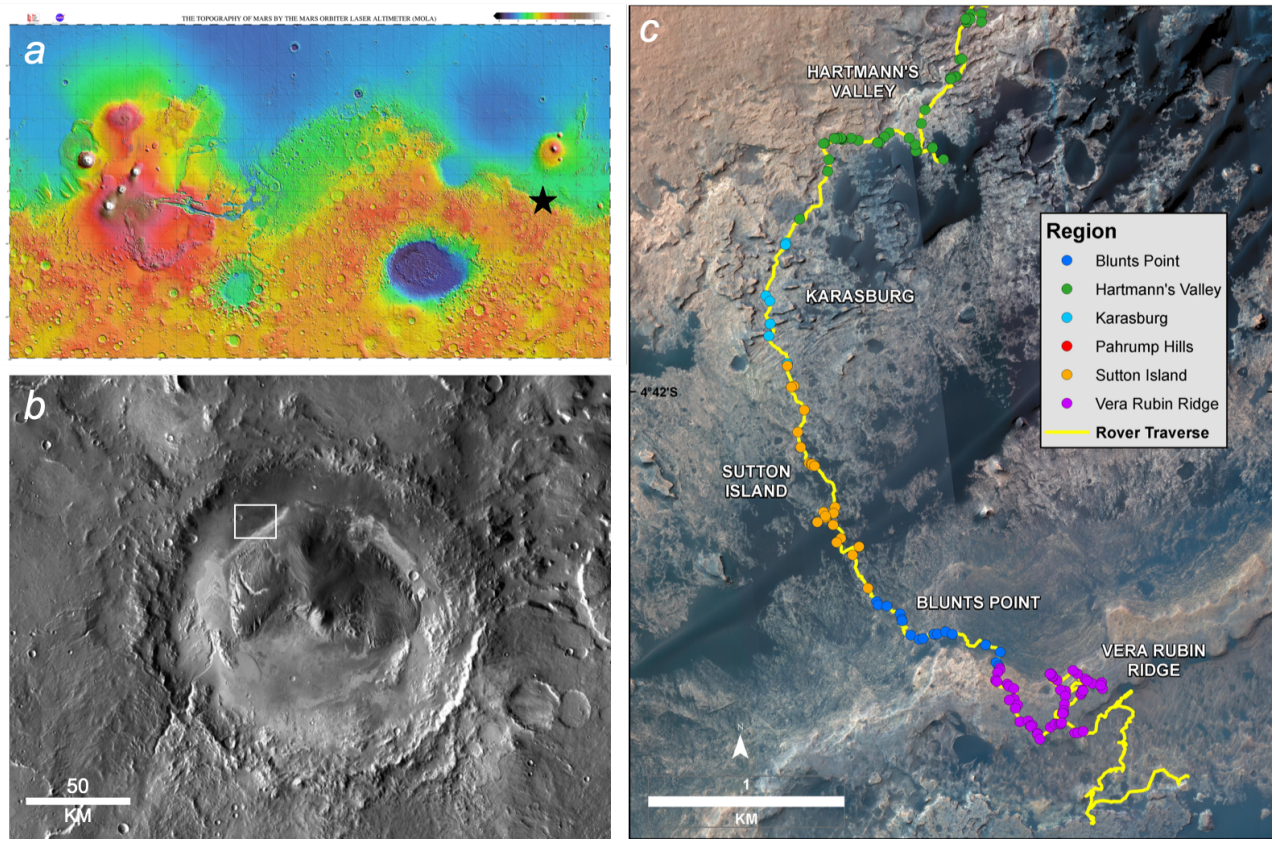

Figure 2. *Context map of Curiosity's traverse, Gale crater, Mars. (a) Global topographic map from Mars Orbiter Laser Altimeter (MOLA) with Gale crater, at the dichotomy boundary between southern highlands and northern lowlands, indicated with black star. b) HiRISE imagery of Gale crater, with white square indicating Curiosity's traverse region. (c) Curiosity's traverse from sol 750-2302. Dots correspond to Mastcam multispectral observations acquired in each respective member of the Murray formation; courtesy of Fred Calef.*

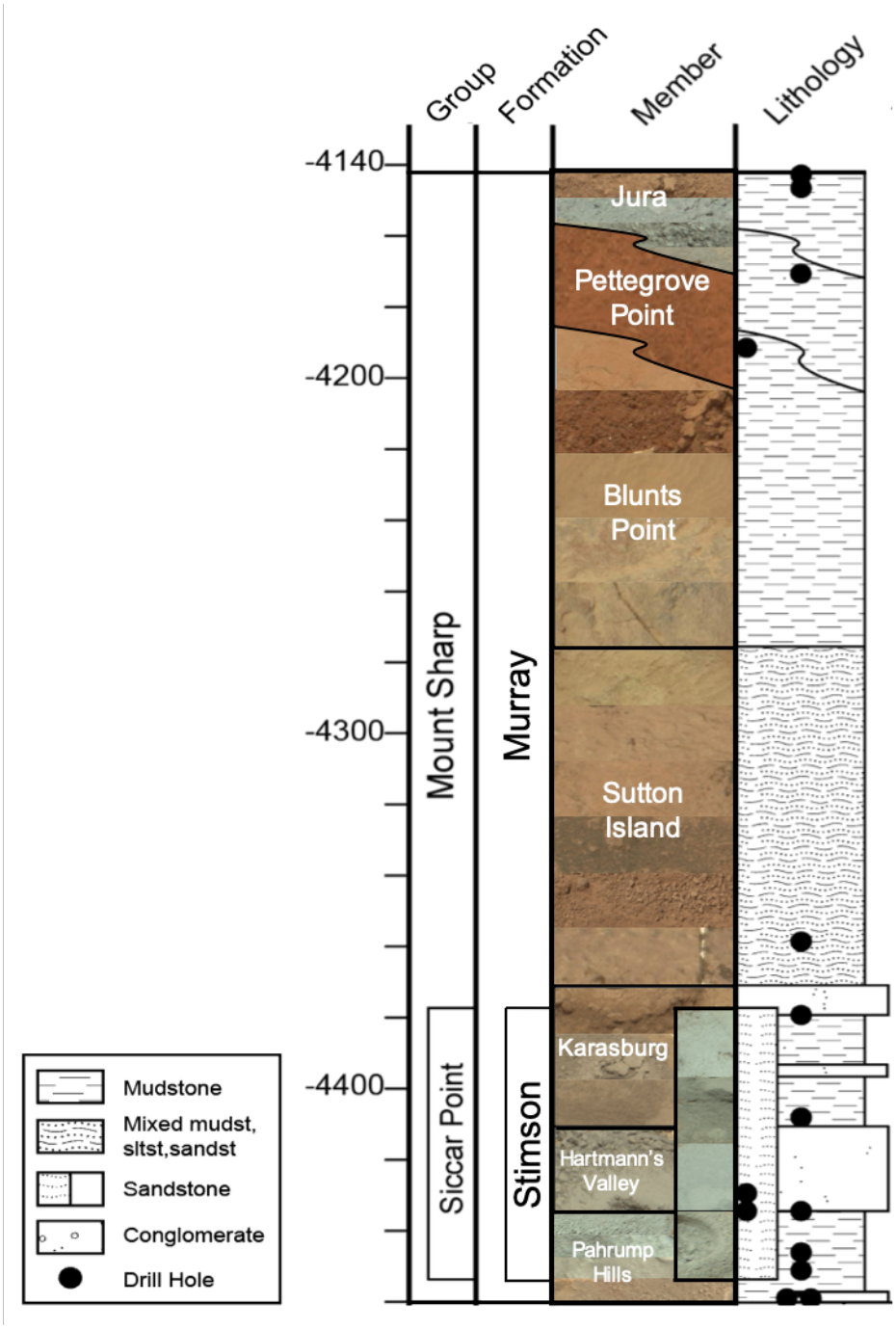

Figure 3. *Schematic stratigraphic column for all stratigraphic units observed. Note that Curiosity has traveled over 10 horizontal kilometers and thus the schematic column cannot account for lateral variation among the units represented. Slanted contacts between VRR stratigraphic members indicate observed elevation changes in three transects across VRR. Murray formation drill targets have distinct symbols to differentiate members. Example uncalibrated Mastcam RGB images of drill tailings and dust-cleared rock patches exhibit the full range of each member's spectral diversity in the member column.*

2.1 Sedimentology and Stratigraphy

Murray Formation

The earliest Murray formation deposits, those comprising the Pahrump Hills member, are millimeter- to centimeter-scale laminated mudstones to very fine sandstones interpreted to have formed by suspension fallout in a lacustrine environment with occasional hyperpycnal plume influence (Minitti et al., 2019; Rivera-Hernández et al., 2019; Stack et al., 2019). These deposits are overlain by the siltstone to very fine sandstone of the Hartmann's Valley member, which is characterized by prominent laminations and meter-scale trough cross-stratification and interpreted to be deposited in a lake margin setting, either by aeolian or fluvial processes (Fedo et al., 2017; Gwizd et al., 2018). The overlying Karasburg member sediments, with many similarities to those of the Pahrump Hills member, indicate a return to subaqueous deposition; this more purple-hued mudstone to very fine sandstone with millimeter- to centimeter-scale parallel laminations and abundant phyllosilicate minerals (Rampe et al., 2017) is interpreted to have formed in a low-energy lacustrine environment (Fedo et al., 2017). The next stratigraphic interval is the heterolithic mudstone-sandstone of the Sutton Island member, interpreted to have formed in a lacustrine and lake margin setting. This unit includes fine-grained centimeter-scale ripple cross-laminated mudstone, decimeter-scale cross-stratified siltstone, and very fine sandstone, and contains concretions, possible desiccation cracks, and sulfate enrichments (Rapin et al., 2019; Stein et al., 2018). After this period of apparent subaerial exposure, sediments again return to stable lacustrine deposits in the Blunts Point member, a mudstone characterized by recessive, fine-grained facies with extensive planer lamination crosscut by curviplanar calcium sulfate veins (Fedo et al., 2018; Edgar et al., 2020).

Although there is a distinct topographic break at the base of VRR, the rocks exposed on the ridge are consistent with the lithologies expressed in the rest of the Murray formation, and they are conformable with the underlying Blunts Point member rocks (Edgar et al., 2020). The stratigraphically lower Pettegrove Point member is a fine-grained, thinly laminated mudstone with parallel stratification and abundant diagenetic nodules and concretions, and is interpreted to as representing stable lacustrine sedimentation close to a near-shore environment (Edgar et al., 2020). Topping VRR as the highest stratigraphic unit discussed in this work is the fine-grained mudstone of the Jura member. This unit includes parallel stratification, red and gray color variations, decimeter- to meter-scale inclined beds with varying dips, and occurrences of

diagenetic crystal molds, leading to interpretation as variable lacustrine deposition followed by slumping due to small slope failures (Edgar et al., 2020).

Other Lithologies

The Siccar Point group unconformably overlies the Mount Sharp group, and has been encountered at several points throughout the rover's traverse. It was primarily explored in the Stimson formation, a blocky gray-toned meter-scale cross bedded sandstone unconformably overlying the Murray formation, interpreted to be aeolian (Banham et al., 2018; Watkins et al., 2016). The Stimson formation was often observed as a capping unit atop mounds of mudstone, such as at the Murray Buttes, and the rover drove across an expanse of it from sols ~1000-1350 (Banham et al., 2018).

Occasional targets were encountered that are obviously incongruous with the surrounding bedrock, standing out visually, spectrally, and/or chemically. Frequently, small, scattered blocks were determined to be iron meteorites, with iron/nickel-rich ChemCam compositions and "grayish" Mastcam spectra with positive NIR slopes (e.g., Wellington 2018; Wellington et al., 2018, 2019). After leaving the fluvial conglomerates of the Bradbury group (Williams et al., 2013), enigmatic decimeter-scale conglomerate blocks were encountered on the erosional surface of the Murray formation at the Bimbe locality (Wiens et al., 2020) and at and near the Bressay locality on VRR (Williams et al., 2020).

Diagenetic Features

Diagenetic features and alteration signatures are abundant in the rock units observed in this segment of the traverse. These features include fracture-filling veins abundant throughout the stratigraphic section (Fedo et al., 2018; Kronyak et al., 2019; Nachon et al., 2017; L'Haridon et al., 2018); four major assemblages of concretions, found throughout the Murray formation (Sun et al., 2019); and silica enrichment in fracture associated halos in both the lower Murray and the Stimson formation (Gabriel et al., *in review*; Hasurath et al., 2018; Freydenvang et al, 2017; Yen et al., 2017). Diagenetic features within VRR specifically include crystals and crystal pseudomorphs (Bennett et al., 2020), nodules and dark diagenetic features (Bennett et al., 2020; L'Haridon et al., 2020), fracture-filling calcium sulfate veins (Fedo et al., 2018), and red-gray color variation cross-cutting primary lamination (Fraeman et al., 2020; Horgan et al., 2020).

While VRR is lithologically consistent with the rest of the Murray formation, it has chemistry and alteration products which suggest that it was cemented by a higher degree of diagenetic alteration from late-stage fluids than the surrounding sediments (Fraeman et al., 2019; Freydenvang et al, 2019; Thompson et al., 2019).

2.2 Geochemistry and Mineralogy of the Murray Formation

Chemical, mineralogical, and sedimentological evidence from Curiosity's instrument suite support a similar provenance and depositional history for the entire Murray formation, with variations influenced by depositional and diagenetic fluid compositions. Mineralogy and chemistry variations over the basal ~13 meters of this unit as measured by CheMin indicate a shift from hematite-dominated to magnetite-dominated mineral assemblages, and trace element abundances for Zn, Ni, and Mn gradually increase up section (Rampe et al., 207). Measurements of the 527 nm absorption feature (consistent with the presence of crystalline hematite) in Mastcam spectra extracted from the three Pahrump Hills drill targets show decreasing band depths consistent with the CheMin measured abundances (Wellington et al., 2017). These trends have been interpreted to be the result of diagenetic episodes from several groundwater influxes (Rampe et al., 2017) or variations in lake water pH and redox conditions (Hurowitz et al., 2017). While magnetite may be more common in samples drilled near the base of the Murray formation, hematite is the dominant Fe-oxide mineral in the drill samples in subsequent members, a trend which suggests increasingly oxidative conditions over time (Bristow et al., 2018; Rampe et al., 2020b). There are subtleties to this trend, however: while the Karasburg and Sutton Island drill samples contain some hematite (notably more than is detected in Pahrump Hills), the Hartmann's Valley drill sample contains a significantly higher abundance of gray hematite than the overlying drill samples (Bristow et al., 2018). The Karasburg and Sutton Island drill samples themselves are compositionally similar, with dominant phyllosilicates and subordinate hematite and Ca-sulfate (Fedo et al., 2017). The up-section increase in clay mineral abundances measured by CheMin is consistent with increasing alteration indices measured by ChemCam reflecting a greater degree of open-system chemical weathering in the middle Murray formation than the lower (Manglold et al., 2019). While Mastcam has detected spectral signatures consistent with hematite throughout the Murray formation (from ~ sol 1160 onwards), the rocks exhibit spectral differences in the 867 – 1012 nm slope, red/blue ratio, and overall reflectance, which suggests

varying mineral grain sizes and/or abundances of iron-bearing mineral phases (Wellington et al., 2017).

VRR is chemically consistent with the rest of the Murray formation, but alteration by secondary processes likely led to the creation of the erosion-resistant topographic ridge itself (Fraeman et al., 2020). CheMin analyses, including the detection of gray hematite in the Jura member, suggest that well after lacustrine deposition, VRR rocks were preferentially altered by multiples episodes of variably warm, saline, and or acidic fluids (Rampe et al., 2020a). The multiple episode model is corroborated by ChemCam analyses, which show a decrease in the chemical index of alteration (CIA) across the ridge independent of elevation and stratigraphy, indicating a decrease in VRR clay mineral abundance independent of deposition (Frydenvang et al., 2020). Mastcam multispectral analyses of VRR further demonstrate strong color differences crossing stratigraphic boundaries corresponding to nanophase, fine-grained, and coarse-grained hematite; Horgan et al. (2020) suggest that the red and nanophase hematite observed was a product of oxidation in early meteoric or lacustrine diagenesis, while gray patches across the ridge were produced later as hematite coarsened under possibly acidic, reducing, and/or warmer conditions. Ultimately, Rampe et al. (2020) propose that the late-stage diagenetic fluids altering VRR rocks may have extended to alter other parts of the Murray formation, but VRR experienced the most intense alteration—possibly due to proximity to a Siccar Point caprock influencing the fluid path by forcing fluids along the contact between the two units. This pattern may be reflected across the Murray formation and the multiple diagenetic events it has experienced: mineralogical differences may be related to physical controls imposed by proximity to sandstone units like the Stimson formation (Achilles et al., 2019).

3. Methods

3.1 Multispectral Observations and Analysis

The Mastcam instrument is a multispectral, stereoscopic imager mounted on the rover's mast, approximately 2 meters above the Martian surface (Malin et al., 2017). Its two cameras have fixed focal lengths, with 34-mm context imaging in the left camera (M34) and 100-mm higher resolution imaging in the right camera (M100). They acquire images through both a Bayer pattern (red, green, blue; RGB) filter set bonded to the CCD detectors and an eight-

position filter wheel. Each filter wheel holds one broadband IR-cutoff filter for Bayer RGB imaging, six narrowband geology filters, and one narrowband neutral density filter for solar observations, allowing Mastcam to acquire spectra in 12 unique wavelength positions from 445-1013 nm (Table 1) (Bell et al., 2017).

Table 1. Mastcam RGB Bayer and geology filters effective center wavelengths (λ_{eff}) and half-widths at half-maximum (HWHM) (Bell et al., 2017).

Mastcam Left (M34)		Mastcam Right (M100)	
Filter Position	**λ_{eff} ± HWHM (nm)**	**Filter Position**	**λ_{eff} ± HWHM (nm)**
L0 (Red Bayer)	640 ± 44	R0 (Red Bayer)	638 ± 44
L0 (Green Bayer)	554 ± 38	R0 (Green Bayer)	551 ± 38
L0 (Blue Bayer)	495 ± 37	R0 (Blue Bayer)	493 ± 37
L1	527 ± 10	R1	527 ± 10
L2	445 ± 10	R2	447 ± 10
L3	751 ± 10	R3	805 ± 10
L4	676 ± 10	R5	937 ± 10
L5	867 ± 10	R4	908 ± 10
L6	1012 ± 21	R6	1013 ± 21

Mastcam observations are calibrated to radiance ($W/m^2/nm/sr$) based on pre-flight calibration coefficients, and then converted to radiance factor (*I/F*) using temporally equivalent on-board calibration target observations, corrected for illumination, viewing geometry, and dust accumulation (Kinch et al., 2015; Bell et al. 2017; Wellington et al., 2017). The resulting *I/F*-calibrated images are converted to relative reflectance (*R**) by dividing by the cosine of the solar incidence angle at the time of imaging.

In this study, we use all Mastcam multispectral observations acquired between sols 750 and 2302 (Table S1). These observations have been calibrated and processed for incorporation into a Mastcam spectral database according to methodology detailed in Part I (Rice et al., this issue). For each observation, the M100 and corresponding M34 images were visually inspected to identify spectral end members in RGB, false color, and decorrelation-stretched image products (Gillespie et al., 1986). These end members are unique regions in color space that also correspond to geologically significant features within the scene (e.g. dusty rock surface vs. one brushed with the rover's Dust Removal Tool, or layered deposits with compositional differences across the outcrop). We manually extracted reflectance spectra from regions of interest (ROIs) within each end-member according to best practices outlined in Part I (Rice et al., this issue).

Reflectance values reported for each ROI are an average of all pixels within each ROI, and therefore we report $R*$ error as the variance within each ROI, which is typically larger than the estimated error in the instrument calibration (Bell et al., 2017).

To geologically contextualize the set of spectra presented for the sol range of this study, key metadata were recorded for each observation in the Mastcam spectral database (Part I). These include both the necessary metadata for viewing geometry corrections (derived from PDS image headers) and geologically relevant classifications for feature types (e.g. soils, drill fines, dusty rocks, dust-cleared rocks, etc.). Each spectrum is labeled according to its position within the defined stratigraphy; lithologic designations follow published member boundaries, and where no data are available, designations are made based on color, texture, composition, distinctive features (such as laminations or concretions), and stratigraphic context. Float blocks with significant similarity to a known stratigraphic unit are assigned that lithologic designation; those that cannot be easily determined are unclassified. The few conglomerate targets encountered are unclassified due to their ambiguous origins; future work is needed to determine if the two conglomerate deposits encountered in the sol range of this study are related to the numerous conglomerates encountered earlier in the mission in the Bradbury group.

Here, we focus on several key spectral parameters, including known VNIR features associated with iron-bearing minerals (e.g. Burns, 1970, 1993; Gaffey et al., 1993; Morris et al., 1985) and hydration (Rice et al., 2010). The parameters include reflectance ratios (reflectance values in one Mastcam filter divided by another), slope values (the difference in reflectance values divided by the difference in wavelength), and band depth values (at a given wavelength position, the reflectance value's depth below a continuum line drawn between two "shoulders" on either side of an absorption feature, as defined by Clark and Roush (1984)). Spectral parameters were chosen based on relevance for analyzing the diagenetically altered lacustrine mudstones and capping aeolian sandstones in this portion of the rover's traverse up Mount Sharp (Table 2). Uncertainties for the calculated parameters are reported as the 1-σ standard deviation of potential parameter values modeled for each target based on uncertainties associated with the individual components of the band parameter calculations after Jacob et al. (2020).

Table 2. Summary of spectral parameters used to characterize Mastcam spectra.

Parameter	Formula	Possible Mineralogic Indicators
527 nm band depth	$1 - (R^*_{527} / (0.23R^*_{447} + 0.77R^*_{551}))$	Larger value can indicate higher degree of Fe oxidation (e.g., Farrand et al., 2008)
640 / 527 nm ratio	R^*_{640} / R^*_{527}	Larger values are consistent with fine-grained hematite and other Fe oxides (e.g. Horgan et al., 2019)
751 / 445 nm ratio	R^*_{751} / R^*_{445}	Along with 445-751 nm slope, often termed "red-blue slope," can indicate "redness" of spectra; larger values are consistent with higher degrees of oxidation (e.g., Farrand et al., 2008)
751 / 527 nm ratio	R^*_{751} / R^*_{527}	Used as a proxy for shorter wavelength slope; values closer to 1.0 can be consistent with iron meteorites (e.g. Wellington, 2018)
751 – 1012 nm slope	$(R^*_{1012} - R^*_{751}) / (1012 - 751)$	Negative slopes may indicate broad Fe absorptions in the NIR
805 – 1013 nm slope	$(R^*_{1013} - R^*_{805}) / (1013 - 805)$	Negative slopes may indicate broad Fe absorptions in the NIR; "Flat" slopes are consistent with phases that are spectrally-neutral in the NIR (e.g., pure sulfates); Positive slopes are consistent with hematite.
867 nm band depth	$1 - (R^*_{867} / (0.556R^*_{751} + 0.444R^*_{1012}))$	Larger values are consistent with presence of fine-grained, red crystalline hematite (equation after Bell et al., 2000)
1012 / 751 nm ratio	R^*_{1012} / R^*_{751}	Used as a proxy for NIR slope; values > 1.0 can be consistent with iron meteorites (e.g. Wellington, 2018)

3.2 Spectral Comparisons

This study focuses on the broad spectral trends observed by plotting the aforementioned key spectral parameters against all of the different lithologies encountered in the stratigraphic sequence explored thus far. The resulting "spectrostratigraphic" plots represent spectral variations across stratigraphy with changes in elevation, much like the common practice of mapping chemical variations within sediments via chemostratigraphy (e.g. Frydenvang et al., 2020).

In order to track chemical relationships across datasets produced by different instruments aboard Curiosity, we compared these spectrostratigraphic results to published chemostratigraphic data from ChemCam and APXS. Because distinctive spectral features indicate the presence of specific mineral assemblages, we assessed the spectra for each lithology for agreement with corresponding samples and mineralogies determined by the other chemistry instruments. Such comparisons are routinely employed for individual samples (e.g. Wellington et al., 2017), but have not previously been completed on a traverse scale.

Our primary analysis of these spectrostratigraphic plots compared them to those produced with the ChemCam instrument. While ChemCam is primarily a laser-induced breakdown

spectrometer (LIBS) (Maurice et al., 2012; Wiens et al., 2012), Johnson et al. (2015, 2016) have shown that the violet (382-469 nm) and VNIR (474-906 nm) spectrometers are sensitive enough to collect reflectance spectra from rock and soil targets without firing the laser (creating ChemCam "passive" spectra). ChemCam passive measurements are acquired with a 3 msec exposure after every LIBS target is shot, and the resulting spectra are converted to relative reflectance following Johnson et al. (2015). Spanning a 400-840 nm range, these spectra complement Mastcam spectra, and allow for direct comparison of many of the same spectral features. Here, we focus on the band depth at 527 nm in Mastcam and 535 nm in ChemCam passive, consistent with iron oxides, and the band depth at 867 nm in Mastcam and the negative slope between 750 – 840 nm in ChemCam passive, consistent with fine-grained red crystalline hematite. In an additional assessment of agreement between instruments, we also conducted a more direct comparison by convolving ChemCam spectra to Mastcam bandpasses to evaluate the 527 nm band depth and 751-805 nm slope. As in Fraeman et al. (2020), ChemCam passive targets were limited to sunlit bedrock surfaces, excluding soils, diagenetic features, drill fines, and data acquired between sols 2076-2215 (affected by the 2018 global dust storm event), and Mastcam targets were limited to rock targets (both typical dusty surfaces and those partially cleared of dust by the Curiosity's Dust Removal Tool (DRT)). Because ChemCam acquires spectra up to ten LIBS shots per target, we calculated the median band depth and slope values for each target to ensure outliers such as veins or nodules targeted by the LIBS shots were not included.

Fraeman et al. (2020) qualitatively demonstrated that Mastcam and ChemCam passive spectra across this sol range exhibit the same spectral trends consistent with iron oxidation and hematite; these trends not only increase and decrease through different stratigraphic units, but change significantly in variance throughout the sequence (Fraeman et al., 2020). Here, we build on the Fraeman et al. (2020) qualitative comparison with the first quantitative evaluation of trends identified in the two instrument datasets by calculating their covariance (e.g. Gretton et al., 2005). Though both instruments did not necessarily collect data from the same targets, target elevation is a reasonable proxy for identifying similar rocks, as it selects for targets acquired in either the same workspace in front of the rover, or stratigraphically equivalent rocks. Elevation (rather than sol) was chosen to account for the segments of the traverse (especially VRR) where the rover drove multiple transects through the stratigraphic section, backtracking and visiting

lower members on later sols. Member boundaries on VRR do not conform to strict elevation boundaries, but these discrepancies were negligible in the compilation of our dataset. Therefore, we compared the aforementioned spectral parameter values for targets at equivalent elevations, which resulted in 311 spectra per instrument for analysis. For each elevation z, we calculate the covariance between the targets from the two datasets, Mastcam band depth, $X(z)$, and ChemCam passive band depth or slope, $Y(z)$, with:

$$Cov(X,Y) = \frac{1}{N-1}\sum_z (X(z) - \mu_X)(Y(z) - \mu_Y)$$

where N is the number of elevations for which we have data points, and μ_X and μ_Y are the mean of X and Y. We expect that if the Mastcam band depth at elevation z is much higher than the mean Mastcam band depth, the ChemCam passive band depth is also likely to be higher than the mean ChemCam passive band depth; this will result in a large positive sum. Highly-dependent variables have a high positive covariance, while independent variables have a covariance of zero.

To determine statistical significance, we used permutation testing; we fix X at each elevation and chose a random value from Y with replacement to generate the variable Y', which should be independent from X. By comparing the covariance between X and Y to that between X and Y' for many permutations, we can quantify the significance of $Cov(X,Y)$. The covariance of our original data is higher than q-percent of the scrambled covariance, providing a p-value of $1 - q$. We performed 10,000 permutations to achieve high enough statistical power to resolve the statistically significant tests. In multiple hypothesis testing, the likelihood of incorrectly rejecting one of the null hypotheses increases with increased tests, so we compensated for that increase with the Bonferroni correction, testing each hypotheses at a significance level of 0.05/4, where 0.05 is the desired significance level and 4 is the number of tests we performed (e.g. Benjamini & Hochberg, 1995).

4. Results

As of sol 2305, Mastcam has acquired 459 multispectral observations—those that use narrowband filters in addition to the RGB filters—of surface geology targets (eight of which are excluded from this study due to extensive shadowing or failed image execution and/or incomplete downlink due to rover faults). All analyses for multispectral observations acquired

on sols 0-750 are discussed in the companion paper (Rice et al., this issue). Here, we present the results of the analyses for observations acquired on sols 750-2302, encompassing Curiosity's traverse through the Mount Sharp group, from entering the Murray formation at Pahrump Hills to exiting the Vera Rubin ridge.

Mastcam multispectral observations were acquired in all members of the Murray formation (Figure 2). The time spent exploring the Pahrump Hills region and subsequent deposits resulted in extensive multispectral coverage of the lower Murray formation. The driving pace increased as Curiosity began climbing in elevation through the Karasburg, Sutton Island, and Blunts Point members, occasionally resulting in elevation gaps in multispectral coverage. A temporarily-broken drill also expedited the observation cadence through this interval, because the rover did not stop to collect drill samples (which require stationary weeks at a time and result in abundant characterization of the surrounding site). Once the rover reached the Pettegrove Point member, the multispectral cadence increased with the start of VRR campaign. VRR campaign resulted in three transects across the ridge, increasing multispectral coverage across this elevation interval.

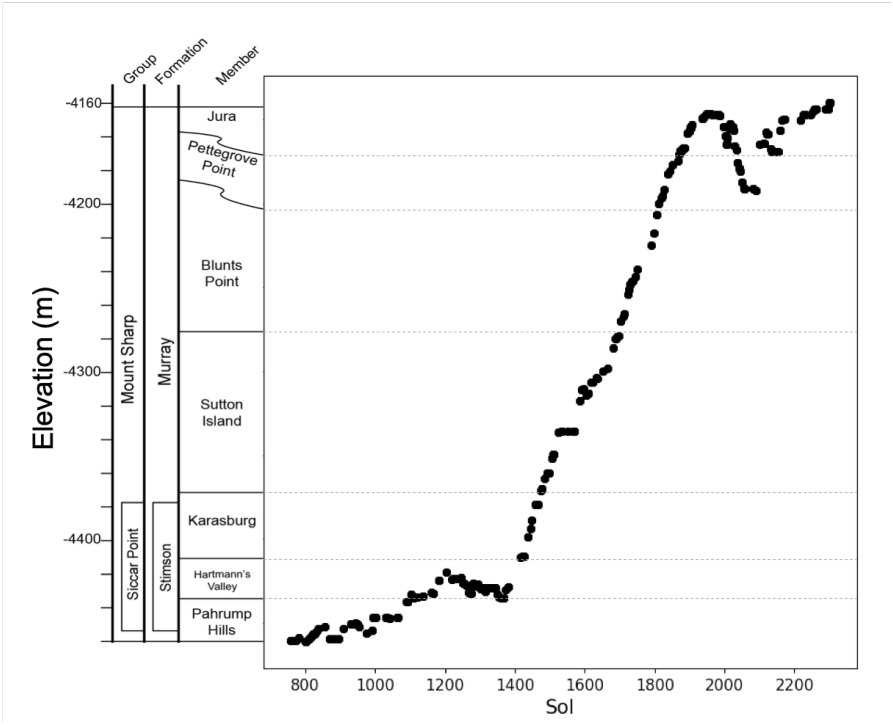

Figure 2*. Mastcam multispectral coverage of Curiosity's traverse. Black dots represent all multispectral targets observed from sol 750-2302. Elevation corresponds to rover elevation at the location of observation, and stratigraphic column is given for geologic context.*

4.1 Influence of Dust on Rock Spectra

Where Curiosity's DRT had been employed, we extracted spectra from the resulting dust-cleared rock surface, as well as spectra from adjacent, dusty rock surfaces. From sols 750-2302, Mastcam observed 106 DRT spots. Direct comparisons of dusty and dust-cleared targets demonstrate that dust consistently masks rock spectra, resulting in higher reflectance (especially at longer wavelengths), muted absorption features, and smaller 751/445 nm ratios. For some targets (e.g., Mojave, Figure 3), reflectance increases in the shortest wavelengths; however, very high reflectance values observed at the shortest wavelengths may not be accurate due to calibration-based artifacts discussed in Part I. These trends are evident in individual observations in both Murray and Stimson formation targets: Figure 3 contains examples of representative Stimson spectra and the spectral diversity of the Murray formation captured by two different members. Across the entire dataset, dust-cleared rocks tend to exhibit greater absorption at 867 nm than dusty rocks, particularly on VRR. They also exhibit consistently lower red-blue slopes, especially in the lower Murray formation where 527 nm absorption features are also shallower for dust-cleared rocks (Figure 3).

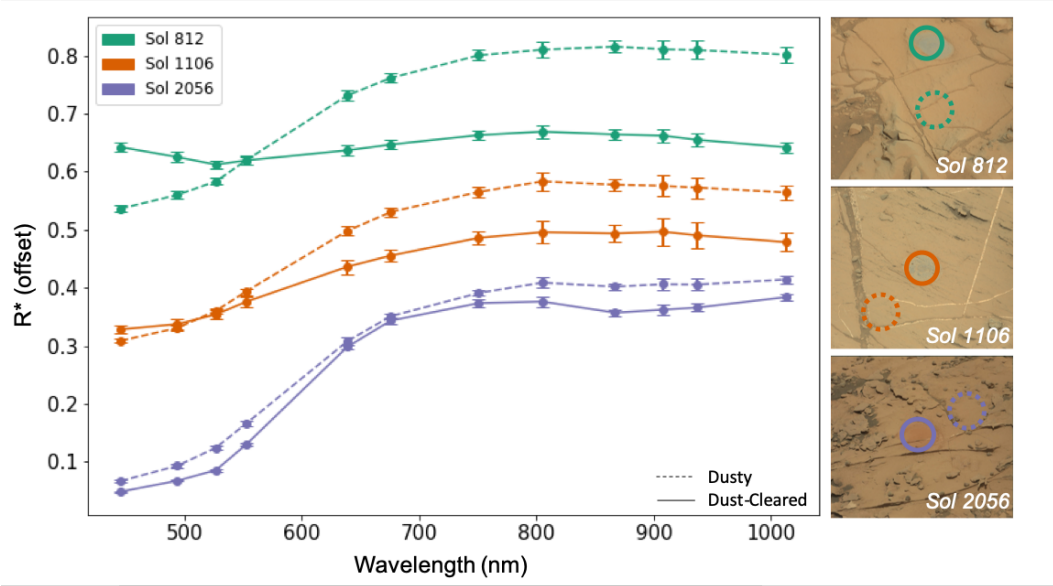

Figure 3. *Spectral variability of example dusty and dust-cleared targets. Dust consistently masks the rock spectra. (left) Mastcam spectra, where solid lines indicate dust-cleared rock targets, and dashed lines indicated adjacent dusty bedrock. Spectra are averaged within each ROI, offset for clarity, and shown with one standard deviation error bars. (right) Mastcam RGB images of three example observations with spectra extracted from ROIs within DRT spots (solid circle) and adjacent dusty bedrock (dashed circle). Targets are Mojave (Pahrump Hills member; sol 812, mcam 03564), Winnipeg (Stimson formation; sol 1106, mcam 04915), and Duluth (Blunts Point member; sol 2056, mcam 10897). DRT spots are ~40mm in diameter.*

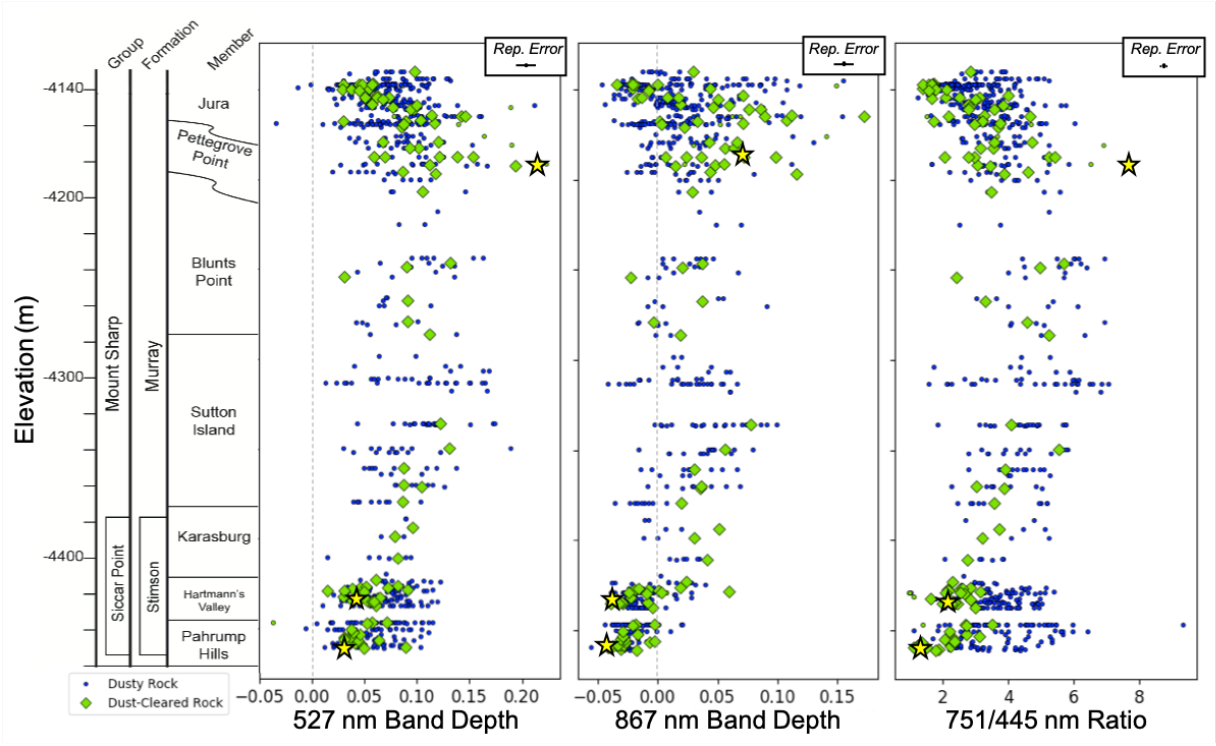

Figure 4. *Spectral variability for all dusty and dust-cleared rock targets. Dust-cleared targets (green diamonds) tend to have shallower 527 nm absorption features, deeper ones at 867 nm, and lower 751/445 nm ratios than their dusty counterparts (blue dots). Differences in slope values are more evident in the lower Murray formation than VRR. Small green dots are fresh faces of rocks broken by the rover's wheels. Example DRT targets from Figure 3 are indicated by yellow stars.*

4.2 Float Rocks

It is rare to encounter large, cohesive bedrock outcrops in Gale crater; rather, Curiosity mostly explored an expansive, broken pavement punctuated by relatively small-scale topography. We classify the rocks in multispectral observations either as in situ rock, or as "float" (not attached to outcrop). Therefore, float rocks can either be eroded components of bedrock (more abundant in less cohesive rock units than others), or anomalous, foreign material (e.g., impact ejecta or meteorites). For observations with both in situ and float rocks with the same spectral signature, spectra are extracted from the in situ rock.

In this study, we include spectra extracted from 541 in situ ROIs, and 225 float rock ROIs. Float rocks are distributed throughout the stratigraphic sequence, though are sparse in the Blunts Point member (Figure 7). In general, float rocks are spectrally consistent with the proximal in situ targets, though float rocks in the Sutton Island member are more spectrally

diverse than their in situ counterparts (Figure 7). We identify several spectral outliers across the traverse (Figure 7, stars). Many anomalous float blocks have been identified as candidate meteorites or fragments (based on morphology and spectral properties), and some have been confirmed by chemical measurements; these three targets were identified by Wellington et al. (2018, 2019) as candidate meteorites. Because iron meteorite spectra typically have distinct positive NIR slopes from 751-1012 nm and grayish visible spectra (Wellington, 2018), we plotted all float rocks in our dataset in this parameter space and found these float blocks to plot distinctly from all others, with spectra consistent with iron meteorites (Figure 8). We identify one nearby outlier in parameter space (teal sol 2259 target), which shares some but not all spectral characteristics with the others, and is not an outlier in Figure 7. Therefore, we do not identify any new meteorites in our dataset, but do identify a transition zone in parameter space between candidate meteorites and ambiguous, similar material; in future observations, spectra with a 1012/751 ratio greater than 1.1 should be investigated as iron meteorites. Meteorites detected by Curiosity are dominantly iron-nickel and stony iron types, which may be more abundant, more resistant to erosion, or more easily spotted (or some combination of the three) than chondritic meteorites (Wellington et al., 2018). Because all outliers discussed here are spectrally consistent with iron meteorites and we have yet to detect impact ejecta or chondritic meteorites, any future float observed that does not spectrally match local bedrock or iron meteorite signatures may be one of these alternative types of foreign material.

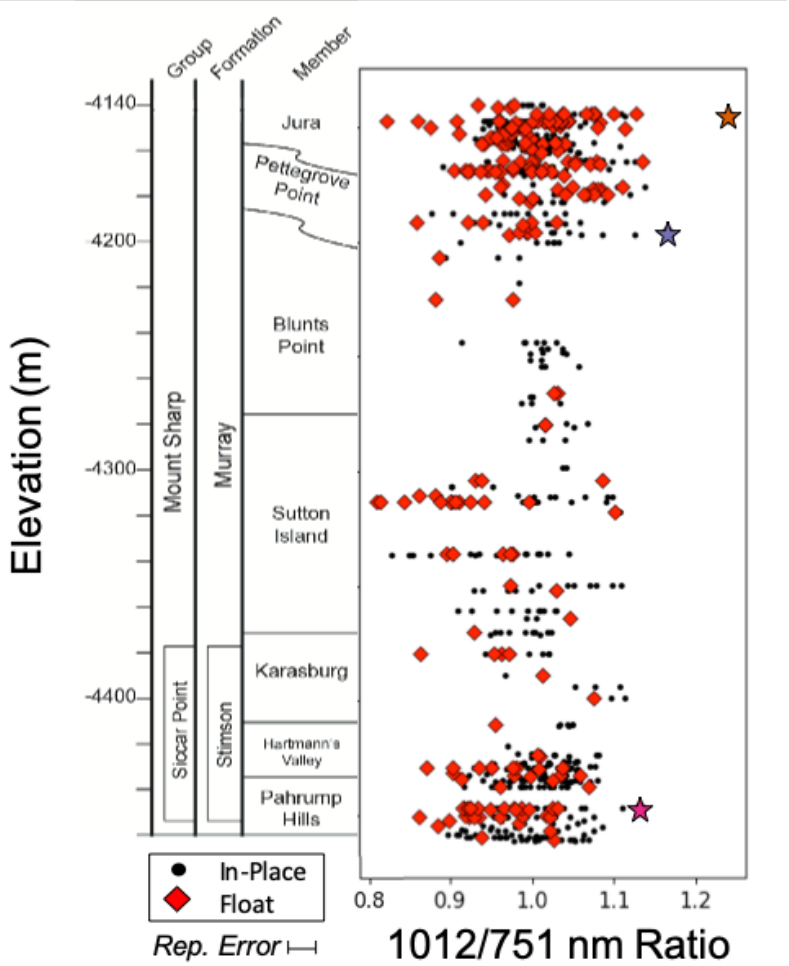

Figure 5. *Spectral variability in float rocks (red diamonds) compared to in-place rocks (black points) across Curioisty's traverse, with stratigraphic column for reference. Three outliers (stars) are discussed in Figure 6. In general, float rocks exhibit similar spectral signatures to proximal bedrock, suggesting that the majority of float rocks are eroded components of that bedrock.*

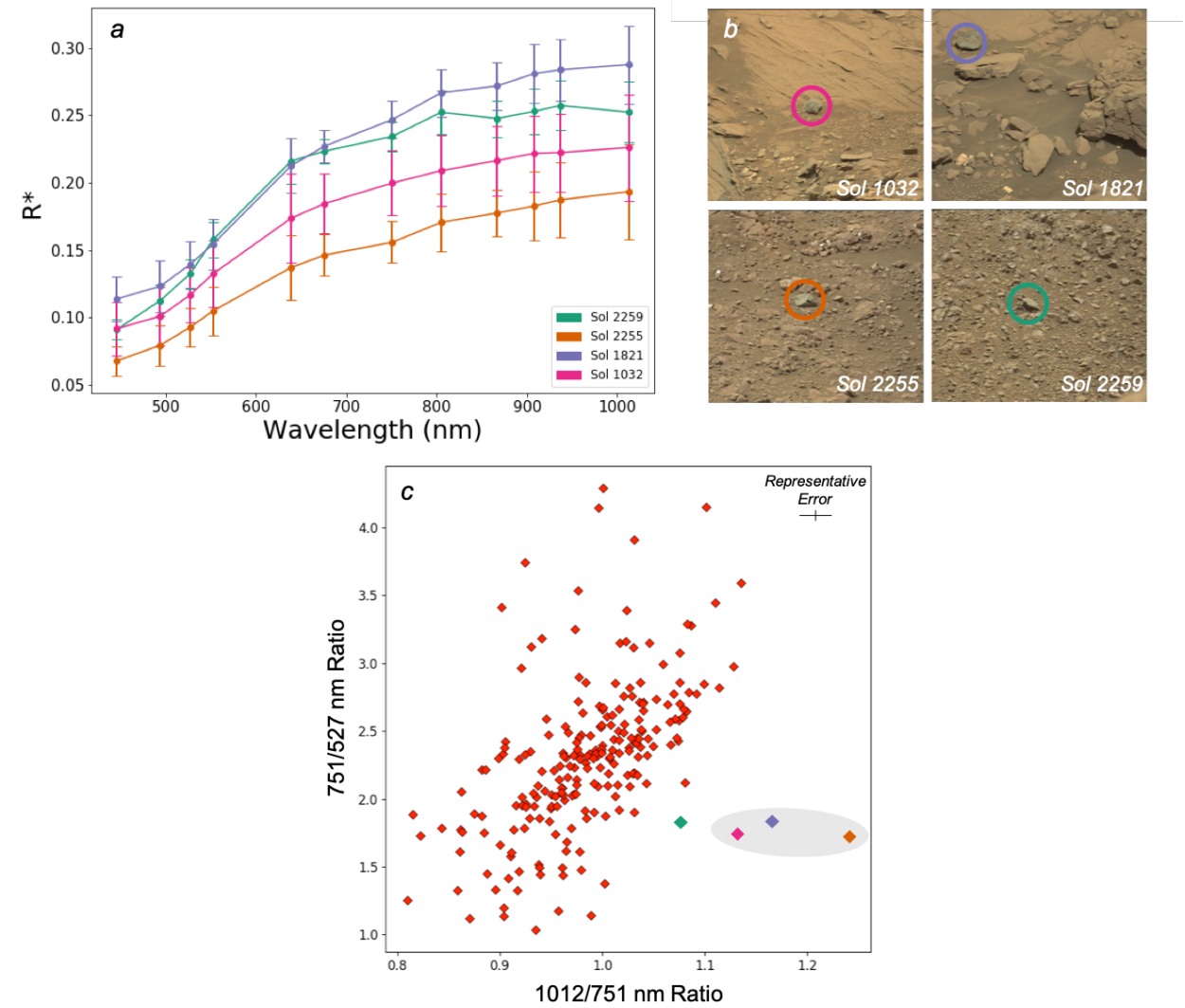

Figure 6. *Candidate and confirmed meteorites have grayish hues and overall positive visible to near-infrared slopes. (a) Mastcam spectra of four iron meteorite candidates. The sol 2259 target exhibits some spectral variability compared to the other three typical meteorite spectra. Spectra are averaged within each ROI and shown with one sigma error bars. (b) Mastcam RGB images of the four example candidate meteorites, with the fragments circled. Targets are Cottonwood (sol 1032, mcam04511), Mustards Island (sol 1821, mcam09401), Newburgh (sol 2255, mcam12069) and Gometra (sol 2259, mcam12088). (c) Parameter space plot comparing short and long wavelength ratios of all float rocks from sols 750-2302. Red diamonds indicate float in VRR observations previously identified to contain candidate meteorite fragments (Wellington et al., 2019). Gray oval highlights where outlier iron meteorite fragments plot in parameter space, with colors corresponding to examples in (a) and (b).*

4.3 Drill Fines

Like dust-cleared sections of rock, drill targets provide even more insight into the rocks' spectral properties; drill tailings, while varying in grain size and homogeneity, are largely free from dust and offer a bulk rock sample. Curiosity collected 14 drill samples from sol 750-2302, and Mastcam acquired 36 observations of drill tailings and 25 observations of subsequent dump piles, collectively referred to as "drill fines." Although the middle interval of the Murray formation has sparse drill samples due to broken hardware, every member was sampled by the drill (including Blunts Point, which was sampled during the eastern transect of VRR campaign). Spectra from drill fines present the same advantages of DRT spots, but to a much greater degree. In the sol 1118 Big Sky observation, we extract spectra from drill tailings, an adjacent DRT spot, and typical dusty bedrock surface (Figure 7). The drill tailings spectrum is much flatter than the other two, with a lower red-blue slope up to 751 nm and deeper absorption features, particularly at the longer wavelengths, than the dustier counterparts.

Throughout the traverse, spectra from drill fines are consistent with corresponding DRT spectra in 867 nm band depth, but tend to have lower red-blue slopes and shallower 527 nm absorption features in the lower Murray and at some VRR localities (Figure 8). Overall, VRR drill fines are more spectrally diverse in red-blue slope than dust-cleared and dusty targets. Juxtaposing spectra from these three feature types demonstrates the degrees to which dust masks spectra, but more importantly highlights which spectral features are most useful in the dusty rock spectrum to reflect the actual spectral signature of the underlying rock. Specifically, the slope from 805-1012 nm is consistent across all three spectra in Figure 7, and the 867 nm absorption feature is consistent across all target types in Figure 8.

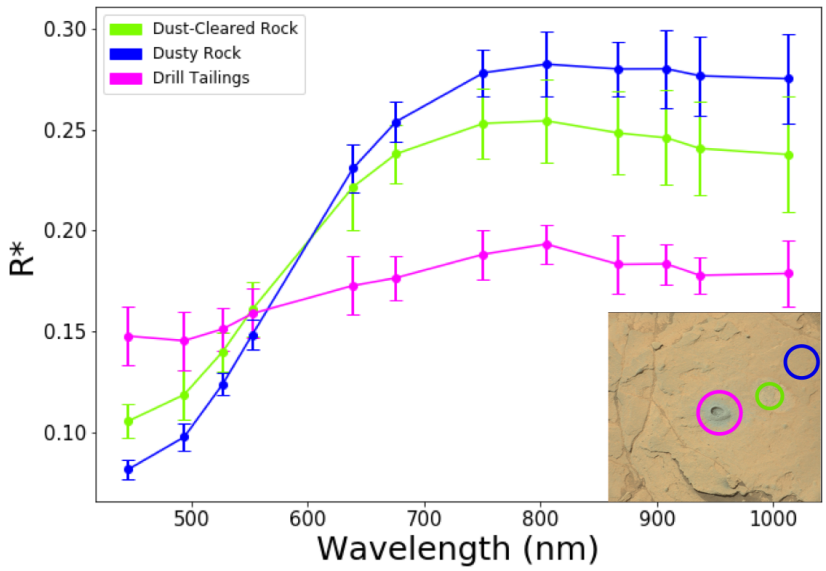

Figure 7. *Mastcam spectra extracted from adjacent dusty rock (blue), dust-cleared rock (green), and drill tailings (light purple). Drill tailings have a flatter red-blue slope and more prominent NIR spectral features. Inset Mastcam RGB image indicates ROI locations in Big Sky mini drill hole observation (sol 1118, mcam 04983; for scale, drill hole is ~16mm in diameter. Spectra are averaged within each ROI and shown with one sigma error bars.*

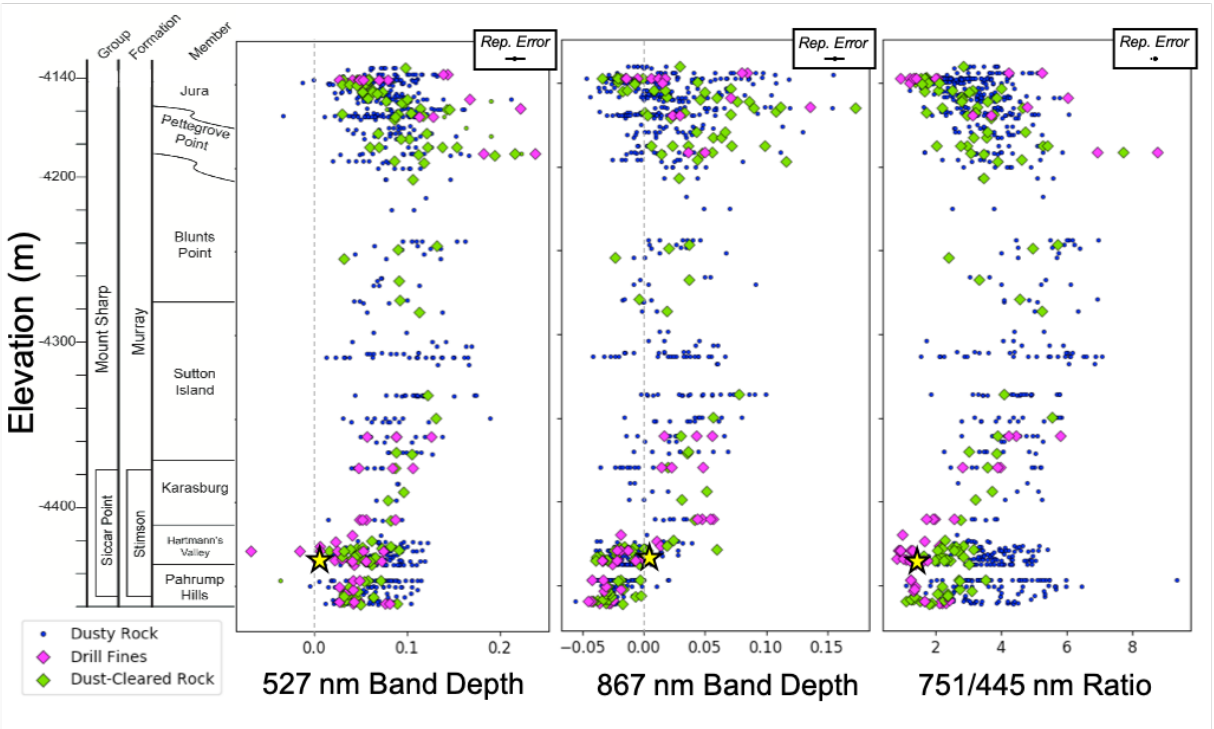

Figure 8. *Spectral variability for all dusty and dust cleared rocks (as in Figure 4), with the addition of all drill tailings and dump piles (together referred to as drill fines). Spectra from drill fines are consistent with corresponding DRT spectra in 867 nm band depth, but tend to have much lower red-blue slopes and shallower 527 nm absorption features in the lower Murray and at some VRR localities. Example target Big Sky drill tailings are indicated by yellow stars.*

4.4 Spectral Parameter Comparisons

4.4.1 Mastcam Spectral Classes

Analysis of dusty and dust-cleared rock surfaces, as well as drill fines, revealed several spectral "classes" which distinguish rocks from different stratigraphic units from each other. These spectral classes are largely informed by trends observed for the different feature types discussed above (*Sections 4.1-4.2*).

The Stimson formation can be identified by a zero to negative 867 nm band depth and negative NIR slope from 751 or 805 to 1012 nm (Figure 9). Positive band depth values are consistent with the presence of an absorption feature, while negative band depth values are not diagnostic. All but five Stimson targets have a zero to negative 867 nm band depth value, while Murray targets span a range from negative to very positive band depth values (almost 60% of Murray targets contain this absorption feature) (Figure 9). Therefore, the Murray rocks frequently exhibit the spectral signature consistent with fine-grained red crystalline hematite, while the Stimson formation does not. Similarly, a positive NIR slope is consistent with the 867 nm absorption feature, as spectra with a strong band slope upwards towards 1013 nm. All but six Stimson targets have a zero to negative NIR slope. Stimson spectra also tend to have a lower 527 nm absorption feature than many Murray formation targets (Figure 9). This trend is more easily identified in DRT targets and drill tailings than in dusty rock targets, likely due to dust spectra masking these spectral features.

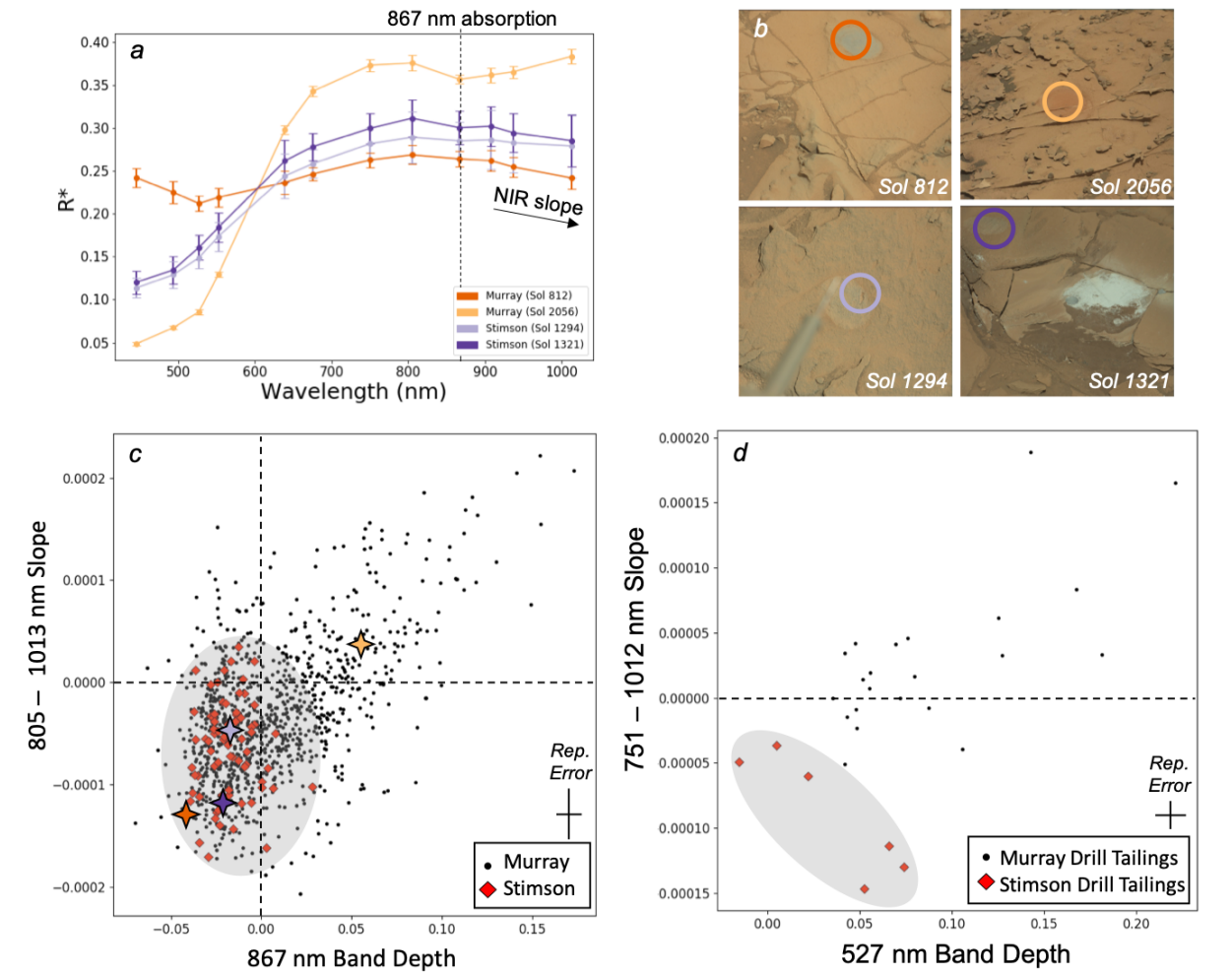

Figure 9. *Spectral comparisons of Murray and Stimson formation. (a) Mastcam spectra of four Murray and Stimson DRT targets, annotated with the two most distinctive parameters used to evaluate them: 867 nm band depth and NIR slope. Stimson targets represent typical Stimson spectra, and Murray targets reflect the spectral variability across the Murray formation. Spectra are averaged within each ROI and shown with one sigma error bars. (b) Mastcam RGB images of the four example targets, with ROIs where spectra were extracted from DRT spots circled. DRT spots are ~40mm in diameter. Targets are Mojave (Murray, sol 812, mcam03564), Duluth (Murray; sol 2056, mcam10897), Brukkaros (Stimson, sol 1294, mcam06144), and Lubango (Stimson, sol 132,1 mcam06305). (c) Parameter space plot comparing 867nm band depth and NIR slope for all Murray and Stimson rock targets. Stimson tends to have a zero to negative 867 nm band depth and negative NIR slope. Example targets from (a) and (b) are indicated with stars of corresponding color. (d) Parameter space plot comparing 527nm band depth and NIR slope for all Murray and Stimson drill tailings. Stimson targets tend to have no or small 527 nm absorption features, and very negative NIR slopes. VRR targets tend to plot in the upper-right portion of parameter space, with greater 527 nm band depths and NIR slopes than typical Murray. In both (c) and (d), Stimson targets are spectrally self-consistent, while Murray targets exhibit much greater variation in these parameters.*

While Stimson rocks appear to have more self-consistent spectral signatures, the Murray formation targets vary widely in these same spectral parameters, often independent of member designation. Heterogeneity within the Murray formation makes it difficult to confidently distinguish between individual members based on one or two spectral parameters alone. Differences in grain size and diagenesis (especially prevalent diagenetic features like veins and nodules) across the formation likely contribute to this variability. Horgan et al. (2019) explored some of the subtler spectral relationships in VRR, and showed that the 867 nm band depth and 640/527 nm ratio can be used to make subtle distinctions between Pettegrove Point and the different-toned subfacies within the Jura member. The presence of an 867 nm absorption feature and a strong 640/527 nm ratio in these units is consistent with fine-grained (red) crystalline hematite (Horgan et al., 2020). Applying the same ferric spectral parameters to the entire dataset, we find that three broad spectral classes emerge (Figure 10). The rocks of the lower Murray formation (Pahrump Hills, Hartmann's Valley, and Karasburg members), along with the Stimson formation **(**which unconformably overlies them), tend to have weak or no 867 nm absorption features and variable 640/527 nm ratios (Figure 10a). Sutton Island and Blunts Point both have weak to moderate 867 nm absorption features and are redder than the lower layers (Figure 10b). VRR members are more similar to each other than the other units, but slightly separate in this parameter space: Pettegrove Point spectra tend to have higher red/blue ratios and deeper 867 nm absorption features than Jura, while Jura spectra tend to have weaker absorption features and lower red/blue slopes (Figure 10c). The spectral variability within the Jura targets suggests a significant variability in crystallinity, grain size, and/or abundance of hematite in this unit (Horgan et al., 2019).

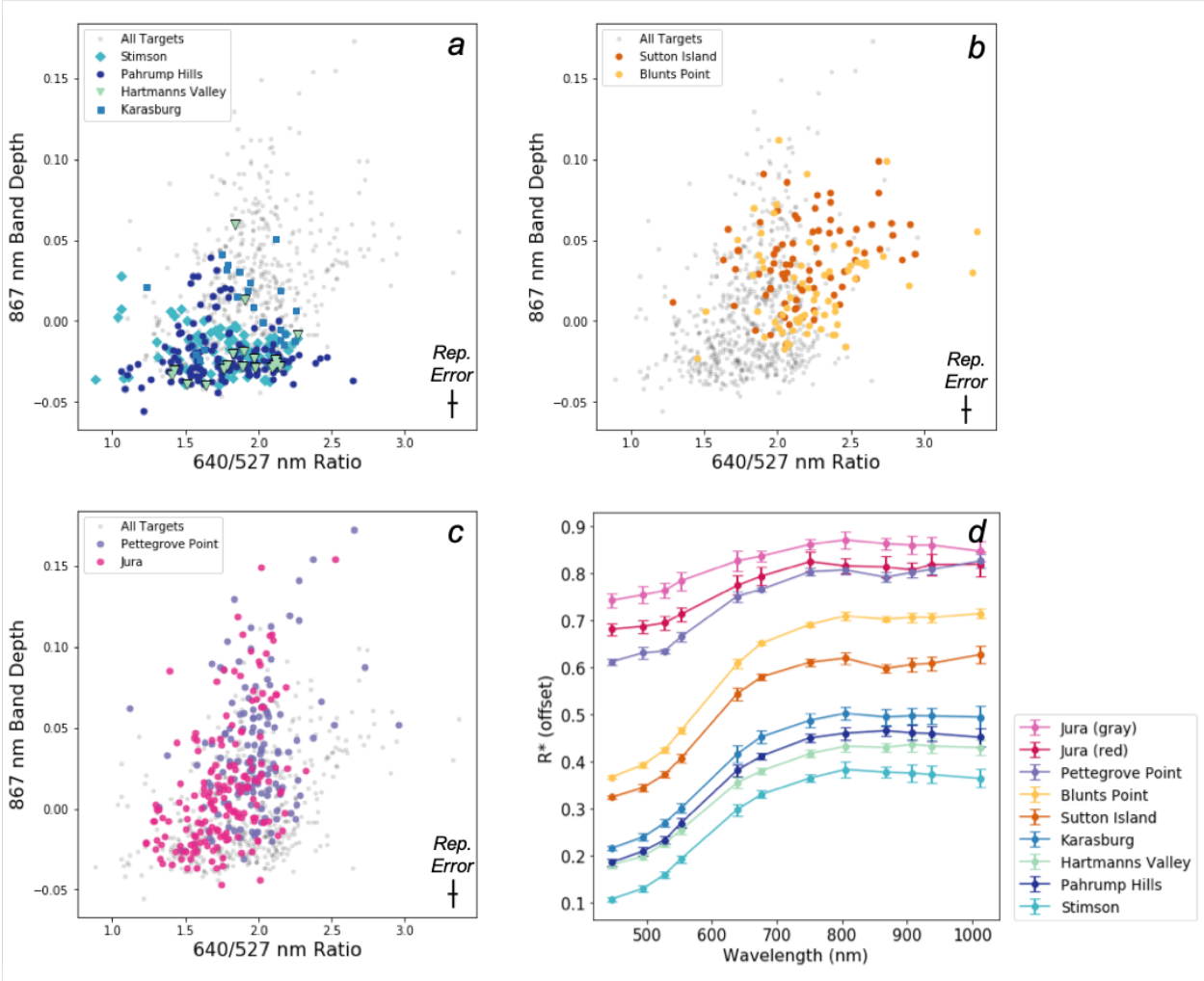

Figure 10. *Mastcam ferric spectral parameters for all dusty and dust-cleared rock targets from sols 750-2302, grouped by members according location in parameter space. Gray points on all plots indicate all dusty and dust-cleared targets. (a) Pahrump Hills, Hartmann's Valley, and Karasburg members, along with Stimson formation; (b) Sutton Island and Blunts Point members; (c) Pettegrove Point and Jura members. (d) Representative spectra from typical targets within each member, grouped by class and offset for clarity.*

4.4.2 Chemical Comparisons Across Instruments

ChemCam Passive spectra, with a similar but not identical wavelength range to Mastcam, show a statistically significant correlation for two iron oxide parameters measurable with both instruments: Mastcam's 527 nm band depth vs. ChemCam's 535 nm band depth, and Mastcam's 867 nm band depth vs. ChemCam's 750-840 nm slope (used a proxy for the 867 nm band depth, which is beyond ChemCam's wavelength range). Figure 13 shows example ChemCam passive and Mastcam spectra extracted from the same targets. ChemCam passive spectra were also convolved to Mastcam bandpasses; this allows us to more directly compare the same parameters

in both instruments: the 527 nm band depth (Test 1) and the 751-805 nm slope (Test 2). The convolved spectra are a robust representation of the raw spectra, though some additional noise is introduced in the convolution process: the linear relationship between ChemCam's 535 nm band depth and convolved 527 nm band depth has an R^2 value of 0.7741, and the linear relationship between the 750-840 nm slope and convolved 751-805 nm slope has an R^2 value of 0.9164.

Building on results presented in Fraeman et al. (2020), ChemCam passive (raw and convolved) and Mastcam parameters have a clear qualitative relationship (Figure 14). Because ChemCam passive measures a continuous spectrum, the Mastcam 527 nm band depths are compared to the more accurate iron oxide parameter with a band center at 535 nm (shoulders at 500 nm and 600 nm) in ChemCam (Test 3). We derive this more accurate parameter from laboratory spectra (Figure 1). The convolved ChemCam passive spectra consistently produce slightly deeper 527 nm band depths than either ChemCam or Mastcam (Figure 14, left). The Mastcam 867 nm band depth is compared to the ChemCam 750-840 nm slope values (again, with a negative slope reflecting an absorption feature beyond the measurable wavelength range; Test 4). Convolved ChemCam passive spectra tend to have less negative slopes than ChemCam passive spectra, which correspond to weaker 867 nm absorption features (Figure 14, right). Therefore, the convolution process produces spectra that overrepresent 527 nm band depths, and underrepresent 867 nm band depths.

Plotting these parameters against each other, we find that the R^2 values are relatively weak for all four comparison tests, and not entirely persuasive of a linear relationship (Table 3; Figure S1). With such similarly weak R^2 values, it is impossible to judge the strength of each test relative to the others. Therefore, to complement this linear regression, we calculate the covariance of the datasets in the four tests, which assesses the existence of a relationship (though not the strength of one) without presuming it is linear. All four tests of the data resulted in large positive covariance values, indicating a significant correlation between the Mastcam and ChemCam passive datasets (Table 3). Covariance can vary orders of magnitude depending on the magnitude of the input parameters, so the absolute covariance values cannot be compared from one test to another. For this reason, the covariance calculated in Test 2—for slope values, rather than band depth values—is much smaller than that calculated for the other tests. However, this value is considered a significant positive covariance value because it is much larger than any covariance value calculated using 10,000 random permutations of the dataset. Indeed, to ensure

each test's signal is above all noise, all covariance values were compared to covariance values calculated from 10,000 random permutations of their respective datasets (see Section 2. Methods). The resulting *p*-values for these tests were smaller than the desired significance level of 0.0125 (calculated by dividing the significance level of 0.05 by the four tests performed, according to the Bonferroni correction for multiple hypothesis testing) and therefore are statistically significant.

The methodology shown here is a robust statistical way to compare two instrument datasets that are not obviously correlated. It demonstrates strong relationships between the ChemCam passive and Mastcam datasets, which is intuitive because the instruments both collect reflectance spectra in similar wavelength ranges. In future work, we will use this method to assess less relationships between the Mastcam dataset and the chemistry measured by ChemCam and APXS, which are not obviously correlated. Specifically, we will compare the 527 nm and 867 nm band depths to iron abundances measured by these two instruments. Though ChemCam does not have the ability to distinguish between oxidized and non-oxidized iron, and Mastcam spectra correlate more with the presence of iron oxides than their abundance, it will be valuable to assess if there is a resolvable relationship between these parameters. Also, Czarnecki et al. (2020) demonstrated that high silica content correlates with spectrally bland Mastcam observations; therefore, it will also be valuable to compare the Mastcam parameters to silica abundance as measured by ChemCam and APXS.

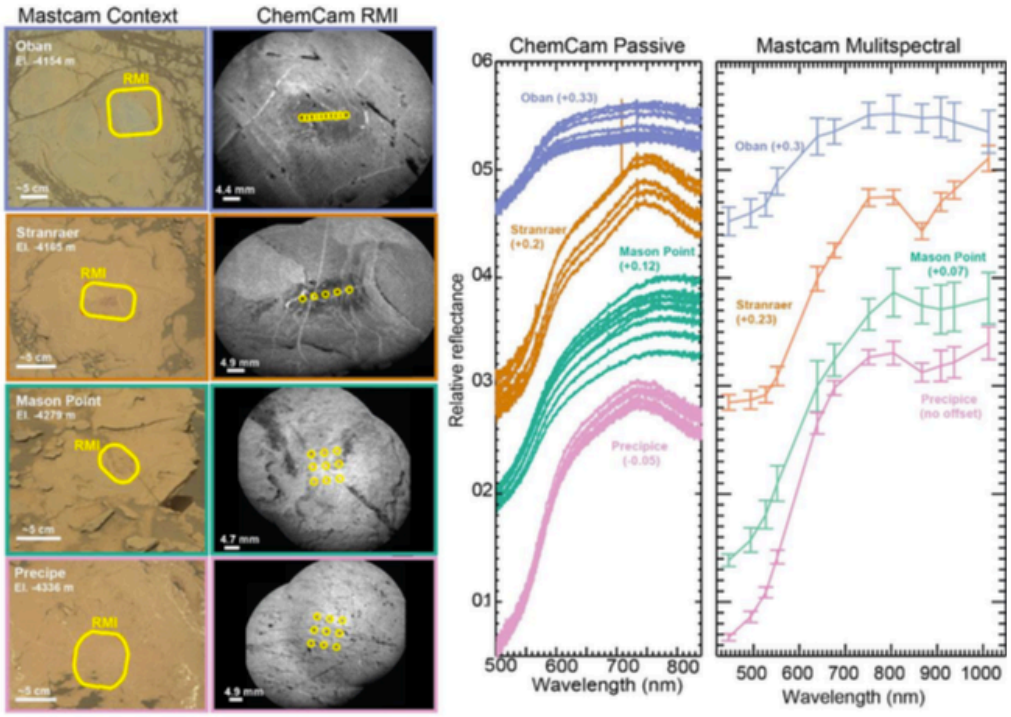

Figure 11. *Example ChemCam passive and Mastcam spectra extracted from the same four example dusty and dust-cleared rock targets, from Fraeman et al. (2020). Context Mastcam RGB images on the left show outline of ChemCam Remote Micro-Imager (RMI) field of view on the right, and RMIs show each ChemCam LIBS shot.*

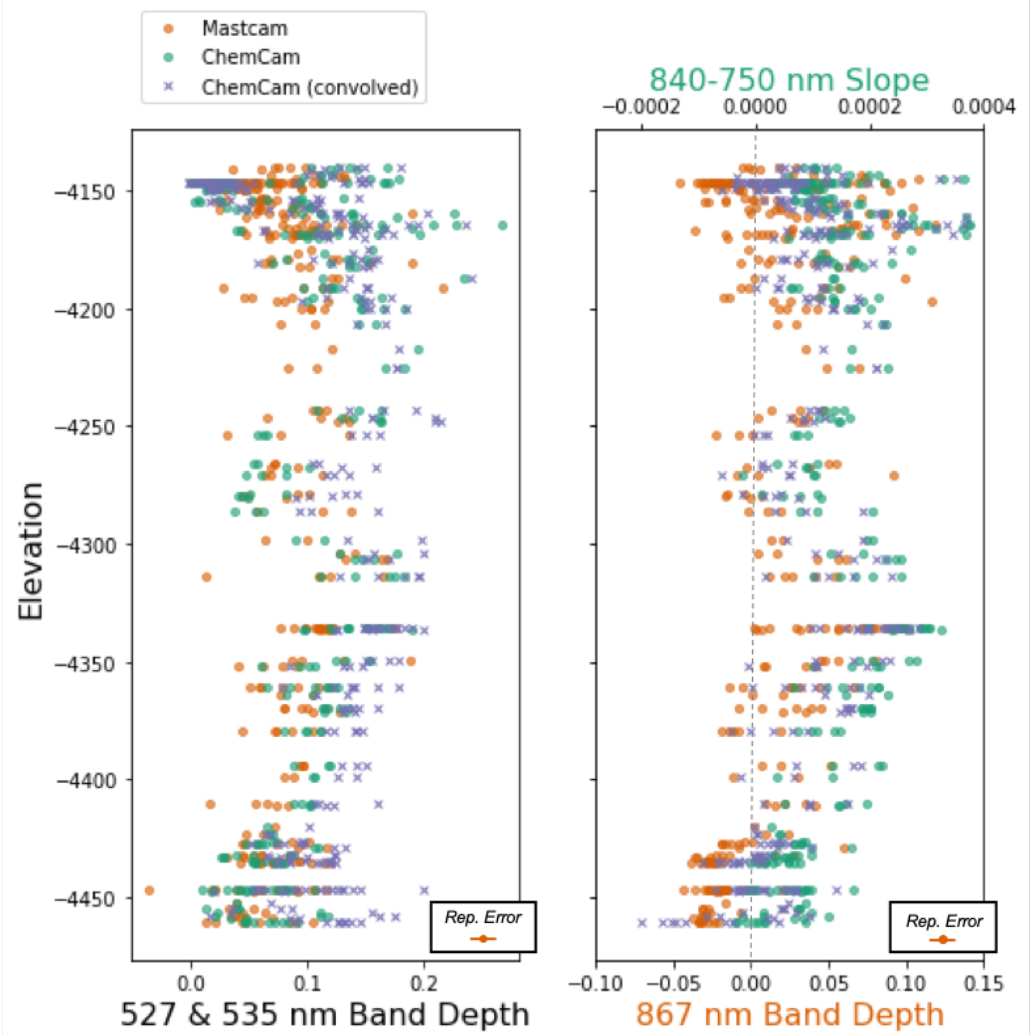

Figure 12. *Spectrostratigraphic agreement between Mastcam and ChemCam passive data for dusty and dust-cleared rocks at matching elevations. (left) Mastcam 527 nm (orange) and ChemCam passive 535 nm (green) band depths, with ChemCam passive convolved 527 nm band depths (purple x). (right) Parameters corresponding to the 867 nm absorption feature (Mastcam 867 nm band depths, ChemCam passive 840-750 nm slope, and convolved ChemCam passive 805-751 nm slope). Slopes are inverted so positive slope values correlate with positive band depth values.*

Table 3. Covariance analysis for Mastcam and ChemCam Passive spectra

Test	Mastcam Parameter	ChemCam Parameter	R^2	Covariance	*p*-value
1	527 nm Band Depth	527 nm Band Depth[a]	0.286	9.93×10^{-4}	<0.0001[b]
2	751-805 nm Slope	751-805 nm Slope[a]	0.154	5.93×10^{-9}	<0.0001[b]
3	527 nm Band Depth	535 nm Band Depth	0.331	1.07×10^{-3}	<0.0001[b]
4	867 nm Band Depth	750-840 nm Slope	0.378	1.98×10^{-6}	<0.0001[b]

[a] Calculated from ChemCam passive data convolved to Mastcam bandpasses
[b] The lowest *p*-value permutation test can resolve

4.5 Landscape-Scale Observations

Mastcam is a particularly useful tool to contextualize the chemistry of outcrops measured by other rover payload elements, and can be employed to investigate distant landscapes the rover will never itself drive. In rare instances, we can compare the spectra from distant targets to stratigraphically equivalent rocks observed in the rover's workspace, with more favorable viewing geometry. Red Cliff, a vertical exposure of rock on the north side of VRR, was observed in a landscape-scale mosaic captured on sol 2038 when Curiosity parked ~320 meters away on the edge of the ridge (Figure 13 a & b). Spectra extracted from the less dusty vertical face, as well as the dusty top of the outcrop, are largely consistent with typical Pettegrove Point spectra despite being two orders of magnitude farther away than other observations (Figure 13e). Here, we compare Red Cliff to the Voyageurs target (the first attempted drill in the Pettegrove Point member, with the highest hematite signature from orbit across the whole VRR) which was observed before and after the drill attempt failed to produce enough sample in the unexpectedly hard rock (Figure 13 c & d). Dusty rock spectra collected from the same location in both images varies slightly; the pre-drill spectrum has a lower red-blue slope, deeper 867 nm band depth, and steeper NIR slope. The post-drill spectrum has a red-blue slope, 867 nm band depth, and NIR slope more consistent with the Red Cliff spectra. The small differences between these two spectra reflect the subtle differences dust can make; drill-induced vibrations invariably move surficial dust around, affecting the variability across the outcrop and therefore the extracted spectra. It is possible that the hardness of the rock resulted in greater vibration during drilling, redistributing dust more than usual. Ultimately, the spectral similarity between Red Cliff and the post-drill Voyageurs observation confirms that major spectral features are discernable from a distance.

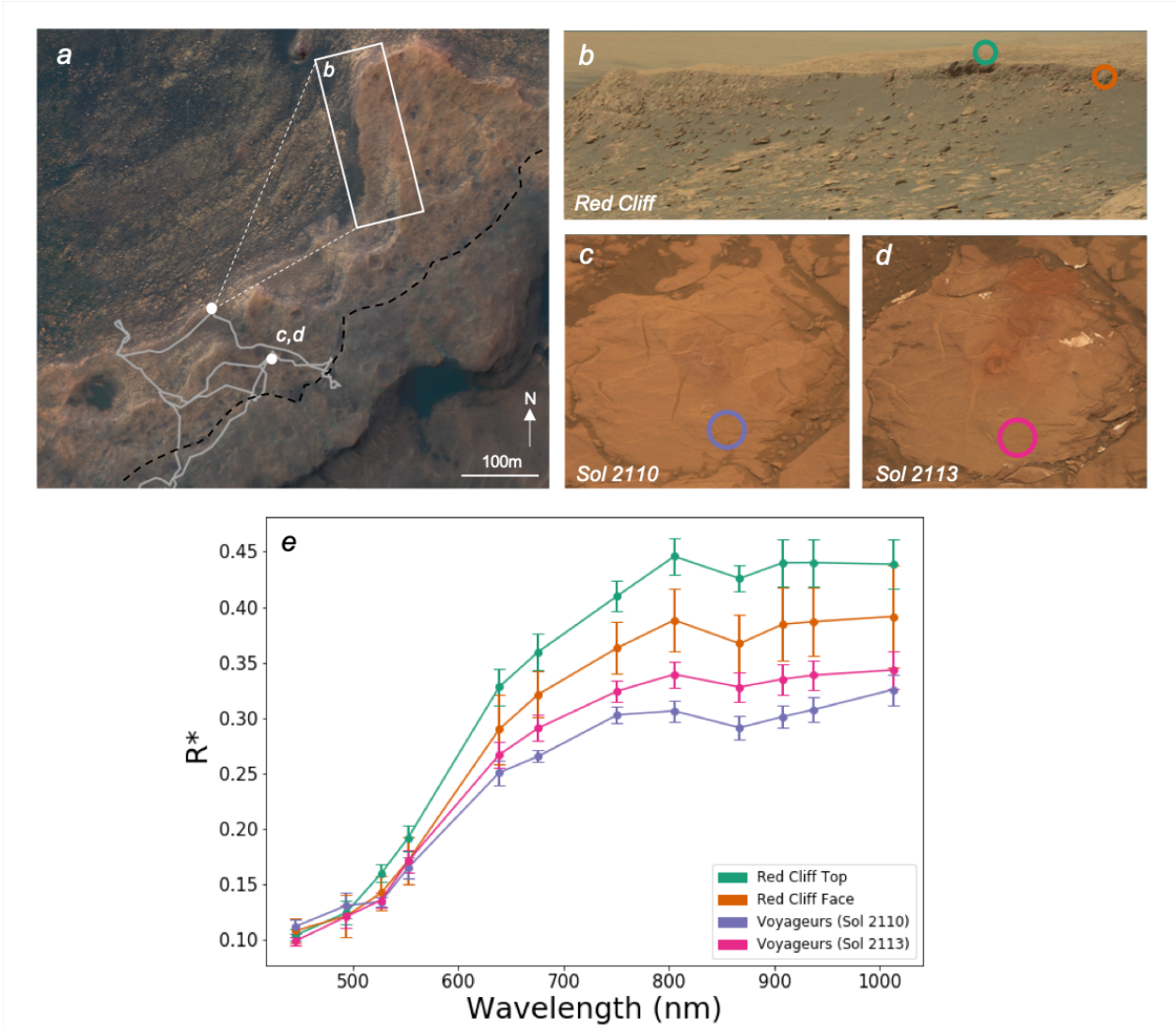

Figure 13. *Distant and proximal ROIs for Pettegrove Point member targets. (a) HiRISE context map of rover's eastern traverse of VRR (in gray), with locations of Red Cliff and Voyageurs observations indicated. Black dashed line separates Pettegrove Point (northwest) from Jura (southeast) members on VRR. (b) Mastcam RGB image of Red Cliff (sol 2038, mcam10762), a vertical exposure approximately 300 meters from the rover, with ROIs on both the less dusty rock "face" and the dusty, flat-lying "top" beyond. (c) Mastcam RGB image of the Voyageurs target as observed before drilling (sol 2110, mcam11271) and (d) after drilling (sol 2113, mcam11291), with dusty rock ROI locations circled. For scale, drill hole is ~16mm in diameter. (e) Mastcam spectra from the Red Cliff and Voyageurs targets. The Red Cliff ROIs are consistent with the Voyageurs spectra, which are observed from a more favorable geometry, though there are subtle differences between the Voyageurs observations due to mobile dust cover.*

5. Discussion

5.1 Complicating Factors in Interpreting Mastcam Spectra

This approach has several limitations, including large 1-sigma error bars in many parameter space plots. Caution should be exercised in interpreting subtle variations in spectral features/parameters. However, the similarities in trends reflected in datasets from multiple instruments (e.g., ChemCam passive spectra) demonstrate that interpretations made from this dataset do contribute to the overall characterization of Gale crater geology in this interval. A detailed discussion of limitations to this approach can be found in Part I.

In Mars Year 34 (2018), Curiosity's Rover Environmental Monitoring System (REMS) recorded a global dust storm—one where dust haze covers all longitudes over the majority of both hemispheres—as it reached Gale crater. This dust storm originated around sol 2060, reached Gale crater 15 sols later, and did not decline to climatological values until ~sol 2157 (Guzewich et al., 2019; Viúdez-Moreiras et al., 2019). Dust storms of this magnitude periodically sweep the surface of Mars, and during the preceding 2007 event, the Mars Exploration Rover Opportunity observed apparent albedo increases with the Pancam instrument (Mastcam's precursor) due to the resulting redder illumination conditions (Rice et al., 2018).

Atmospheric opacity is measured as tau, and increases exponentially with increasing tau values. Tau values were much higher than average during the extent of the dust storm, and the resulting redder illumination conditions could have impacted Mastcam imaging. However, the Mastcam observations acquired during these high tau conditions were not systematically redder than usual (Figure 14). Therefore, the dust storm had no measurable effect on Mastcam multispectral imaging acquired during the event, and the spectra acquired during this sol range can be directly compared to those acquired under typical illumination conditions.

While this initial assessment verifies that the dust storm itself did not result in false reddening of the spectra, there does appear to be a correlation between redness and tau as observed over the entire course of the mission that requires further investigation.

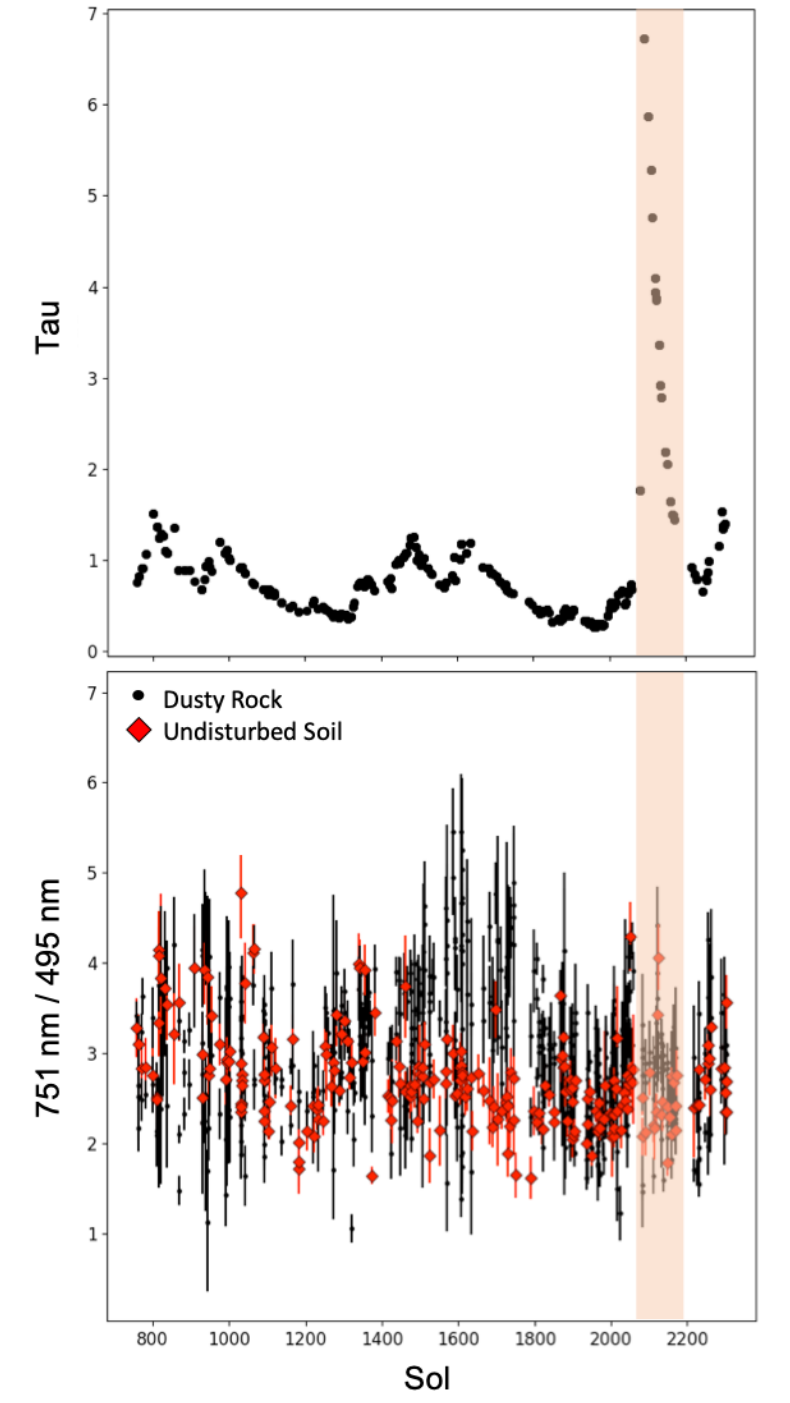

Figure 14. *Tau (top) and "redness" (bottom) by sol for all dusty rock (black) and undisturbed soil (red) targets observed from sol 750-2302. High tau values measured during the global dust storm did not result in a reddening of Mastcam reflectance values; in the highlighted sol range, they are consistent with the range of redness observed throughout the 3500 sols presented.*

5.2 Spatial Distribution of Spectral Classes and Geological Interpretations

The "spectrostratigraphic" plots throughout this paper provide key insight into the spectral trends as Curiosity has explored them within Gale crater. Here, we investigate the relationship between three key spectral parameters (867 nm band depth, 527 nm band depth, and NIR slope) and the stratigraphic boundaries of this sequence (Figure 15). The lower Murray formation—Pahrump Hills in particular—has a narrower range of band depths and slopes than the rest of the stratigraphy. Indeed, the weak or absent 867 nm absorption feature—one of the parameters distinguishing Stimson from Murray—is consistent across this interval. While the Murray may exhibit greater variability overall, it is locally spectrally similar to the Stimson. The relationship between Stimson and similar caprocks to the underlying Murray material, particularly how the caprock may influence diagenesis and ultimately the spectral signatures consistent with iron oxidation, requires further study.

Both the 867 nm and 527 nm band depths vary similarly over the entire stratigraphic section, though there are few targets with no 527 nm absorption (while there are many without an 867 nm feature). These parameters are well confined to stratigraphic boundaries below VRR. Weak or absent bands in the Pahrump Hills and Hartmann's Valley members give way to increased absorption in the Karasburg member, and the increasing trend continues into Sutton Island. These values peak mid-Sutton Island, and decline into Blunts Point. A scarcity of data obscures any upper Blunts Point trends, but the transition into Pettegrove Point is marked by an increased spread of band depth values. Pettegrove Point and Jura are hardly distinguishable with these singular spectral parameters, but rather represent the most spectrally diverse units encountered to date.

The NIR slope is much more varied in the lower Murray than the absorption features are. In Pahrump Hills, dust-cleared rocks only have negative NIR slopes, while the dusty rocks have both positive and negative in equal magnitudes. Hartmann's Valley is similar, but includes a few DRT targets with positive slopes. Slopes decrease across the Karasburg member, and then vary widely through Sutton Island, with a slight skew towards negative slopes. Lower Blunts Point has positive slopes, while upper Blunts Point has very negative slopes. VRR units are difficult to discern at this scale (for detail, see Figure 16).

Each lithology varies substantially in grain size, color, texture, and even depositional and diagenetic history. These variations are consistent with the widely varying spectral signatures within these units.

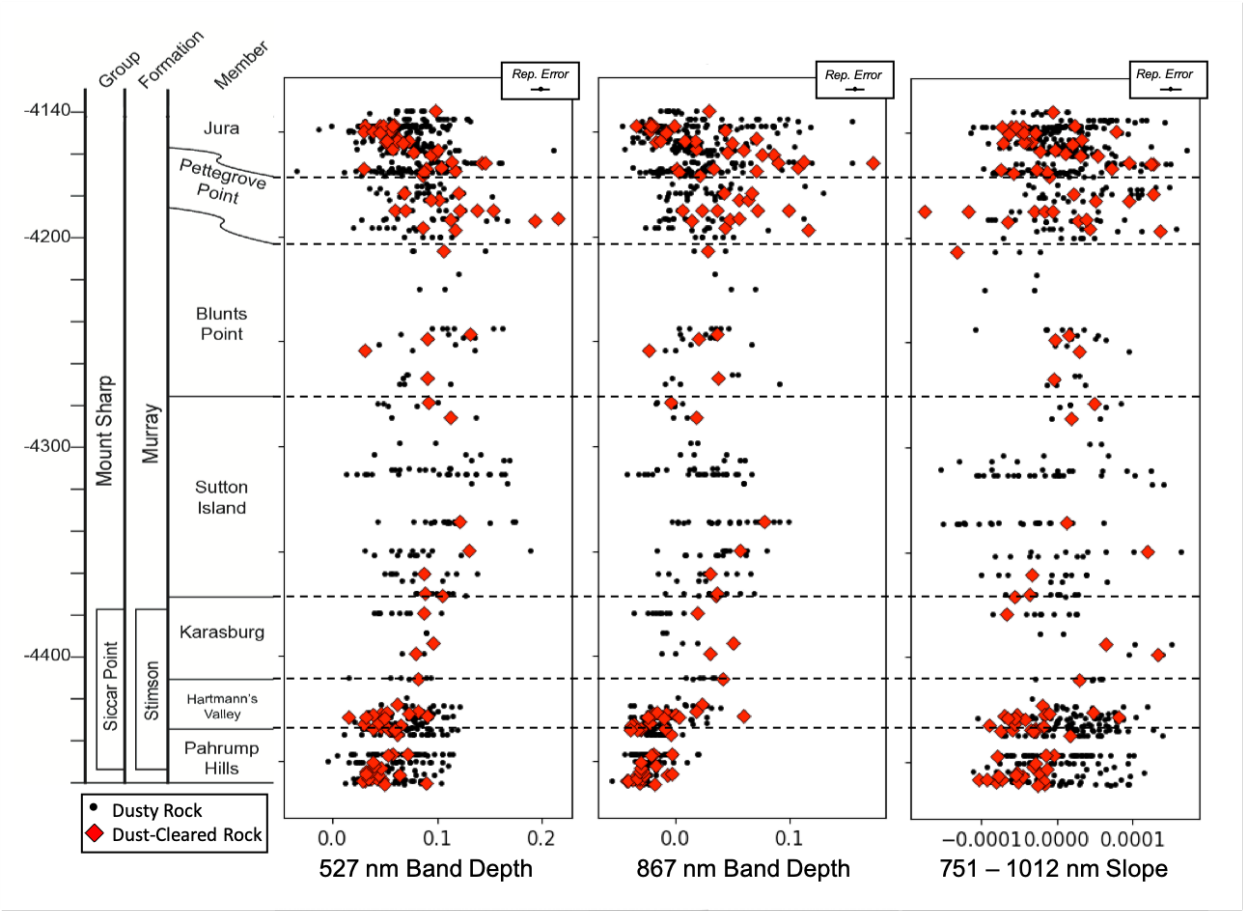

Figure 15. *Spectrostratigraphic plots of all dusty and dust-cleared targets observed by Mastcam from sol 750-2302, correlated with stratigraphic units indicated on schematic stratigraphic column. Note that a single dashed line at the base of the Jura and Pettegrove Point members does not capture the variable unit boundaries represented by a zig zag on the stratigraphic column.*

The VRR campaign involved three transects across the ridge in which the Blunts Point, Pettegrove Point, and Jura members were all observed at inconsistent elevations. Blunts Pont stands apart from VRR units spectrally in 527 nm band depth and NIR slope, but the Pettegrove Point and Jura spectra do not necessarily separate around member boundaries (Figure 16). While Pettegrove Point and Jura spectra have widely varying 867 nm band depths, Jura has many more spectra lacking the absorption feature than Pettegrove Point does. Both are more spectrally diverse than all of Blunts Point. For the 527 nm band depth, Pettegrove Point is very consistent with Jura save a handful of targets at ~ -1460 m with deeper bands. Interestingly, where

Pettegrove Point and Jura overlap, they are more spectrally similar to each other than the overall range of values exhibited (e.g., at ~ -1470 m, Jura and Pettegrove Point targets cluster together).

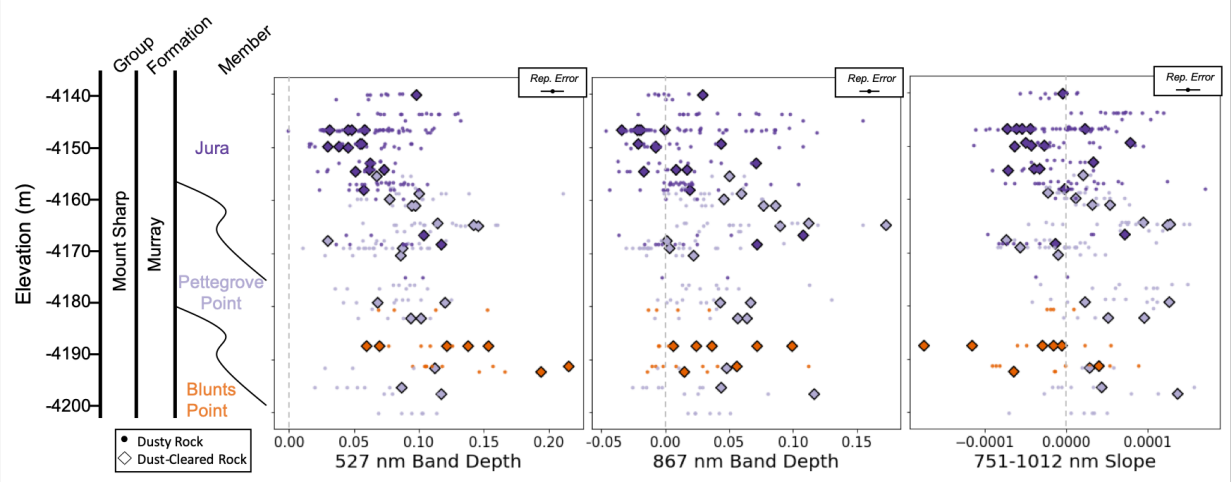

Figure 16 *Spectrostratigraphic plots for all dusty (dots) and dust-cleared rocks (diamonds) observed during VRR campaign. Units are colored according to stratigraphic column. Though Blunts Point is not a VRR unit, it was observed at the same elevation as Pettegrove Point deposits.*

Spectral and chemical trends within VRR suggest multiple stages of diagenesis, with both early and late fluid flow causing highly variable crystallinity, grain size, and texture of iron oxides (primarily hematite) across the ridge itself (Horgan et al., 2019). The much higher variance in iron oxide spectral signatures in VRR targets than any other member encountered in the Murray formation (Figure 15) corroborates the hypothesis that VRR exists as a topographic ridge due to greater degrees of diagenetic alteration than the surrounding terrain (Fraeman et al., 2020). The boundaries between Blunts Point, Pettegrove Point, and Jura are not confined to horizontal strata, and the VRR members are difficult to distinguish spectrally. Because the other members of the Murray formation do have clear boundaries and spectral identities, the iron oxides on VRR are the result of complex diagenesis, while iron oxides distributed throughout the rest of the Murray formation likely had a stronger depositional component, and/or did not experience the duration or magnitude of fluid flow that VRR did. Fraeman et al. (2020) suggest that proximity to Siccar Point group deposits may have increased alteration due to sedimentary controls on fluid paths; however, the lower Murray formation, where Curiosity also explored the unconformably overlying Siccar Point Stimson formation, has far less spectral diversity and variability in iron oxide-related parameters. Ultimately, these spectral signatures mapped

throughout the traverse present a new tool to contextualize orbital scale interpretations of the interactions between Siccar Point group and the underlying lacustrine sediments. It is likely that the interface between these rocks was only one of the many influences on timing and degree of alteration in the Murray formation, as the distribution of diagenetic signatures along the rover's traverse points to highly variable aqueous conditions for an extended period of time in a relatively small part of Gale crater.

5.4 Comparisons to Other MSL Datasets and Orbital Trends

Drawing links between orbital and wheels-on-the-ground spectral signatures is an essential facet of Mars exploration. Orbital data informs where rovers should explore, and then high-resolution ground-based data informs the larger-scale models built on those orbital datasets. VRR was initially identified as a target of interest due to anomalously high spectral signatures detected by the Compact Reconnaissance Imaging Spectrometer for Mars (CRISM) corresponding to red crystalline hematite, which was inferred to have either precipitated from anoxic Fe^{2+} groundwater in an oxidizing environment, or formed from in-place silicate weathering (Fraeman et al., 2013). Curiosity's exploration of VRR revealed that the deep absorption features that make this region distinctive from orbit can be attributed to varying ferric oxide grain size and crystallinity, highlighting the importance of ground-truthing potentially ambiguous orbital signatures (Fraeman et al., 2020). Iron oxide spectral parameters for CRISM, ChemCam passive, and Mastcam all demonstrate qualitative agreement (Fraeman et al., 2020). However, CheMin X-ray diffraction measurements of ferric phyllosilicates better correlate with variations in Mastcam's 867 nm absorption feature than CheMin-derived crystalline hematite abundance (Jacob et al., 2020). The full characterization of VRR on the ground confirmed the orbital-based hypothesis that hematite was formed by recrystallization during interactions with diagenetic fluids (Fraeman et al., 2020). Our study contextualizes the highly variable spectral signatures of VRR, and quantitatively demonstrates that they differ from the rest of the Murray formation.

The Bagnold Dune Field, a collection of dark mafic sand in a topographic low, was another distinctive feature analyzed from orbit and the ground. Seelos et al. (2014) identified variations in CRISM mafic mineral signatures (i.e. olivine and high-calcium pyroxene) that appeared to correlate with dune type and grain sorting (especially olivine enrichment on the

upwind margin of the dune field); these observations were corroborated by Curiosity's observation of the dune field, where it found that the zones of stronger olivine signatures were qualitatively correlated with zones of inferred lower dust cover and higher fluxes (Lapotre et al., 2017).

Because of their range—from under the rover's wheels to hundreds of meters distant—multispectral observations can act as an intermediate between these orbital datasets and ground-based datasets. We have demonstrated that spectral signatures acquired at distance retain the necessary spectral features to correlate them with stratigraphic units (Figure 13). Therefore, they expand the rover's reach offer a better comparison to the scale of spectral trends observed from orbit. Moreover, these observations can provide context for units along Curiosity's path long before it reaches them. However, landscape scale observations of Mount Sharp units beyond VRR exceed the scope of this work.

Zooming in further, we have shown that the Mastcam and ChemCam passive datasets complement each other to a significant degree. The spectral parameters measured and used as inputs for the covariance analysis are significantly correlated, demonstrating that the shorter wavelength range of ChemCam passive does not affect our ability to detect diagnostic spectral features, and Mastcam spectra sufficiently capture Fe-oxide spectral behavior, despite having band centers at slightly different wavelengths than the "ideal" band centers (i.e., 527 nm vs. 535 nm). However, convolving ChemCam passive spectra to Mastcam bandpasses provided valuable insight into exactly how well these lower resolution versions of the spectra capture Fe-oxide behavior. The convolved spectra consistently over-represent 527 nm band depths, and under-represent 867 nm band depths (Figure 14), and do not have a perfect linear relationship with their unconvolved counterparts. Therefore, this cross-instrument calibration reveals that Mastcam is not able to characterize the full extent of Fe-oxide behavior in this region of the spectrum. However, the complementary datasets produced by these instruments tell a much more complete story, and provide essential context for the chemical and mineralogical measurements made on the ChemCam passive target scale.

5.5 Implications for Curiosity's Ongoing Investigation at Mount Sharp

Defining broad spectral classes for the different members of the Murray formation (as in Figure 10) creates a valuable baseline to compare new observations to as they are continually

collected throughout the MSL mission. After leaving VRR on sol 2302, Curiosity descended into the Glen Torridon region, which boasts Al/Fe phyllosilicate signatures from orbit (Fraeman et al., 2016). Future work includes investigating how spectral signatures of Glen Torridon compare to the entire Murray formation dataset in order to gain insight into the sediments and better understand their relationship to VRR. As Curiosity continues its climb up Mount Sharp, it will likely encounter new capping units—which may be spectrally similar to the Stimson formation capping sandstones—and ultimately leave the Murray formation behind. Because we have established that multispectral landscape-scale mosaics retain the spectral signatures of rocks at distance, we can use Mastcam to better understand the composition of outcrops the rover will visit soon, as well as places it will never drive—particularly if interpretations of those observations can be calibrated by our spectral characterization of the entire traverse through VRR.

6. Post-VRR Analyses

All results presented up to sol 2302 are part of the aforementioned manuscript as a collaborative work with members of the MSL Science Team. The rover did not stop driving, however; results from analyses of the region explored beyond VRR, through sol 2755, are presented in this section as my own work.

Glen Torridon Background

After departing the Vera Rubin ridge on sol 2302, Curiosity descended into Glen Torridon (GT), a trough-like region with Al/Fe phyllosilicate spectral signatures detected from orbit (Fraeman et al., 2016). Though Glen Torridon strata occupy a topographic low south of the VRR, the unit is continuous upslope to elevations higher than the VRR (Figure 17). Along Curiosity's traverse, it is bounded to the south by the Greenheugh Pediment, a fan-shaped feature composed of Siccar Point aeolian sandstones unconformably overlying the Murray formation. At the time of writing, Curiosity has driven nearly two kilometers and explored ~70 vertical meters of strata in the Glen Torridon region, from the lowest point just south of the Vera Rubin ridge explored on sol 2409 to the top edge of the Greenheugh Pediment, reached on sol 2702. This region is dominated by a continuation of the Jura member of the Murray formation, topped by a coarser grained Knockfarril Hill member and an as-yet-unnamed "fractured intermediate

unit." At the southern end of the Glen Torridon region rises the Greenheugh Pediment, a fan-shaped feature capped by a Siccar Point group aeolian sandstone, unconformably overlying the Murray formation rocks below.

The Glen Torridon Jura member can be divided into three types based on morphology observed by Mastcam: coherent, rubbly, and pebbly. Coherent Glen Torridon Jura consists of cohesive outcrop, often cross-stratified blocks. Fractured and rough-textured laminated mudstones comprise the rubbly type, and cm-scale pebble-strewn lags of former outcrop comprise the pebbly type. The rubbly and pebbly deposits are associated with high K and low Mg, as measured by ChemCam and APXS, while the outcrop-forming coherent deposits are associated with a low K, high Mg chemical endmember (Bennett et al., 2019).

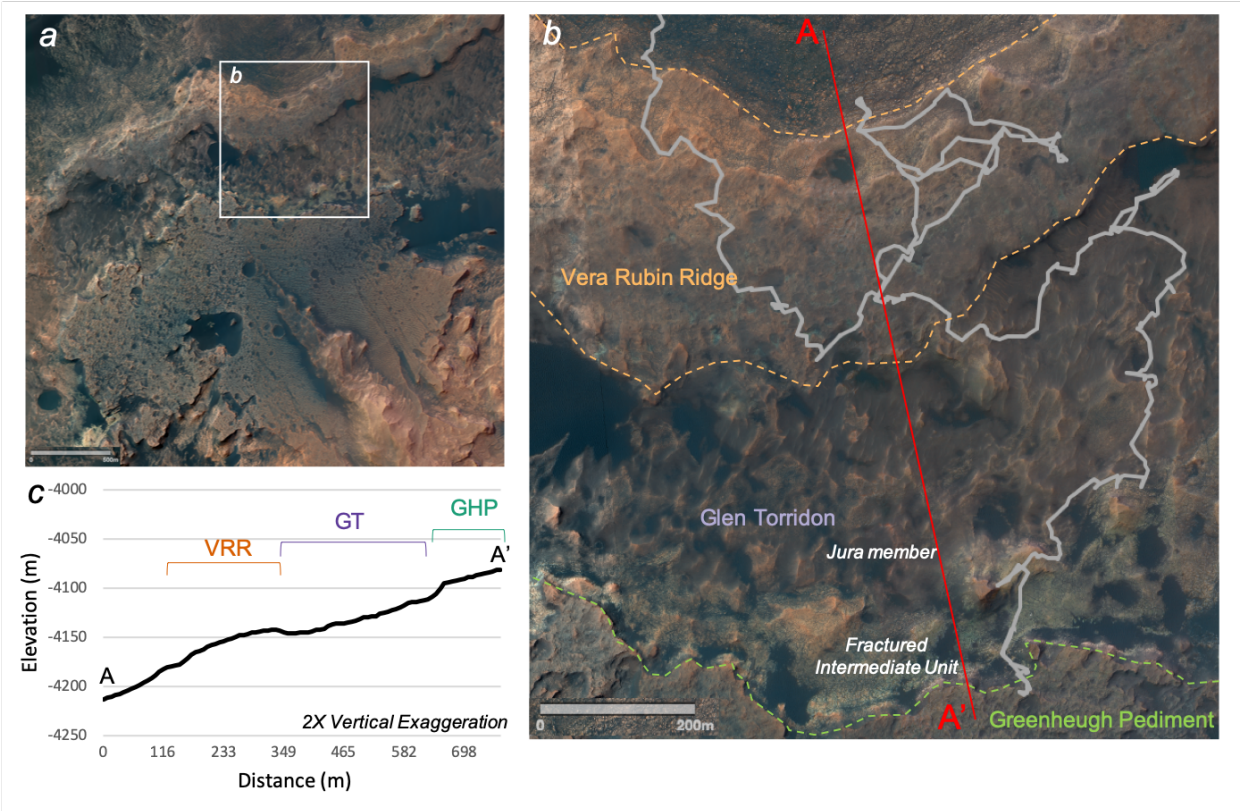

Figure 17. *Geologic context for Curiosity's traverse post-VRR. (a) Regional context, including Vera Rubin ridge and fan-shaped Greenheugh Pediment. (b) Detail of post-traverse units discussed, including both the Jura member and Fractured Intermediate Unit of Glen Torridon and the briefly-sampled Greenheugh Pediment. Red line indicates cross section in (c), which shows (with 2X vertical exaggeration) the topography of the ridge (VRR), trough and slope (GT), and pediment scarp (GHP).*

Glen Torridon Spectral Variability

Glen Torridon Jura sub-types exhibit loose correlations with positive and negative near-IR slope (from 937-1013 nm), though spectrally are much harder to distinguish than chemically. Type examples of end-members show the textural variety in Glen Torridon Jura (Figure 18). Pebbly targets are most spectrally self-consistent; all but two pebbly targets have a negative NIR slope, and spectra from pebbly targets have the lowest slopes observed (Figure 19). Coherent targets, however, are much more variable; though the majority have positive NIR slopes, there are many targets with negative slopes (Figure 19). Rubbly targets are sparse compared to the other two, and exhibit spectral signatures that match both pebbly and coherent targets (Figure 19). Therefore, it is difficult to determine the origin of the pebbly material from spectra alone; chemical similarities measured by ChemCam indicate that pebbly material is likely derived from rubbly material (*Dehouck et al., 2019).*

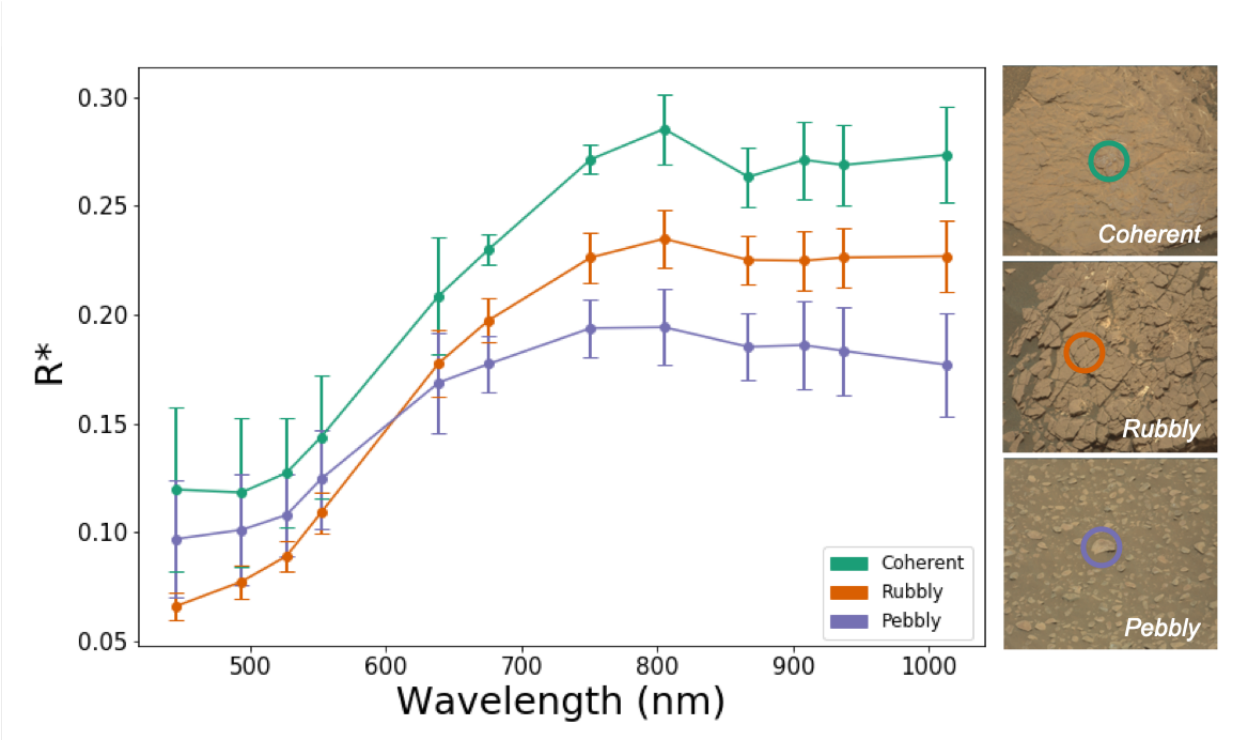

Figure 18. *Spectral signatures of three type examples of the GT Jura subfacies: coherent, rubbly, and pebbly. (left) Mastcam spectra of the three examples, averaged within each ROI and shown with one standard deviation error bars. (right) Mastcam RGB images of coherent, rubbly, and pebbly target spectra extracted from circled ROIs. Targets are Curlew (coherent, sol 2320, mcam12405), Muir of Ord (rubbly, sol 2351, mcam12472), and Little Minch Strathspey (pebbly, sol 2435, mcam12909).*

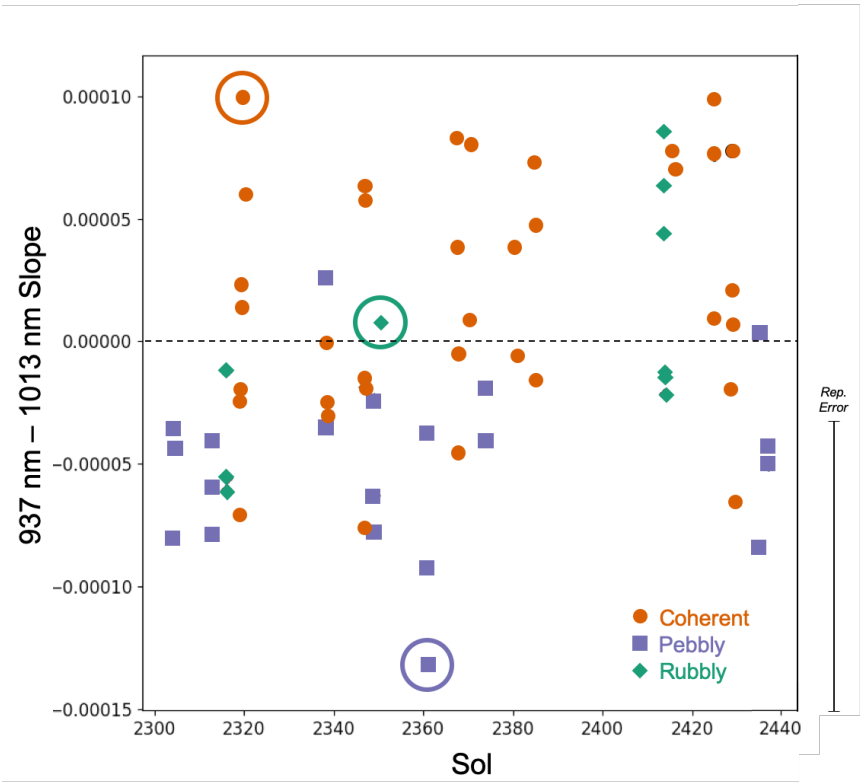

Figure 19. *GT Jura subfacies loosely separate in parameter space by NIR slope from 937-1013 nm. Coherent (orange dots) and pebbly (purple squares) materials can be loosely separated, but rubbly materials (teal diamond) have spectral signatures matching both coherent and rubbly targets. Example targets from Figure 18 are circled.*

Greenheugh Pediment Capping Unit

Curiosity continued its exploration across the Glen Torridon region and all the way on top of the Greenheugh Pediment. Murray formation rocks just under the capping sandstone of the pediment are more heavily altered than those lower down. Drill samples were collected in Glen Torridon (two adjacent drill holes were named Glen Etive), material just under the pediment cap (dubbed Hutton), and the pediment cap itself (Edinburgh). Both Hutton and Edinburgh have much flatter spectra (Edinburgh has a flatter red-blue slope than Hutton), a NIR downturn (particularly 908-1012 nm), and an absorption feature at ~680 nm (Figure 20). This absorption feature also appears in gray/mottled Jura spectra, and is consistent with coarse gray hematite (Horgan et al., 2020).

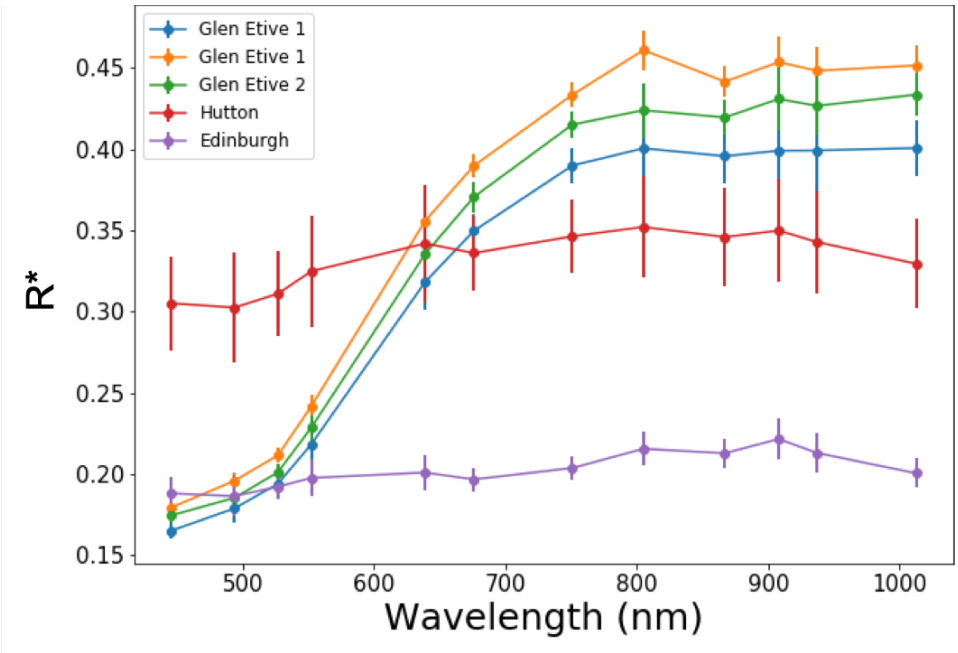

Figure 20. *Mastcam spectra of post-VRR drill tailings collected from Glen Torridon (Glen Etive), just below the Greenheugh Pediment (Hutton), and on top of the pediment (Edinburgh). Spectra are averaged within each ROI and shown with one standard deviation error bars.*

Curiosity acquired several Mastcam landscape-scale observations of the pediment capping sandstone and underlying units as the rover approached for ascent. Spectral variations across the outcrop correspond to the lower laminated bedrock, altered/weathered bedrock directly beneath the cap, and the capping sandstone itself (Figure 21). Several spectra extracted from this outcrop have an absorption feature in the vicinity of ~680 nm, but given the spacing of the left and right eye filters in this wavelength range, the band minimum and width is challenging to characterize; instead, the negative 640-676 nm slope can be used as the best quantitative measurement of the strength of this absorption feature (Figure 21a). The lower, vein-rich portion of the outcrop appears darker in the slope map, and therefore contains this absorption feature while the upper smooth, dust-covered surfaces do not express it (potentially due to variable dust cover and outcrop geometry produced by different rock textures). The less dusty capping unit float blocks also exhibit negative slopes (and, consequently, the absorption feature). Because this feature is present in both the capping unit and the underlying material, but not in all spectra in the scene, it is not an image artifact.

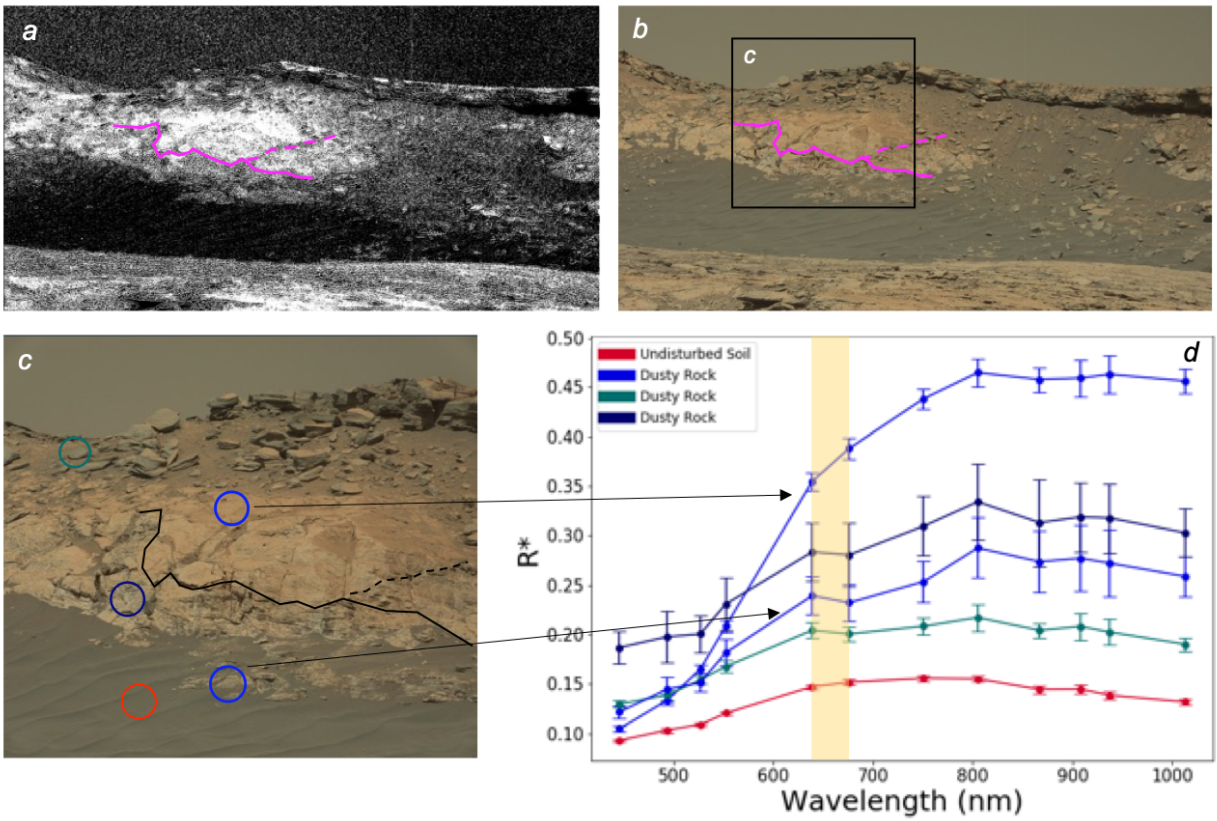

Figure 21. *Spectral variations across the capping sandstone and underlying material correlate with the stratigraphic boundaries between laminated bedrock, altered/weathered bedrock, and capping sandstone. (a) Mastcam left eye slope map for 640-676 nm slope as a proxy for 676 nm band depth. Darker regions reflect negative slope (and therefore positive band depth). Magenta trace delineates lower, vein-rich portion of outcrop from upper, smooth, dust-covered surfaces. (b) Mastcam left eye RGB image of region in (a), with Mastcam right eye outlined and shown in (c), where ROIs where spectra were extracted are circled. (d) Mastcam spectra of dusty rocks below and in the capping sandstone. 676 nm absorption feature is present in both capping sandstone and underlying material; yellow bar highlights 640-676nm slope corresponding to absorption feature. Spectra are averaged within each ROI and shown with one standard deviation error bars, and all images are from sol 2609 (mcam13704)..*

This ~680 nm absorption feature is not exclusive to the Greenheugh Pediment interface; rather, it appears in two dominant pulses throughout the traverse as well as in stray float pebbles (Figure 22). The lower elevation pulse at about -4440 m consists of dominantly Stimson formation targets, mixed with some Pahrump Hills targets. As previously demonstrated, the rocks of the Pahrump Hills member share many spectral characteristics with the proximal Stimson formation rocks (e.g. Figure 11). The upper elevation pulse contains some VRR targets

(especially the Highfield and Lake Orcadie drill tailings) around -4150 m, and the uppermost set of targets around -4110 m are from the capping sandstone and underlying units. Because the Stimson formation spectra dominantly do not contain the 867 nm absorption feature consistent with red, fine-grained hematite, it is notable that many have the 676 nm absorption feature consistent with coarse gray hematite—particularly because drill samples only contain between 1.1 and 6.0 weight percent hematite (Yen et al., 2017).

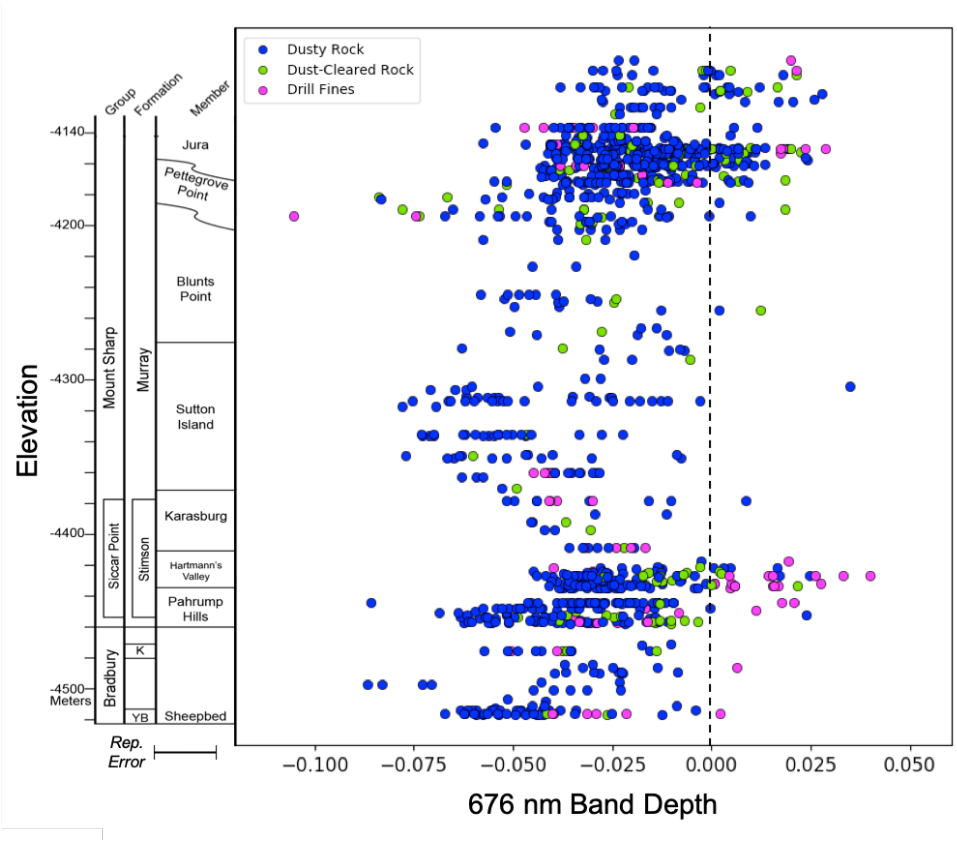

Figure 22. *The 676 nm absorption feature in all dusty and dust cleared rocks, as well as drill fines, from sols 0-2755. The 676 nm band depth is calculated with band shoulders at 640 and 751 nm.*

En route to the Greenheugh Pediment, Curiosity also explored an isolated topographic mound called Western butte. While the rover did not reach the top of the feature to sample the uppermost dark-toned capping unit, it did investigate a float block called Blackwaterfoot on sol 2620 (mcam13763) that had tumbled down from the highest stratigraphic layer. While it was initially hypothesized that the capping unit atop Western butte may match the material capping the Greenheugh Pediment, APXS and ChemCam measurements indicate that Blackwaterfoot

does not match Stimson nor Glen Torridon compositions (Wiens et al., 2020). I found that Blackwaterfoot spectra also do not match Stimson spectra: the float block has a lower NIR slope than most Stimson targets, and a more negative 867 nm band depth than all Stimson targets (Figure 23). Spectra from the Greenheugh Pediment capping unit, however, are spectrally consistent with Stimson spectra (Figure 23).

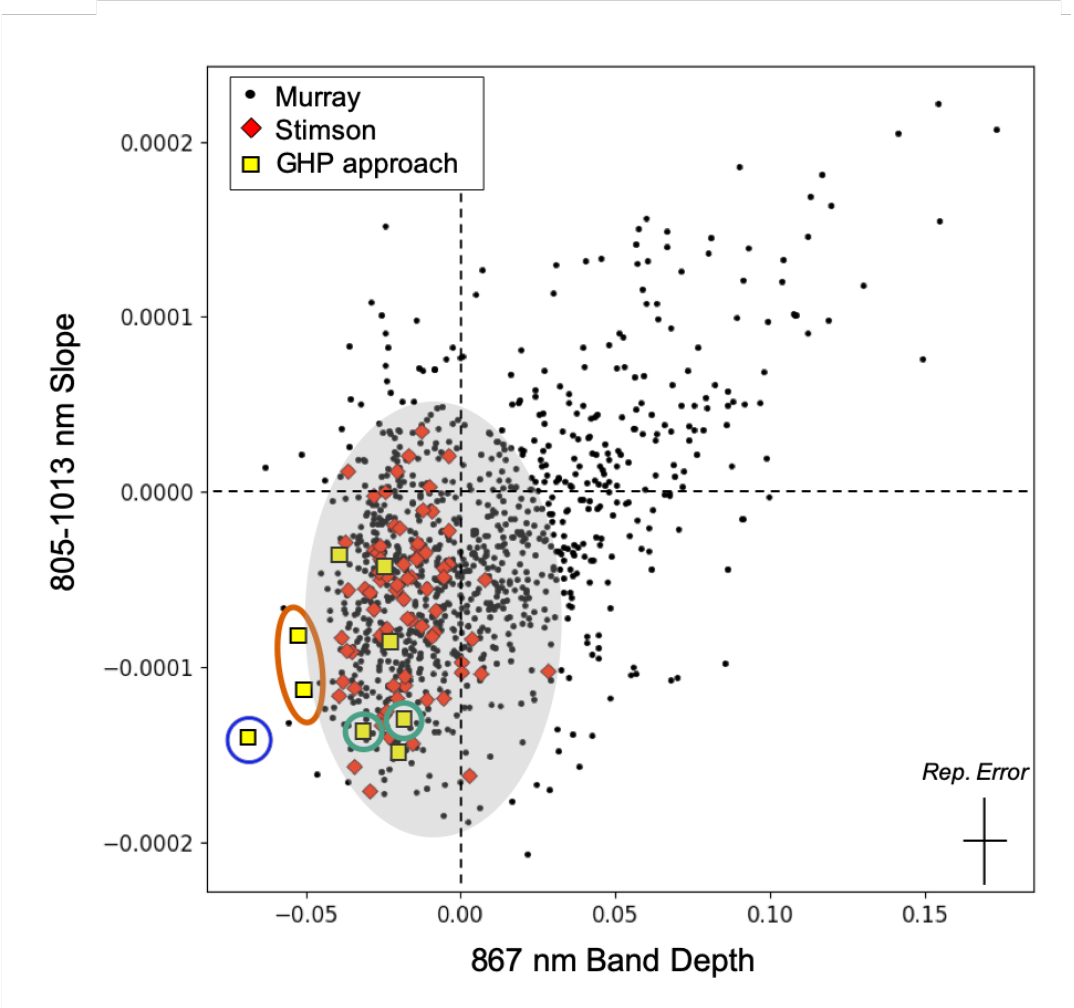

Figure 23. *Many of the spectra acquired of the rocks in the Greenheugh Pediment approach region (GHP approach), including the laminated mudstones directly underlying the capping unit (uncircled yellow squares), are spectrally consistent with Stimson formation rocks. The capping sandstone (circled in teal) is also spectrally consistent with Stimson spectra. Blackwaterfoot (circled in orange), however, plots slightly outside of the range of Stimson values in parameter space. The spectral outlier circled in purple is from bedrock below the pediment in the sol 2609 (mcam13704) observation, and has an unusually negative 867 nm band depth due to the previously discussed 676 nm absorption feature.*

7. Conclusion

Curiosity's exploration of Gale crater has provided innumerable insights into the aqueous history of early Mars, and what has happened to those rocks in the intervening billions of years. Mastcam is an essential tool to explore the landscapes surrounding Curiosity, and provides context for the chemical and mineralogical measurements made in millimeter- to centimeter-scale spots on rock surfaces. My investigation of the spectral trends in the portion of Curiosity's traverse from the start of the Murray formation at Pahrump Hills to the southern edge of the Vera Rubin ridge provides a foundation to explore new trends as they were encountered approaching the Greenheugh Pediment, and these techniques—analyzing the multispectral dataset in its entirety, investigating broad trends and relating them to stratigraphy, and contextualizing chemistry from the rest of the rover's scientific payload—will continue to shape our understanding of geologic history on Mars as Curiosity explores ever upwards. Some key findings are:

1. Dust consistently masks rock spectra, resulting in higher reflectance (especially at longer wavelengths), muted absorption features, and larger 751/445 nm ratios.
2. Float rocks are generally spectrally consistent with proximal in situ outcrop, but spectral outliers often have spectra consistent with iron meteorites.
3. Spectra from drill tailings tend to have lower red-blue slopes and more pronounced absorption features; however, the 867 nm band depth and 805-1012 nm slope tend to be consistent across all target types, and are useful spectral parameters in the dusty rock spectrum to reflect the actual spectral signature of the underlying rock.
4. 867 nm band depth and NIR slope are useful parameters to distinguish Stimson formation from Murray formation; Stimson is more spectrally self-consistent than Murray. Three broad spectral classes can be drawn based on 867 nm band depth and 640/527 nm ratio, dividing lower Murray and Stimson, middle Murray, and VRR targets.
5. ChemCam passive and Mastcam spectra are significantly correlated, and a cross-instrument calibration reveals that while Mastcam's bandpasses are not able to characterize the full extent of Fe-oxide behavior, Mastcam and ChemCam have complementary datasets that together best characterize the alteration and oxidation of the sedimentary sequence.

6. Mastcam spectral variation across Curiosity's traverse reveals that Vera Rubin ridge has much higher variance in several Fe-oxide parameters than any other part of the Murray formation, consistent with a greater magnitude and duration of later stage fluid flow.
7. Greenheugh Pediment capping aeolian sandstone is spectrally constant with Stimson formation, though nearby Western butte caprock targets are spectrally and chemically unique.

The techniques and methodology developed and employed in this study will continue to illuminate the changing environments of Gale crater's past as Curiosity continues to climb Mount Sharp and explore successively younger units. This work also demonstrates the value of frequent and regular multispectral image acquisition. When the Mars 2020 Perseverance rover lands in Jezero crater in 2021, Mastcam-Z (Mastcam's successor) will be used to explore the complex sediments of a delta remnant. Results from Mastcam demonstrate that with frequent and regular full-filter multispectral image acquisition will produce a valuable dataset to investigate local changes in deposition, alteration, and weathering in the delta deposits, providing essential regional context for in situ chemical and mineralogical measurements and informing the developing stratigraphic model from the outset of the mission.

References

Achilles et al., 2019 (in review) Evidence for Multiple Diagenetic Episodes in Ancient Fluvial-Lacustrine Sedimentary Rocks in Gale Crater, Mars.

Bell, J. F., McSween, H. Y., Crisp, J. A., Morris, R. V., Murchie, S. L., Bridges, N. T., ... Soderblom, L. (2000). Mineralogic and compositional properties of Martian soil and dust: Results from Mars Pathfinder. Journal of Geophysical Research: Planets, 105(E1), 1721–1755.

Bell, J. F., Godber, A., McNair, S., Caplinger, M. A., Maki, J. N., Lemmon, M. T., … Deen, R. G. (2017). The Mars Science Laboratory Curiosity rover Mastcam instruments: Preflight and in-flight calibration, validation, and data archiving. *Earth and Space Science*, *4*(7), 396–452. https://doi.org/10.1002/2016EA000219

Bennett, K. A., Fox, V. K., Bryk, A. B., Fedo, C., Vasavada, A. R., Dehouck, E., ... & McAdam, A. (2019). Results from the Curiosity Rover's Traverse Through the Clay-Bearing Glen Torridon Region in Gale Crater. *AGUFM*, *2019*, P33B-01. https://ui.adsabs.harvard.edu/abs/2019AGUFM.P33B..01B/abstract

Bennett, K. A., Rivera-Hernandez, F., Tinker, C., Horgan, B., Fey, D. M., Edwards, C., … Williams, A. J. (in review). Extensive diagenesis revealed by fine-scale features at Vera Rubin ridge, Gale crater, Mars.

Blake, D., Vaniman, D., Achilles, C., Anderson, R., Bish, D., Bristow, T., ... & Downs, R. T. (2012). Characterization and calibration of the CheMin mineralogical instrument on Mars Science Laboratory. Space Science Reviews, 170(1-4), 341-399. https://doi.org/10.1007/s11214-012-9905-1

Bridges, J. C., Schwenzer, S. P., Leveille, R., Westall, F., Wiens, R. C., Mangold, N., … Berger, G. (2015). Diagenesis and clay mineral formation at Gale Crater, Mars. *Journal of Geophysical Research: Planets*, *120*(1), 1–19. https://doi.org/10.1002/2014JE004757

Burns, R. G. (1970). Crystal field spectra and evidence of cation ordering in olivine minerals. *American Mineralogist: Journal of Earth and Planetary Materials*, *55*(9-10), 1608-1632.

Burns, R. G., & Burns, R. G. (1993). *Mineralogical applications of crystal field theory* (Vol. 5). Cambridge university press.

Campbell, J. L., Perrett, G. M., Gellert, R., Andrushenko, S. M., Boyd, N. I., Maxwell, J. A., … Schofield, C. D. M. (2012). Calibration of the Mars Science Laboratory Alpha Particle X-ray Spectrometer. Space Science Reviews, 170(1), 319–340. https://doi.org/10.1007/s11214-012-9873-5

Clark, R. N., & Roush, T. L. (1984). Reflectance spectroscopy: Quantitative analysis techniques for remote sensing applications. *Journal of Geophysical Research: Solid Earth*, *89*(B7), 6329-6340. https://doi.org/10.1029/JB089iB07p06329

Czarnecki, S., Hardgrove, C., Gasda, P. J., Gabriel, T. S., Starr, M., Rice, M. S., ... & Lisov, D. (2020). Identification and Description of a Silicic Volcaniclastic Layer in Gale Crater, Mars, Using Active Neutron Interrogation. Journal of Geophysical Research. Planets, 125(3), Art-No.

Dehouck, E., Cousin, A., Mangold, N., Frydenvang, J., Lasue, J., Meslin, P. Y., ... & Wiens, R. C. (2019). MSL/ChemCam at Glen Torridon: Geochemistry of the Orbitally-Identified Clay-Bearing Unit of Gale Crater. *LPICo*, *2089*, 6125. https://www.hou.usra.edu/meetings/ninthmars2019/pdf/6125.pdf

Edgar, L. A., Gupta, S., Rubin, D. M., Lewis, K. W., Kocurek, G. A., Anderson, R. B., ... & Hardgrove, C. (2018). Shaler: in situ analysis of a fluvial sedimentary deposit on Mars. *Sedimentology*, *65*(1), 96-122. https://doi.org/10.1111/sed.12370

Edgar, L. A., Fedo, C. M., Gupta, S., Banham, S. G., Fraeman, A. A., Grotzinger, J. P., ... & Sun, V. Z. (2020). A lacustrine paleoenvironment recorded at Vera Rubin ridge, Gale crater: Overview of the sedimentology and stratigraphy observed by the Mars Science Laboratory Curiosity rover. *Journal of Geophysical Research: Planets*, e2019JE006307. https://doi.org/10.1029/2019JE006307

Fedo, C., Grotzinger, J. P., Gupta, S., Banham, S., Bennett, K., Edgar, L. A., Edgett, K., Fox, V., Fraeman, A. A., House, C., Lewis, K., Stack, K. M., Rubin, D., Siebach, K. L., Sumner, D., Sun, V., & Vasavada, A. R. (2019). Evidence for persistent, water-rich lacustrine deposition preserved in the Murray formation, Gale crater: A depositional system suitable for sustained habitability. Presented at the Ninth International Conference on Mars. Retrieved from https://www.hou.usra.edu/meetings/ninthmars2019/pdf/6308.pdf

Fedo, C. M., Grotzinger, J. P., Gupta, S., Stein, N. T., Watkins, J., Banham, S., ... & Stack-Morgan, K. (2017). Facies analysis and basin architecture of the upper part of the Murray formation, Gale Crater, Mars. Paper presented at 48th Lunar and Planetary Science Conference, The Woodlands, TX.

Fedo, C. M., Grotzinger, J. P., Schieber, J., Gupta, S., House, C. H., Edgett, K. S., Siebach, K. L., Fraeman, A. A., Edgar, L., Kronyak, R., Kah, L., Gwizd, S. J., & Vasavada, A. (2018). Things are not always as they seem: Detangling intersecting planar and curvi-planar veins and fractures from primary bedding in the Vera Rubin ridge member, Murray formation, Mars. *Geological Society of America Abstracts with Programs*, **50**(3). https://doi.org/10.1130/abs/2018SE-312748

Fraeman, A. A., Arvidson, R. E., Catalano, J. G., Grotzinger, J. P., Morris, R. V., Murchie, S. L., ... & Seelos, K. D. (2013). A hematite-bearing layer in Gale Crater, Mars: Mapping and implications for past aqueous conditions. *Geology*, *41*(10), 1103-1106. https://doi.org/10.1130/G34613.1

Fraeman, A. A., Ehlmann, B. L., Arvidson, R. E., Edwards, C. S., Grotzinger, J. P., Milliken, R. E., … Rice, M. S. (2016). The stratigraphy and evolution of lower Mount Sharp from spectral, morphological, and thermophysical orbital data sets. *Journal of Geophysical Research: Planets*, *121*(9), 1713–1736. https://doi.org/10.1002/2016JE005095

Fraeman, A. A., Johnson, J. R., Arvidson, R. E., Rice, M. S., Wellington, D. E., Morris, R. V., … Vasavada, A. R. (in review). Synergistic ground and orbital observations of iron oxides on Mt. Sharp and Vera Rubin ridge. *JGR Planets.*

Frydenvang, J., Gasda, P. J., Hurowitz, J. A., Grotzinger, J. P., Wiens, R. C., Newsom, H. E., ... & Fisk, M. R. (2017). Diagenetic silica enrichment and late-stage groundwater activity in Gale crater, Mars. *Geophysical Research Letters*, *44*(10), 4716-4724. https://doi.org/10.1002/2017GL073323

Frydenvang, J., Mangold, N., Wiens, R. C., Fraeman, A. A., Edgar, L. A., Fedo, C., ... & Bridges, J. C. (2020). The chemostratigraphy of the Murray formation and role of diagenesis at Vera Rubin ridge in Gale crater, Mars, as observed by the ChemCam instrument. *Journal of Geophysical Research: Planets*, e2019JE006320. https://doi.org/10.1029/2019JE006320

Gabriel, T. S. J., Hardgrove, C., Achilles, C. N., Rampe, E. B., Rapin, W. N., Nowicki, S., … McAdam, M. (in review). On an extensive late groundwater event in Gale crater as indicated by water-rich fracture halos. *AGU Advances.*

Gaffey, S. J., McFadden, L. A., Nash, D., & Pieters, C. M. (1993). Ultraviolet, visible, and near-infrared reflectance spectroscopy: Laboratory spectra of geologic materials. *Remote geochemical analysis: Elemental and mineralogical composition*, *43*, 77.

Gillespie, A. R., Kahle, A. B., & Walker, R. E. (1986). Color enhancement of highly correlated images. I. Decorrelation and HSI contrast stretches. *Remote Sensing of Environment*, *20*(3), 209–235. https://doi.org/10.1016/0034-4257(86)90044-1

Grotzinger, J. P., Gupta, S., Malin, M. C., Rubin, D. M., Schieber, J., Siebach, K., … Wilson, S. A. (2015). Deposition, exhumation, and paleoclimate of an ancient lake deposit, Gale crater, Mars. *Science*, *350*(6257), aac7575. https://doi.org/10.1126/science.aac7575

Grotzinger, J. P., Sumner, D. Y., Kah, L. C., Stack, K., Gupta, S., Edgar, L., ... & Milliken, R. (2014). A habitable fluvio-lacustrine environment at Yellowknife Bay, Gale Crater, Mars. *Science*, *343*(6169), 1242777. https://doi.org/10.1126/science.1242777

Guzewich, S. D., Lemmon, M., Smith, C. L., Martínez, G., de Vicente-Retortillo, Á., Newman, C. E., ... & Harri, A. M. (2019). Mars Science Laboratory observations of the 2018/Mars year 34 global dust storm. *Geophysical Research Letters*, *46*(1), 71-79. https://doi.org/10.1029/2018GL080839

Gwizd, S., Fedo, C., Grotzinger, J., Edgett, K., Rivera-Hernández, F., & Stein, N. (2018). Depositional History of the Hartmann's Valley Member, Murray Formation, Gale crater, Mars. In the 49th Lunar and Planetary Science Conference, Abstract #2150.

Hausrath, E. M., Ming, D. W., Peretyazhko, T. S., & Rampe, E. B. (2018). Reactive transport and mass balance modeling of the Stimson sedimentary formation and altered fracture zones constrain diagenetic conditions at Gale crater, Mars. Earth and Planetary Science Letters, 491, 1-10. https://doi.org/10.1016/j.epsl.2018.02.037

Horgan, B. H. N., Johnson, J. R., Fraeman, A. A., Rice, M. S., Seeger, C., Bell III, J. F., ... & Mangold, N. (2020). Diagenesis of Vera Rubin ridge, Gale crater, Mars from Mastcam multispectral images. https://doi.org/10.1002/essoar.10501380.1

Hurowitz, J. A., Grotzinger, J. P., Fischer, W. W., McLennan, S. M., Milliken, R. E., Stein, N., ... & Fairen, A. G. (2017). Redox stratification of an ancient lake in Gale crater, Mars. *Science*, *356*(6341), eaah6849. https://doi.org/10.1126/science.aah6849

Jacob, S., Wellington, D. F., Bell, J. F., III, Fraeman, A., Sun, V. Z., Johnson, J. R., & Horgan, B. H. N. (2018). Correlating Mastcam Multispectral Data and Rock Morphology to Understand Potential Links Between Ferric Spectral Features Along Vera Rubin Ridge in Gale Crater, Mars. *AGU Fall Meeting Abstracts*, *41*. Retrieved from http://adsabs.harvard.edu/abs/2018AGUFM.P41A..05J

Jacob et al., 2020 (in review) Spectral, Compositional, and Physical Properties of the Upper Murray Formation and Vera Rubin ridge, Gale Crater, Mars

Johnson, J. R., Bell III, J. F., Bender, S., Blaney, D., Cloutis, E., DeFlores, L., ... & Lemmon, M. (2015). ChemCam passive reflectance spectroscopy of surface materials at the Curiosity landing site, Mars. *Icarus*, *249*, 74-92. https://doi.org/10.1016/j.icarus.2014.02.028

Johnson, J. R., Bell III, J. F., Bender, S., Blaney, D., Cloutis, E., Ehlmann, B., ... & Maurice, S. (2016). Constraints on iron sulfate and iron oxide mineralogy from ChemCam visible/near-infrared reflectance spectroscopy of Mt. Sharp basal units, Gale Crater, Mars. *American Mineralogist*, *101*(7), 1501-1514. https://doi.org/10.2138/am-2016-5553

Johnson, J. R., Achilles, C., Bell III, J. F., Bender, S., Cloutis, E., Ehlmann, B., ... & Maurice, S. (2017). Visible/near-infrared spectral diversity from in situ observations of the Bagnold

Dune Field sands in Gale Crater, Mars. Journal of Geophysical Research: Planets, 122(12), 2655-2684. https://doi.org/10.1002/2016JE005187

Johnson, J. R., Bell III, J. F., Bender, S., Cloutis, E., Ehlmann, B., Fraeman, A., ... & Wellington, D. (2018). Bagnold Dunes campaign Phase 2: Visible/near-infrared reflectance spectroscopy of longitudinal ripple sands. *Geophysical Research Letters*, *45*(18), 9480-9487. https://doi.org/10.1029/2018GL079025

Kinch, K. M., Bell III, J. F., Goetz, W., Johnson, J. R., Joseph, J., Madsen, M. B., & Sohl-Dickstein, J. (2015). Dust deposition on the decks of the Mars Exploration Rovers: 10 years of dust dynamics on the Panoramic Camera calibration targets. *Earth and Space Science*, *2*(5), 144-172. https://doi.org/10.1002/2014EA000073

Kronyak, R. E., Kah, L. C., Edgett, K. S., VanBommel, S. J., Thompson, L. M., Wiens, R. C., ... & Nachon, M. (2019). Mineral-filled fractures as indicators of multigenerational fluid flow in the Pahrump Hills member of the Murray formation, Gale crater, Mars. *Earth and Space Science*, *6*(2), 238-265. https://doi.org/10.1029/2018EA000482

Lapotre, M. G., Ehlmann, B. L., Minson, S. E., Arvidson, R. E., Ayoub, F., Fraeman, A. A., ... & Bridges, N. T. (2017). Compositional variations in sands of the Bagnold Dunes, Gale Crater, Mars, from visible-shortwave infrared spectroscopy and comparison with ground truth from the Curiosity rover. *Journal of Geophysical Research: Planets*, *122*(12), 2489-2509. https://doi.org/10.1002/2016JE005133

L'Haridon, J., Mangold, N., Meslin, P. Y., Johnson, J. R., Rapin, W., Forni, O., ... & Le Deit, L. (2018). Chemical variability in mineralized veins observed by ChemCam on the lower slopes of Mount Sharp in Gale crater, Mars. Icarus, 311, 69-86. https://doi.org/10.1016/j.icarus.2018.01.028

Malin, Michal C., Ravine, M. A., Caplinger, M. A., Ghaemi, F. T., Schaffner, J. A., Maki, J. N., … & Jensen, E. H. (2017). The Mars Science Laboratory (MSL) Mast cameras and Descent imager: Investigation and instrument descriptions. *Earth and Space Science*, *4*(8), 506–539. https://doi.org/10.1002/2016EA000252

Mangold, N., Dehouck, E., Fedo, C., Forni, O., Achilles, C., Bristow, T., ... & Le Deit, L. (2019). Chemical alteration of fine-grained sedimentary rocks at Gale crater. *Icarus*, *321*, 619-631. https://doi.org/10.1016/j.icarus.2018.11.004

Mangold, N., Schmidt, M. E., Fisk, M. R., Forni, O., McLennan, S. M., Ming, D. W., … Wiens, R. C. (2017). Classification scheme for sedimentary and igneous rocks in Gale crater, Mars. Icarus, 284, 1–17. https://doi.org/10.1016/j.icarus.2016.11.005

Maurice, S., Wiens, R. C., Saccoccio, M., Barraclough, B., Gasnault, O., Forni, O., ... Vaniman, D. (2012). The ChemCam Instrument Suite on the Mars Science Laboratory (MSL) Rover: Science Objectives and Mast Unit Description. Space Science Reviews, 170(1), 95–166. https://doi.org/10.1007/s11214-012-9912-2

Minitti, M. E., Malin, M. C., Van Beek, J. K., Caplinger, M., Maki, J. N., Ravine, M., ... & Kah, L. C. (2019). Distribution of primary and secondary features in the Pahrump Hills outcrop (Gale crater, Mars) as seen in a Mars Descent Imager (MARDI)"sidewalk" mosaic. *Icarus*, *328*, 194-209. https://doi.org/10.1016/j.icarus.2019.03.005

Morris, R. V., H. V. Lauer Jr., C. A. Lawson, E. K. Gibson Jr., G. A. Nace, & C. Stewart (1985). Spectral and other physicochemical properties of submicron powders of hematite (a-Fe2O3), maghemite (g-Fe2O3), mag- netite (Fe3O4), goethite (a-FeOOH), and lepidocrocite (g-FeOOH), J. Geophys. Res., 90, 3126–3144. https://doi.org/10.1029/JB090iB04p03126

Nachon, M., Mangold, N., Forni, O., Kah, L. C., Cousin, A., Wiens, R. C., ... & Clegg, S. M. (2017). Chemistry of diagenetic features analyzed by ChemCam at Pahrump Hills, Gale crater, Mars. Icarus, 281, 121-136. https://doi.org/10.1016/j.icarus.2016.08.026

Rampe, E. B., Blake, D. F., Bristow, T. F., Ming, D. W., Vaniman, D. T., Morris, R. V., ... & Yen, A. S. (2020). Mineralogy and geochemistry of sedimentary rocks and eolian sediments in Gale crater, Mars: A review after six Earth years of exploration with Curiosity. *Geochemistry*, *80*(2), 125605. https://doi.org/10.1016/j.chemer.2020.125605

Rampe, E. B., Ming, D. W., Blake, D. F., Bristow, T. F., Chipera, S. J., Grotzinger, J. P., ... & Achilles, C. N. (2017). Mineralogy of an ancient lacustrine mudstone succession from the Murray formation, Gale crater, Mars. *Earth and Planetary Science Letters*, *471*, 172-185. https://doi.org/10.1016/j.epsl.2017.04.021

Rapin, W., Ehlmann, B. L., Dromart, G., Schieber, J., Thomas, N. H., Fischer, W. W., ... & Kah, L. C. (2019). An interval of high salinity in ancient Gale crater lake on Mars. *Nature Geoscience*, *12*(11), 889-895. https://doi.org/10.1038/s41561-019-0458-8.

Rice, M.S., J.F. Bell III, E. Cloutis, A. Wang, S. Ruff, M.A. Craig, D.T. Bailey, J.R. Johnson, P.A. de Souza Jr., & W. H. Farrand (2010). Silica-rich deposits and hydrated minerals at Gusev crater, Mars: Vis-NIR spectral characterization and regional mapping, Icarus, 205, 375–395. https://doi.org/10.1016/j.icarus.2009.03.035

Rice, M. S., Reynolds, M., Studer-Ellis, G., Bell III, J. F., Johnson, J. R., Herkenhoff, K. E., ... & Kinch, K. M. (2018). The albedo of Mars: Six Mars years of observations from Pancam on the Mars Exploration Rovers and comparisons to MOC, CTX and HiRISE. *Icarus*, *314*, 159-174. https://doi.org/10.1016/j.icarus.2018.05.017

Rice, M.S. et al. (this issue). Mastcam spectral diversity of rocks and soils in Gale crater, Mars Part I: Results from the Curiosity rover's traverse in the Bradbury Group, sols 0 – 750.

Rivera-Hernández, F., Sumner, D. Y., Mangold, N., Stack, K. M., Forni, O., Newsom, H., ... & Wiens, R. (2019). Using ChemCam LIBS data to constrain grain size in rocks on Mars: Proof of concept and application to rocks at Yellowknife Bay and Pahrump Hills, Gale crater. Icarus, 321, 82-98. https://doi.org/10.1016/j.icarus.2018.10.023

Seelos, K. D., Seelos, F. P., Viviano-Beck, C. E., Murchie, S. L., Arvidson, R. E., Ehlmann, B. L., & Fraeman, A. A. (2014). Mineralogy of the MSL Curiosity landing site in Gale crater as observed by MRO/CRISM. *Geophysical Research Letters*, *41*(14), 4880-4887. https://doi.org/10.1002/2014GL060310

Stack, K. M., Grotzinger, J. P., Lamb, M. P., Gupta, S., Rubin, D. M., Kah, L. C., ... & Rivera-Hernández, F. (2019). Evidence for plunging river plume deposits in the Pahrump Hills member of the Murray formation, Gale crater, Mars. *Sedimentology*, *66*(5), 1768-1802. https://doi.org/10.1111/sed.12558

Sun, V. Z., Stack, K. M., Kah, L. C., Thompson, L., Fischer, W., Williams, A. J., … VanBommel, S. (2019). Late-stage diagenetic concretions in the Murray formation, Gale crater, Mars. *Icarus*, *321*, 866–890. https://doi.org/10.1016/j.icarus.2018.12.030

Stein, N., Grotzinger, J. P., Schieber, J., Mangold, N., Hallet, B., Newsom, H., ... & Cousin, A. (2018). Desiccation cracks provide evidence of lake drying on Mars, Sutton Island member, Murray formation, Gale Crater. Geology, 46(6), 515-518. https://doi.org/10.1130/G40005.1

Sun, V. Z., Stack, K. M., Kah, L. C., Thompson, L., Fischer, W., Williams, A. J., ... & House, C. H. (2019). Late-stage diagenetic concretions in the Murray formation, Gale crater, Mars. *Icarus*, *321*, 866-890. https://doi.org/10.1016/j.icarus.2018.12.030

Viúdez-Moreiras, D., Newman, C. E., de la Torre, M., Martínez, G., Guzewich, S., Lemmon, M., ... & Vicente-Retortillo, A. (2019). Effects of the MY34/2018 global dust storm as measured by MSL REMS in Gale crater. *Journal of Geophysical Research: Planets*, *124*(7), 1899-1912. https://doi.org/10.1029/2019JE005985

Watkins, J. A., Grotzinger, J., Stein, N., Banham, S. G., Gupta, S., Rubin, D., Stack, K., et al. (2016). Paleotopography of erosional unconformity, base of Stimson formation, Gale crater, Mars. Paper presented at 47th Lunar and Planetary Science Conference, The Woodlands, TX.

Wellington, D. F. (2018) Mars in the visible to near infrared: Two views of the Red Planet, (Doctoral dissertation). Retrieved from ASU Library Digital Repository (https://repository.asu.edu/items/50591#embed). Tempe, AZ: Arizona State University.

Wellington, D. F., Bell, J. F., Johnson, J. R., Kinch, K. M., Rice, M. S., Godber, A., ... & Hardgrove, C. (2017). Visible to near-infrared MSL/Mastcam multispectral imaging: Initial results from select high-interest science targets within Gale Crater, Mars. *American Mineralogist*, *102*(6), 1202-1217. https://doi.org/10.2138/am-2017-5760CCBY

Wellington, D. F., Johnson, J. R., Meslin, P. Y., & Bell, J. F. (2018). Iron Meteorite Candidates Within Gale Crater, Mars, from MSL/Mastcam Multispectral Observations. Paper presented at 49th Lunar and Planetary Society Conference, The Woodlands, TX.

Wellington, D. F., Meslin, P. Y., Van Beek, J., Johnson, J. R., Wiens, R. C., Calef, F. J., & Bell, J. F. (2019). Iron Meteorite Finds Across Lower Mt. Sharp, Gale Crater, Mars: Clustering and Implications. Paper presented at 50th Lunar and Planetary Society Conference, The Woodlands, TX.

Wiens, R. C., Edgett, K. S., Stack, K. M., Dietrich, W. E., Bryk, A. B., Mangold, N., ... & Johnson, J. (2020). Origin and composition of three heterolithic boulder-and cobble-bearing deposits overlying the Murray and Stimson formations, Gale Crater, Mars. *Icarus*, 113897. https://doi.org/10.1016/j.icarus.2020.113897

Wiens, R. C., Mangold, N., Forni, O., Anderson, R. B., Gasnault, O., Bryk, A., ... & Frydenvang, J. (2020). First Gale Western Butte Capping-Unit Compositions, and Relationships to Earlier Units Along Curiosity's Traverse. Paper presented at 51st Lunar and Planetary Science Conference, The Woodlands, TX.

Wiens, R. C., Maurice, S., Barraclough, B., Saccoccio, M., Barkley, W. C., Bell, J. F., ... Wong-Swanson, B. (2012). The ChemCam Instrument Suite on the Mars Science Laboratory (MSL) Rover: Body Unit and Combined System Tests. Space Science Reviews, 170(1), 167–227. https://doi.org/10.1007/s11214-012-9902-4

Williams, R. M., Grotzinger, J. P., Dietrich, W. E., Gupta, S., Sumner, D. Y., Wiens, R. C., ... & Forni, O. (2013). Martian fluvial conglomerates at Gale crater. science, 340(6136), 1068-1072. https://doi.org/10.1126/science.1237317

Williams, R. M. E., Malin, M. C., Edgett, K. S., Wiens, R. C., Yingst, R. A., Stack, K. M., ... & Gasnault, O. (2020). Diversity of Float Rocks at Bressay on Vera Rubin Ridge, Gale Crater, Mars. Paper presented at 51st Lunar and Planetary Science Conference, The Woodlands, TX.

Yen, A. S., Ming, D. W., Vaniman, D. T., Gellert, R., Blake, D. F., Morris, R. V., … Thompson, L. M. (2017). Multiple stages of aqueous alteration along fractures in mudstone and sandstone strata in Gale Crater, Mars. *Earth and Planetary Science Letters*, *471*, 186–198. https://doi.org/10.1016/j.epsl.2017.04.033

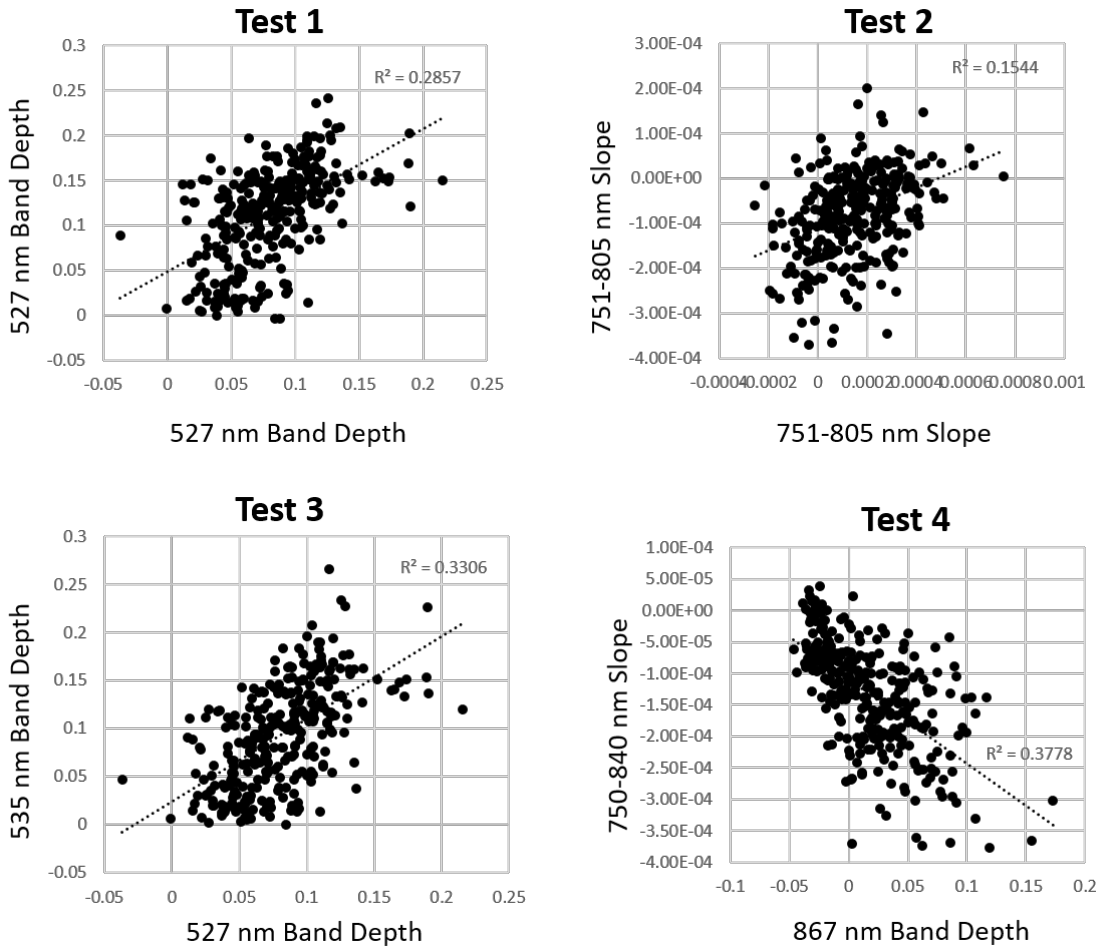

Figure S1. *Linear regression for four covariance tests, with R^2 values reported in Table 3.*

Table S1. All multispectral observations used in this study

Region	Sol	Sequence	Filters	Target	Local True Solar Time	Incidence (deg)	Emission (deg)	Phase (deg)
Pahrump Hills	758	mcam03257	L0-6, R0-6	**Confidence Hills**	12:07:59	4.9	49.3	51.2
Pahrump Hills	762	mcam03273	L0-6, R0-6	**Confidence Hills 2x1**	13:20:12	20.7	44.6	40.7
Pahrump Hills	771	mcam03310	L0-6, R0-6	**Comb Ridge**	11:34:40	9.8	71.8	81.1
Pahrump Hills	773	mcam03347	L0-6, R0-6	**Confidence Hills Dump**	11:13:31	14.0	34.9	45.5
Pahrump Hills	782	mcam03413	L0-6, R0-6	**Confidence Hills Dump 2**	11:42:04	11.0	51.3	53.5
Pahrump Hills	801	mcam03498	L0-6, R0-6	**Garlock 2x1**	12:17:38	14.7	36.5	38.8
Pahrump Hills	803	mcam03505	L0-6, R0-6	**Mendenhall**	12:02:27	14.5	34.3	42.5
Pahrump Hills	807	mcam03538	L0-6, R0-6	**Pelona Ricardo 1x2**	11:44:23	15.6	45.4	59.7
Pahrump Hills	812	mcam03564	L0-6, R0-6	**Mojave**	12:51:49	20.4	39.1	24.4
Pahrump Hills	812	mcam03565	L0-6, R0-6	**Rosamund**	12:54:26	20.8	45.2	35.9
Pahrump Hills	816	mcam03594	L0-6, R0-6	**Topanga**	11:49:06	16.9	67.3	65.5
Pahrump Hills	816	mcam03595	L0-6, R0-6	**Afton Canyon**	11:51:38	16.8	62.0	66.0
Pahrump Hills	816	mcam03596	L0-6, R0-6	**Punchbowl**	11:54:27	16.7	51.9	53.3
Pahrump Hills	822	mcam03618	L0-6, R0-6	**Mescal**	11:22:57	19.7	53.1	71.6
Pahrump Hills	826	mcam03629	L0-6, R0-6	**Puente**	11:35:50	19.0	40.0	59.0
Pahrump Hills	832	mcam03653	L0-6, R0-6	**Pickhandle**	11:11:28	22.1	61.0	83.1
Pahrump Hills	832	mcam03654	L0-6, R0-6	**Goldstone**	11:14:09	21.8	49.7	71.5
Pahrump Hills	837	mcam03675	L0-6, R0-6	**Cowhole Mountain**	11:59:59	19.3	51.9	70.6
Pahrump Hills	845	mcam03762	L0-6, R0-6	**Santa Ana**	12:09:00	20.1	48.0	51.4
Pahrump Hills	855	mcam03777	L0-6, R0-6	**Tecoya**	11:55:11	20.5	43.2	53.7
Pahrump Hills	868	mcam03812	L0-6, R0-6	**Mini Drill Tailings**	12:38:01	22.5	44.1	45.9
Pahrump Hills	872	mcam03816	L1236	**Photom East**	10:25:09	30.6	69.2	82.6
Pahrump Hills	872	mcam03818	L1236	**Photom West 1x2**	10:28:16	30.0	71.3	63.3
Pahrump Hills	872	mcam03820	L1236	**Photom East**	11:25:11	22.1	69.2	69.8
Pahrump Hills	872	mcam03822	L1236	**Photom West 1x2**	11:28:14	21.9	71.3	74.2
Pahrump Hills	872	mcam03823	L1236	**Photom East**	12:25:19	21.4	69.2	56.7
Pahrump Hills	872	mcam03826	L1236	**Photom East**	13:24:56	29.0	69.2	43.5
Pahrump Hills	872	mcam03828	L1236	**Photom West 1x2**	13:28:00	29.5	71.3	98.6
Pahrump Hills	872	mcam03829	L1236	**Photom East**	14:31:23	41.7	69.2	28.5
Pahrump Hills	872	mcam03831	L1236	**Photom West 1x2**	14:34:33	42.4	71.3	113.1
Pahrump Hills	883	mcam03851	L0-6, R0-6	**Mojave2 Drill Tailings**	12:06:50	20.1	41.7	45.5
Pahrump Hills	886	mcam03861	L1236	**Photom East**	14:19:52	39.1	69.2	31.2
Pahrump Hills	886	mcam03863	L1236	**Photom East**	15:17:01	51.3	69.2	18.2
Pahrump Hills	886	mcam03865	L1236	**Photom West 1x2**	15:20:14	52.0	71.3	123.2
Pahrump Hills	886	mcam03866	L1236	**Photom East**	16:48:42	71.9	69.2	2.8
Pahrump Hills	886	mcam03868	L1236	**Photom West 1x2**	16:52:02	72.7	71.3	144.0
Pahrump Hills	889	mcam03873	L0-6, R0-6	**Mojave2 Presieve Dump**	10:26:04	29.9	42.6	68.9
Pahrump Hills	892	mcam03884	L1236	**Photom East**	7:00:28	74.3	69.2	120.9

Pahrump Hills	892	mcam03886	L1236	**Photom West 1x2**	7:03:59	73.5	71.3	44.9
Pahrump Hills	895	mcam03933	L0-6, R0-6	**Mojave2 Postsieve Dump**	11:56:45	19.1	45.7	52.7
Pahrump Hills	909	mcam03977	L0-6, R0-6	**Telegraph Peak Tailings**	11:36:39	18.3	46.6	62.3
Pahrump Hills	914	mcam03996	L1236	**Photom West 1x2**	10:12:07	31.0	71.1	56.0
Pahrump Hills	914	mcam04003	L1236	**Photom West 1x2**	12:37:06	19.0	71.1	85.4
Pahrump Hills	914	mcam04005	L1236	**Photom West 1x2**	15:32:59	54.3	71.1	125.3
Pahrump Hills	914	mcam04007	L1236	**Photom West 1x2**	16:21:05	65.4	71.1	136.4
Pahrump Hills	915	mcam04009	L1236	**Photom West 1x2**	11:35:40	17.6	71.1	72.3
Pahrump Hills	915	mcam04015	L1236	**Photom West 1x2**	13:40:32	29.6	71.1	99.5
Pahrump Hills	915	mcam04017	L1236	**Photom West 1x2**	17:10:43	76.9	71.1	148.0
Pahrump Hills	916	mcam04022	L1236	**Photom West 1x2**	14:52:02	44.9	71.1	115.8
Pahrump Hills	917	mcam04028	L1236	**Photom West 1x2**	7:50:03	62.6	71.1	38.4
Pahrump Hills	929	mcam04084	L0-6, R0-6	**Sanpete**	12:15:14	14.8	59.2	69.9
Pahrump Hills	929	mcam04085	L0-6, R0-6	**Hoskinnini Ouray**	12:17:59	15.0	57.0	70.5
Hartmann's Valley	935	mcam04103	L0-6, R0-6	**Aneth**	11:29:00	15.2	59.8	73.4
Hartmann's Valley	939	mcam04120	L0-6, R0-6	**Hyrum**	12:07:12	12.6	60.6	70.8
Hartmann's Valley	939	mcam04121	L0-6, R0-6	**Telegraph Peak Dump**	12:10:00	12.8	45.7	58.0
Hartmann's Valley	943	mcam04141	L0-6, R0-6	**Little Devil**	12:25:36	13.3	47.7	58.3
Hartmann's Valley	946	mcam04158	L0-6, R0-6	**Amboy Jacumba**	12:28:11	13.2	43.0	53.2
Hartmann's Valley	949	mcam04170	L0-6, R0-6	**Anza Borrego**	11:30:10	12.8	44.5	56.1
Hartmann's Valley	955	mcam04222	L0-6, R0-6	**Telegraph Peak Dump**	11:18:32	13.8	36.6	41.4
Hartmann's Valley	976	mcam04311	L0-6, R0-6	**Albert**	10:55:03	16.8	67.7	67.0
Hartmann's Valley	984	mcam04340	L0-6, R0-6	**Pahrump Stimson**	10:22:09	24.4	95.1	112.6
Hartmann's Valley	990	mcam04372	L0-6, R0-6	**Pinedale**	10:48:43	17.8	43.5	60.9
Hartmann's Valley	994	mcam04398	L0-6, R0-6	**Red Horn 2x1 Rall**	11:34:32	6.3	87.1	91.3
Hartmann's Valley	994	mcam04399	L0-6, R0-6	**Red Sleep 1x2 Rall**	11:45:06	3.7	82.8	82.8
Hartmann's Valley	999	mcam04429	L0-6, R0-6	**Ronan DRT**	11:02:51	14.2	53.2	59.9
Hartmann's Valley	999	mcam04430	L0-6, R0-6	**Seely**	11:05:38	13.5	34.2	46.1
Hartmann's Valley	1000	mcam04444	L1236	**Photom East 2x1**	12:45:11	11.3	68.1	57.0
Hartmann's Valley	1000	mcam04446	L1236	**Photom West 1x2**	12:49:47	12.5	71.2	83.6
Hartmann's Valley	1001	mcam04447	L1236	**Photom East 2x1**	7:15:30	70.8	68.1	137.3
Hartmann's Valley	1001	mcam04449	L1236	**Photom West 1x2**	7:20:50	69.5	71.2	3.7
Hartmann's Valley	1001	mcam04450	L1236	**Photom East 2x1**	10:05:13	28.6	68.1	96.3

Hartmann's Valley	1001	mcam04452	L1236	**Photom West 1x2**	10:10:09	27.3	71.2	43.8
Hartmann's Valley	1001	mcam04453	L1236	**Photom East 2x1**	15:15:27	48.8	68.1	20.5
Hartmann's Valley	1001	mcam04455	L1236	**Photom West 1x2**	15:20:18	50.0	71.2	121.2
Hartmann's Valley	1001	mcam04456	L1236	**Photom East 2x1**	16:15:38	63.8	68.1	8.0
Hartmann's Valley	1001	mcam04458	L1236	**Photom West 1x2**	16:20:21	65.0	71.2	136.1
Hartmann's Valley	1001	mcam04459	L1236	**Photom East 2x1**	17:00:20	74.9	68.1	9.3
Hartmann's Valley	1001	mcam04461	L1236	**Photom West 1x2**	17:05:42	76.3	71.2	147.4
Hartmann's Valley	1001	mcam04465	L0-6, R0-6	**Wallace**	10:53:11	16.6	38.0	53.0
Hartmann's Valley	1003	mcam04467	L1236	**Photom East**	11:28:28	7.9	68.1	76.0
Hartmann's Valley	1003	mcam04469	L1236	**Photom West 1x2**	11:31:27	7.1	71.2	64.1
Hartmann's Valley	1003	mcam04475	L1236	**Photom East**	14:24:58	36.2	68.1	32.8
Hartmann's Valley	1003	mcam04477	L1236	**Photom West 1x2**	14:28:10	37.0	71.2	108.2
Hartmann's Valley	1030	mcam04497	L0-6, R0-6	**Lemhi**	11:28:56	10.5	57.6	56.2
Hartmann's Valley	1030	mcam04498	L0-6, R0-6	**Lowary**	11:32:00	9.9	42.9	46.8
Hartmann's Valley	1032	mcam04510	L0-6, R0-6	**Coombs**	12:03:14	7.6	77.5	73.7
Hartmann's Valley	1032	mcam04511	L0-6, R0-6	**Cottonwood**	12:06:08	7.7	70.9	67.6
Hartmann's Valley	1032	mcam04512	L0-6, R0-6	**Lowary 2**	12:09:16	7.9	51.8	44.1
Hartmann's Valley	1033	mcam04517	L0-6, R0-6	**Thunderbolt**	11:24:51	11.6	49.5	50.6
Hartmann's Valley	1034	mcam04524	L0-6, R0-6	**Thunderbolt**	11:27:43	11.3	47.1	44.8
Hartmann's Valley	1034	mcam04526	L0-6, R0-6	**Seeley**	11:34:11	10.2	46.7	42.6
Hartmann's Valley	1034	mcam04527	L0-6, R0-6	**Thunderbolt**	13:55:16	29.9	47.1	33.2
Hartmann's Valley	1034	mcam04529	L0-6, R0-6	**Thunderbolt**	15:55:11	59.3	47.1	45.5
Hartmann's Valley	1039	mcam04546	L0-6, R0-6	**Pistol R7x1**	12:30:13	11.8	29.2	34.7
Hartmann's Valley	1041	mcam04560	R0-6	**Elk**	11:51:16	9.6	28.4	35.6
Hartmann's Valley	1041	mcam04561	R0-6	**Lamoose**	11:53:14	9.5	23.5	31.7
Hartmann's Valley	1041	mcam04562	L0-6, R0-6	**Mosquito Frog**	11:55:41	9.5	26.5	36.0
Hartmann's Valley	1044	mcam04574	L35	**Apikuni Mountain 4x3**	11:52:59	10.2	84.2	86.4
Hartmann's Valley	1059	mcam04658	L0-6, R0-6	**Ch-paa-qn**	13:58:51	32.4	69.3	48.1
Hartmann's Valley	1062	mcam04672	L0-6, R0-6	**Buckskin Drill Tailings**	13:00:54	20.4	37.3	50.3

Hartmann's Valley	1066	mcam04689	L0-6, R0-6	**Buckskin Presieve Dump**	12:23:47	15.6	32.0	45.9
Hartmann's Valley	1090	mcam04784	L0-6, R0-6	**Buckskin Dump Pile**	11:21:29	20.9	61.4	59.5
Hartmann's Valley	1092	mcam04788	L0-6, R0-6	**Ivanhoe**	12:57:12	23.8	49.6	26.4
Hartmann's Valley	1092	mcam04790	L0-6, R0-6	**Rabbit Hills**	13:04:44	24.9	50.1	25.5
Hartmann's Valley	1092	mcam04791	L0-6, R0-6	**Horseshoe Hills**	13:08:00	25.5	53.7	34.9
Hartmann's Valley	1093	mcam04843	L0-6, R0-6	**Ledger DRT**	12:27:56	20.4	61.5	49.7
Hartmann's Valley	1104	mcam04891	L0-6, R0-6	**Light Toned Ridge**	11:32:10	22.0	96.3	77.9
Hartmann's Valley	1106	mcam04915	L0-6, R0-6	**Winnipeg DRT**	12:35:27	23.0	46.4	24.0
Hartmann's Valley	1110	mcam04942	L0-6, R0-6	**Cody DRT**	12:52:07	25.4	31.3	54.2
Hartmann's Valley	1118	mcam04983	L0-6, R0-6	**Big Sky Mini Start Hole**	12:02:04	23.0	49.4	37.8
Hartmann's Valley	1120	mcam04990	L0-6, R0-6	**Big Sky Full Drill Hole**	12:27:24	24.2	50.0	31.9
Hartmann's Valley	1136	mcam05076	L1236	**Photom East 2x1**	10:59:20	29.3	77.7	86.2
Hartmann's Valley	1136	mcam05078	L1236	**Photom West 1x2**	11:03:29	28.8	71.3	70.9
Hartmann's Valley	1136	mcam05085	L1236	**Photom East 2x1**	12:19:33	25.7	77.7	67.7
Hartmann's Valley	1136	mcam05087	L1236	**Photom West 1x2**	12:23:43	25.9	71.3	87.2
Hartmann's Valley	1138	mcam05088	L1236	**Photom East 2x1**	8:35:10	56.2	77.7	117.5
Hartmann's Valley	1138	mcam05090	L1236	**Photom West 1x2**	8:39:30	55.3	71.3	48.4
Hartmann's Valley	1138	mcam05095	L0-6, R0-6	**Greenhorn Full Drill**	12:46:58	28.0	45.1	22.6
Hartmann's Valley	1138	mcam05096	L0-6, R0-6	**Big Sky Post Sieve Pile**	12:39:30	27.3	36.8	10.2
Hartmann's Valley	1139	mcam05148	L1236	**Photom East 2x1**	13:17:35	31.9	77.7	54.2
Hartmann's Valley	1139	mcam05150	L1236	**Photom West 1x2**	13:21:50	32.6	71.3	99.8
Hartmann's Valley	1140	mcam05159	L1236	**Photom East 2x1**	14:49:35	48.9	77.7	32.8
Hartmann's Valley	1140	mcam05161	L1236	**Photom West 1x2**	14:54:12	49.9	71.3	120.4
Hartmann's Valley	1140	mcam05162	L1236	**Photom East 2x1**	16:05:42	65.5	77.7	15.6
Hartmann's Valley	1140	mcam05164	L1236	**Photom West 1x2**	16:09:47	66.4	71.3	137.6
Hartmann's Valley	1141	mcam05167	L1236	**Photom East 2x1**	17:01:58	78.3	77.7	7.2
Hartmann's Valley	1141	mcam05169	L1236	**Photom West 1x2**	17:06:19	79.3	71.3	150.6
Hartmann's Valley	1142	mcam05174	L1236	**Photom East**	16:11:27	66.8	77.7	11.3
Hartmann's Valley	1142	mcam05177	L1236	**Photom East**	17:02:54	78.5	77.7	6.0

Hartmann's Valley	1143	mcam05178	L1236	**Photom East**	15:06:05	52.5	77.7	25.3
Hartmann's Valley	1160	mcam05245	L0-6, R0-6	**Bogenfels**	12:14:39	27.8	65.6	49.2
Hartmann's Valley	1167	mcam05284	L0-6, R0-6	**Garub**	11:56:24	28.2	44.5	60.7
Hartmann's Valley	1182	mcam05356	L0-6, R0-6	**Hoanib**	12:15:44	29.3	45.5	16.6
Hartmann's Valley	1183	mcam05361	L0-6, R0-6	**Narabeb**	12:07:54	29.2	57.5	46.7
Hartmann's Valley	1183	mcam05362	L0-6, R0-6	**Kubib**	12:10:52	29.2	24.1	41.0
Hartmann's Valley	1204	mcam05546	L0-6, R0-6	**Greenhorn Dump Pile**	13:20:26	35.6	42.2	41.9
Hartmann's Valley	1219	mcam05592	L0-6, R0-6	**Solitaire**	12:32:05	30.8	41.5	72.3
Hartmann's Valley	1222	mcam05603	L0-6, R0-6	**Slangpos**	12:07:47	29.8	86.5	88.0
Hartmann's Valley	1229	mcam05651	R0-6	**Gobabeb Dump A**	12:20:12	29.9	38.6	63.6
Hartmann's Valley	1229	mcam05652	L0-6, R0-6	**Gobabeb Dump B**	12:22:54	30.1	38.4	66.1
Hartmann's Valley	1229	mcam05654	L1236	**Photom Sunrise**	12:30:11	30.4	71.6	78.9
Hartmann's Valley	1229	mcam05655	L1236	**Photom Antisunset**	12:33:24	30.6	71.4	53.3
Hartmann's Valley	1229	mcam05659	L1236	**Photom Sunrise**	13:44:23	39.0	71.6	65.5
Hartmann's Valley	1229	mcam05661	L1236	**Photom Antisunset**	13:49:43	39.8	71.4	36.2
Hartmann's Valley	1229	mcam05662	L1236	**Photom Sunrise**	16:04:25	66.3	71.6	49.4
Hartmann's Valley	1229	mcam05664	L1236	**Photom Antisunset**	16:10:05	67.5	71.4	4.5
Hartmann's Valley	1233	mcam05703	L0-6, R0-6	**Hakos 2x1 Lall 1x1 Rall**	13:39:33	38.1	37.8	43.6
Hartmann's Valley	1234	mcam05705	L0-6, R0-6	**Sanitatis**	12:55:37	32.4	37.6	65.8
Hartmann's Valley	1234	mcam05707	L0-6, R0-6	**Gobabeb Scp2 Dump CD**	13:02:47	33.1	40.3	73.3
Hartmann's Valley	1234	mcam05708	R0-6	**Gobabeb Scp3 Dump EF**	13:05:24	33.4	42.3	74.8
Hartmann's Valley	1234	mcam05714	L1236	**Photom Sunrise**	15:04:06	53.5	71.6	54.3
Hartmann's Valley	1234	mcam05716	L1236	**Photom Antisunset**	15:08:47	54.5	71.5	18.4
Hartmann's Valley	1235	mcam05719	L1236	**Photom Sunrise**	7:39:29	69.6	71.6	140.8
Hartmann's Valley	1235	mcam05721	L1236	**Photom Antisunset**	7:44:29	68.5	71.4	112.3
Hartmann's Valley	1236	mcam05726	L1236	**Photom Sunrise**	9:35:25	45.7	71.6	115.0
Hartmann's Valley	1236	mcam05728	L1236	**Photom Antisunset**	9:40:01	44.8	71.4	90.5
Hartmann's Valley	1237	mcam05731	L1236	**Photom Sunrise**	10:59:56	32.7	71.6	96.8
Hartmann's Valley	1237	mcam05733	L1236	**Photom Antisunset**	11:04:35	32.2	71.4	72.8

Hartmann's Valley	1246	mcam05813	L0-6, R0-6	**Kudis**	12:06:25	28.8	48.4	35.5
Hartmann's Valley	1252	mcam05846	L0-6, R0-6	**Fiskus**	12:50:52	31.0	50.8	65.9
Hartmann's Valley	1253	mcam05852	L0-6, R0-6	**Kuiseb, Dumps R3x1**	13:18:14	34.2	31.6	64.5
Hartmann's Valley	1260	mcam05889	L0-6, R0-6	**Gorob DRT**	12:31:56	28.9	43.4	25.5
Hartmann's Valley	1267	mcam05932	L0-6, R0-6	**Stockdale DRT**	11:52:54	27.2	43.9	37.2
Hartmann's Valley	1273	mcam05953	L0-6, R0-6	**Murray Stimson Contact**	12:32:10	27.7	90.0	103.5
Hartmann's Valley	1274	mcam05965	L0-6, R0-6	**Schwarzrand DRT**	12:40:02	28.2	32.0	28.5
Hartmann's Valley	1276	mcam05989	L0-6, R0-6	**Mirabib Lall 2x1 Rall**	13:22:36	33.2	55.1	40.7
Hartmann's Valley	1280	mcam06017	L0-6, R0-6	**Khomas DRT**	12:34:58	27.2	32.2	56.8
Hartmann's Valley	1289	mcam06076	L0-6, R0-6	**Sesriem Canyon DRT**	12:39:36	26.6	40.8	20.4
Hartmann's Valley	1294	mcam06144	L0-6, R0-6	**Brukkaros DRT**	12:57:52	27.9	30.8	33.9
Hartmann's Valley	1301	mcam06185	L0-6, R0-6	**Bero DRT**	13:23:10	30.8	38.6	37.3
Hartmann's Valley	1309	mcam06229	L0-6, R0-6	**Ruacana**	11:58:55	21.8	88.2	71.8
Hartmann's Valley	1314	mcam06265	L0-6, R0-6	**Gariep**	11:50:41	21.1	59.2	38.9
Hartmann's Valley	1321	mcam06305	L0-6, R0-6	**Lubango Full Drill**	12:11:53	19.9	43.7	26.5
Hartmann's Valley	1326	mcam06328	L0-6, R0-6	**Lubango Tailings Dump**	12:07:58	18.9	43.9	27.5
Hartmann's Valley	1326	mcam06329	L0-6, R0-6	**Rubikon Ebony**	12:10:51	19.0	29.7	17.1
Hartmann's Valley	1328	mcam06371	L0-6, R0-6	**Lubango Postsieve Dmp**	12:04:41	18.5	43.7	27.2
Hartmann's Valley	1333	mcam06395	L0-6, R0-6	**Okoruso Drill Hole**	12:40:14	20.2	46.6	57.8
Hartmann's Valley	1338	mcam06418	L0-6, R0-6	**Okoruso PreSieve Dump**	12:10:32	16.7	40.1	53.3
Hartmann's Valley	1342	mcam06440	L0-6, R0-6	**Kwakwas DRT**	11:49:47	15.9	44.0	58.6
Hartmann's Valley	1344	mcam06447	L0-6, R0-6	**Stampriet Lall 2x1 Rall**	11:47:57	15.5	56.8	48.2
Hartmann's Valley	1349	mcam06476	L0-6, R0-6	**Meob DRT**	11:59:29	14.2	37.5	44.0
Hartmann's Valley	1355	mcam06577	L0-6, R0-6	**Kunjas**	12:43:15	16.9	66.5	83.0
Hartmann's Valley	1355	mcam06578	L0-6, R0-6	**Navachab**	12:46:16	17.4	44.1	48.9
Hartmann's Valley	1356	mcam06589	L1236	**Photom Antisunset 2x1**	8:37:41	52.0	80.1	120.2
Hartmann's Valley	1356	mcam06591	L1236	**Photom Sunset 1x2**	8:41:03	51.1	71.4	29.3
Hartmann's Valley	1356	mcam06592	L1236	**Photom Antisunset 2x1**	11:52:49	12.8	80.1	76.7
Hartmann's Valley	1356	mcam06594	L1236	**Photom Sunset 1x2**	11:56:11	12.7	71.4	73.2

Hartmann's Valley	1356	mcam06595	L0-6, R0-6	**Inamagando**	11:58:47	12.7	46.6	38.5
Hartmann's Valley	1356	mcam06597	L1236	**Photom Antisunset 2x1**	13:52:26	30.8	80.0	49.2
Hartmann's Valley	1356	mcam06599	L1236	**Photom Sunset 1x2**	13:55:48	31.6	71.4	102.2
Hartmann's Valley	1356	mcam06603	L1236	**Photom Antisunset 2x1**	16:04:18	62.3	80.0	21.3
Hartmann's Valley	1356	mcam06605	L1236	**Photom Sunset 1x2**	16:10:53	63.9	71.4	135.3
Hartmann's Valley	1356	mcam06607	L1236	**Photom Antisunset 2x1**	16:49:04	73.2	80.1	15.5
Hartmann's Valley	1356	mcam06609	L1236	**Photom Sunset 1x2**	16:52:31	74.1	71.4	145.5
Hartmann's Valley	1359	mcam06626	L0-6, R0-6	**Okoruso Dump Oudam**	12:44:25	16.4	33.1	43.6
Hartmann's Valley	1363	mcam06671	L0-6, R0-6	**Oudam Drill Hole**	12:45:04	15.9	28.4	38.8
Hartmann's Valley	1366	mcam06683	L0-6, R0-6	**Oudam Presieve Dump**	12:27:58	12.6	37.5	44.5
Hartmann's Valley	1368	mcam06691	L0-6, R0-6	**Aubures**	13:07:27	19.6	31.8	41.0
Hartmann's Valley	1373	mcam06720	L0-6, R0-6	**Uis**	13:10:56	19.8	90.7	81.4
Hartmann's Valley	1382	mcam06774	L0-6, R0-6	**Koes**	11:51:07	7.0	56.1	53.0
Hartmann's Valley	1405	mcam06879	L0-6	**Galo**	13:16:54	19.3	87.5	68.6
Hartmann's Valley	1405	mcam06880	L0-6	**Guri**	13:19:03	19.8	26.1	43.7
Karasburg	1408	mcam06894	L0-6, R0-6	**Tumba**	13:32:33	23.1	44.9	62.9
Karasburg	1417	mcam06946	L0-6, R0-6	**Chibia DRT**	12:39:09	10.0	43.9	41.9
Karasburg	1421	mcam07009	L0-6, R0-6	**Marimba Drill Tailings**	13:23:04	20.9	32.4	49.9
Karasburg	1421	mcam07011	L0-6, R0-6	**Oudam Postsieve Dump**	13:30:13	22.7	32.8	46.4
Karasburg	1425	mcam07034	L0-6, R0-6	**Marimba2 Drill Tailings**	11:37:33	6.8	34.1	27.3
Karasburg	1427	mcam07056	L0-6, R0-6	**Marimba Presieve Dump**	12:51:29	13.6	26.2	31.1
Karasburg	1438	mcam07111	L0-6, R0-6	**Conda DRT**	11:30:16	10.2	53.2	60.3
Karasburg	1445	mcam07152	L0-6, R0-6	**Ganda DRT**	12:40:58	13.5	53.7	53.0
Karasburg	1448	mcam07171	L0-6, R0-6	**Calandala**	12:27:57	11.8	100.5	99.7
Karasburg	1458	mcam07231	L0-6, R0-6	**Marimba Post Sieve**	12:12:16	12.1	46.2	47.7
Karasburg	1459	mcam07236	L0-6, R0-6	**Quela DRT**	12:11:30	12.3	45.2	49.6
Karasburg	1460	mcam07283	L0-6, R0-6	**Cuimba**	11:47:25	12.5	77.1	64.7
Karasburg	1462	mcam07290	L0-6, R0-6	**Ekunha**	11:11:44	17.2	106.6	96.0
Karasburg	1462	mcam07292	L1236	**Photom Antisunset 1x2**	11:19:16	16.0	71.3	78.1
Karasburg	1462	mcam07294	L1236	**Photom Sunset 2x1**	11:23:37	15.4	73.9	71.3
Karasburg	1462	mcam07298	L1236	**Photom Antisunset 1x2**	12:44:21	16.7	71.2	58.1
Karasburg	1462	mcam07300	L1236	**Photom Sunset 2x1**	12:48:42	17.4	73.9	89.7
Karasburg	1462	mcam07302	L1236	**Photom Antisunset 1x2**	14:31:36	39.2	71.2	32.5
Karasburg	1462	mcam07304	L1236	**Photom Sunset 2x1**	14:35:57	40.3	73.8	114.1
Karasburg	1462	mcam07305	L1236	**Photom Antisunset 1x2**	17:01:45	74.8	71.2	4.2

Karasburg	1462	mcam07307	L1236	**Photom Sunset 2x1**	17:06:51	76.0	73.8	149.3
Karasburg	1463	mcam07309	L1236	**Photom Antisunset 1x2**	8:31:18	52.5	71.2	116.0
Karasburg	1463	mcam07311	L1236	**Photom Sunset 2x1**	8:35:45	51.5	73.9	42.4
Karasburg	1463	mcam07315	L1236	**Photom Antisunset 1x2**	15:53:31	58.6	71.2	13.0
Karasburg	1463	mcam07317	L1236	**Photom Sunset 2x1**	15:58:02	59.6	73.8	133.2
Karasburg	1465	mcam07323	L0-6, R0-6	**Quela Drill Tailings**	11:59:33	13.2	45.2	47.2
Karasburg	1467	mcam07337	L0-6, R0-6	**Quela Presieve Dump**	11:36:09	14.7	43.3	35.8
Karasburg	1475	mcam07395	L0-6, R0-6	**Jwaneng**	12:12:53	15.4	47.5	52.5
Karasburg	1475	mcam07396	L0-6, R0-6	**Kopong Munhango**	12:16:54	15.6	54.2	64.2
Sutton Island	1478	mcam07422	L0-6	**Catumbela Caungula**	12:22:12	16.5	47.0	62.8
Sutton Island	1485	mcam07463	L0-6, R0-6	**Serowe**	12:09:15	16.9	53.6	60.3
Sutton Island	1492	mcam07509	L0-6, R0-6	**Sebina DRT + Quela**	12:01:58	17.8	38.5	47.1
Sutton Island	1493	mcam07516	L0-6, R0-6	**Cahama**	12:05:50	17.9	73.6	77.3
Sutton Island	1496	mcam07566	L0-6, R0-6	**Sebina Tailings**	11:40:34	18.8	39.9	47.5
Sutton Island	1498	mcam07582	L0-6, R0-6	**Sebina Presieve Dump**	12:12:46	18.8	42.1	54.1
Sutton Island	1505	mcam07641	L0-6, R0-6	**Thrumcap**	12:04:40	19.3	46.4	62.3
Sutton Island	1505	mcam07642	L0-6, R0-6	**Egg Rock**	12:06:52	19.3	50.5	68.6
Sutton Island	1508	mcam07661	L0-6, R0-6	**Thunder Hole**	11:31:08	20.7	81.7	75.6
Sutton Island	1512	mcam07688	L0-6, R0-6	**Penobscot DRT**	11:34:20	20.8	45.4	65.7
Sutton Island	1520	mcam07741	R046	**Hematite Ridge**	11:56:23	20.3	95.9	106.1
Sutton Island	1524	mcam07770	L0-6, R0-6	**SuttonIsland Manset 2x1**	11:55:47	20.5	47.5	53.8
Sutton Island	1532	mcam07809	L0-6, R0-6	**Precipice DRT**	12:02:21	20.6	46.8	50.0
Sutton Island	1534	mcam07824	L0-6, R0-6	**Sebina Post Sieve Dump**	11:26:57	22.1	42.1	49.7
Sutton Island	1537	mcam07878	L1236	**Photom Antisunset 1x2**	9:39:00	39.5	71.8	94.2
Sutton Island	1537	mcam07880	L1236	**Photom Sunset 1x2**	9:42:52	38.7	71.2	56.3
Sutton Island	1537	mcam07884	L1236	**Photom Antisunset 1x2**	11:25:35	22.1	71.8	72.1
Sutton Island	1537	mcam07886	L1236	**Photom Sunset 1x2**	11:29:27	21.8	71.2	74.4
Sutton Island	1537	mcam07896	L1236	**Photom Antisunset 1x2**	13:10:15	26.6	71.8	49.2
Sutton Island	1537	mcam07898	L1236	**Photom Sunset 1x2**	13:14:07	27.2	71.2	95.6
Sutton Island	1537	mcam07899	L1236	**Photom Antisunset 1x2**	14:57:11	47.2	71.8	25.2
Sutton Island	1537	mcam07901	L1236	**Photom Sunset 1x2**	15:01:03	48.1	71.2	119.0
Sutton Island	1537	mcam07903	L1236	**Photom Antisunset 1x2**	16:44:01	70.9	71.8	1.5
Sutton Island	1537	mcam07905	L1236	**Photom Sunset 1x2**	16:48:00	71.8	71.2	143.0
Sutton Island	1544	mcam07929	L1236	**Photom Antisunset 1x2**	7:40:33	65.3	71.8	115.7
Sutton Island	1544	mcam07931	L1236	**Photom Sunset 1x2**	7:44:50	64.3	71.2	45.8
Sutton Island	1552	mcam07972	L0-6, R0-6	**Western Head**	11:49:03	20.2	52.4	52.2
Sutton Island	1566	mcam07987	L0-6, R0-6	**Old Soaker**	12:31:57	20.4	40.6	60.4
Sutton Island	1566	mcam07988	L0-6, R0-6	**Schooner Head**	12:34:51	20.6	56.1	73.4
Sutton Island	1571	mcam07999	L0-6, R0-6	**Greening Island**	11:34:24	19.3	42.3	50.1
Sutton Island	1587	mcam08091	L0-6, R0-6	**Belle Lake DRT**	11:44:25	16.5	44.3	60.2

Sutton Island	1592	mcam08115	L0-6, R0-6	**Hematite Ridge**	11:56:42	15.3	95.8	105.6
Sutton Island	1592	mcam08116	L0-6, R0-6	**Hematite Ridge**	11:59:25	15.3	96.2	107.9
Sutton Island	1596	mcam08130	L0-6, R0-6	**Parker Bog**	12:02:53	14.6	81.1	94.4
Sutton Island	1603	mcam08177	L0-6, R0-6	**Matagamon**	12:40:18	16.6	42.8	56.0
Sutton Island	1603	mcam08179	L0-6, R0-6	**Scarboro Flumeridge**	12:49:49	18.1	49.2	57.7
Sutton Island	1608	mcam08214	L0-6, R0-6	**Quoddy Quimby**	11:38:08	13.5	34.3	21.3
Sutton Island	1608	mcam08215	L0-6, R0-6	**Jemtland**	11:41:59	13.2	85.1	81.0
Sutton Island	1610	mcam08231	L0-6, R0-6	**Perry**	11:17:57	15.8	38.7	32.5
Sutton Island	1610	mcam08232	L0-6, R0-6	**Spurwink**	11:22:48	15.1	48.9	51.1
Sutton Island	1618	mcam08273	L0-6, R0-6	**Macworth**	11:28:32	13.0	39.1	29.1
Sutton Island	1624	mcam08347	L0-6, R0-6	**Dunn Brook**	11:48:30	9.7	47.1	39.8
Sutton Island	1634	mcam08440	L0-6, R0-6	**North Haven**	12:07:16	7.4	48.5	55.5
Sutton Island	1637	mcam08465	L0-6, R0-6	**Hildreths**	11:12:39	13.4	40.3	36.3
Sutton Island	1652	mcam08558	L0-6, R0-6	**Ogunquit**	10:50:20	17.6	40.6	53.5
Sutton Island	1657	mcam08595	R0456	**VRR Long Baseline 28x1**	10:34:16	21.4	93.4	114.6
Sutton Island	1657	mcam08597	L0-6	**Gts Fivemile**	11:03:07	14.3	63.0	59.5
Sutton Island	1666	mcam08643	L0-6, R0-6	**Moosehead Lake**	11:44:37	3.8	84.2	84.2
Sutton Island	1682	mcam08745	L0-6, R0-6	**Duck Brook Bridge DRT**	11:43:07	5.4	38.1	39.9
Vera Rubin Ridge	1687	mcam08781	L0-6, R0-6	**Cobbosseecontee Lake**	11:42:04	6.4	42.0	40.8
Vera Rubin Ridge	1688	mcam08786	L0-6, R0-6	**Eddie Brook**	12:46:37	12.6	24.0	31.3
Vera Rubin Ridge	1693	mcam08822	L0-6, R0-6	**Bear Island**	12:03:36	6.0	64.5	58.5
Vera Rubin Ridge	1696	mcam08845	L0-6, R0-6	**Mason Point DRT**	10:58:49	16.6	45.8	50.8
Vera Rubin Ridge	1703	mcam08884	L0-6, R0-6	**Broad Cove**	11:20:06	12.8	50.5	53.7
Vera Rubin Ridge	1711	mcam08923	L0-6, R0-6	**White Ledge**	12:06:12	9.8	44.5	36.7
Vera Rubin Ridge	1714	mcam08948	L0-6, R0-6	**Heron Island**	13:03:22	18.9	47.0	36.0
Vera Rubin Ridge	1725	mcam09004	L0-6, R0-6	**Haynes Point**	12:51:30	18.0	46.4	29.9
Vera Rubin Ridge	1727	mcam09015	L0-6, R0-6	**Freeman Ridge**	11:59:06	12.9	93.1	80.2
Vera Rubin Ridge	1728	mcam09026	L0-6, R0-6	**Fernald Point**	11:53:47	13.2	53.2	40.8
Vera Rubin Ridge	1729	mcam09034	L0-6, R0-6	**Mark Island**	12:08:40	13.5	45.0	51.5
Vera Rubin Ridge	1734	mcam09057	L0-6, R0-6	**Northern Neck**	12:07:54	14.4	94.7	81.9
Vera Rubin Ridge	1737	mcam09080	L0-6, R0-6	**Winter Harbor DRT**	12:25:15	16.1	45.5	45.8
Vera Rubin Ridge	1745	mcam09118	L0-6, R0-6	**Jobbies Mingo**	11:53:11	16.4	45.6	49.4
Vera Rubin Ridge	1745	mcam09120	L0-6, R0-6	**Ld VRR**	12:00:00	16.3	96.2	82.8
Vera Rubin Ridge	1749	mcam09142	L0-6, R0-6	**Ile Damour**	12:03:21	17.0	48.6	36.2

Vera Rubin Ridge	1790	mcam09243	L0-6, R0-6	**Zephyr Ledges 2x1**	11:46:36	23.6	52.3	31.8
Vera Rubin Ridge	1797	mcam09276	L0-6, R0-6	**Bois Bubert Stereo**	13:22:03	31.6	40.8	37.1
Vera Rubin Ridge	1805	mcam09310	R0-6	**Toothacher Island**	12:57:53	29.0	55.8	55.2
Vera Rubin Ridge	1807	mcam09325	L0-6, R0-6	**Robinson Rock Gunning**	12:38:56	27.3	54.2	37.5
Vera Rubin Ridge	1812	mcam09351	L0-6, R0-6	**Kemps Folly Stereo**	12:49:53	28.8	58.6	30.2
Vera Rubin Ridge	1814	mcam09364	L0356	**Weymouth Point**	12:16:47	26.6	92.3	68.6
Vera Rubin Ridge	1819	mcam09395	L0-6, R0-6	**Christmas Cove Stereo**	12:22:38	27.3	38.1	23.4
Vera Rubin Ridge	1819	mcam09396	R0-6	**Jaquish Ledge**	12:24:15	27.4	93.5	66.5
Vera Rubin Ridge	1821	mcam09401	L0-6, R0-6	**Mustards Island**	12:31:31	28.0	57.2	36.3
Vera Rubin Ridge	1822	mcam09411	L0-6, R0-6	**Passadumkeag Stereo**	12:06:29	27.1	43.1	22.6
Vera Rubin Ridge	1827	mcam09449	L0-6, R0-6	**Sherwood Tableland**	12:04:44	27.5	54.9	27.4
Vera Rubin Ridge	1833	mcam09493	L0-6, R0-6	**Katberg**	13:38:32	36.9	56.5	35.6
Vera Rubin Ridge	1836	mcam09620	L0-6, R0-6	**VRR Hotazel 4x1**	11:42:07	28.5	88.4	80.2
Vera Rubin Ridge	1837	mcam09630	L0-6, R0-6	**Ecca Lucknow DRT 2x1**	12:08:45	28.3	44.9	17.4
Vera Rubin Ridge	1843	mcam09640	L0-6, R0-6	**Iron Mask Stereo**	12:32:34	29.7	90.0	69.7
Vera Rubin Ridge	1850	mcam09674	L0-6, R0-6	**Zeederberg Stereo**	12:07:02	29.1	65.2	37.3
Vera Rubin Ridge	1850	mcam09675	L0-6, R0-6	**Blinkberg Stereo**	12:09:33	29.1	44.5	20.7
Vera Rubin Ridge	1852	mcam09683	L0356	**VRR Region 7**	12:14:11	29.3	91.0	64.7
Vera Rubin Ridge	1864	mcam09742	R0-6	**Sibasa Drt**	11:54:24	29.6	57.0	33.8
Vera Rubin Ridge	1866	mcam09746	L0-6, R0-6	**VRR Region 6c**	11:38:45	30.1	89.5	60.6
Vera Rubin Ridge	1871	mcam09783	L0-6, R0-6	**Platberg DRT Stereo**	13:06:49	33.9	54.0	32.5
Vera Rubin Ridge	1872	mcam09789	L0-6, R0-6	**Frisco Stereo**	12:01:06	29.7	59.2	47.8
Vera Rubin Ridge	1876	mcam09813	L0-6, R0-6	**Fort Brown DRT**	12:04:02	29.8	45.7	36.9
Vera Rubin Ridge	1876	mcam09814	L0-6, R0-6	**Middleton**	12:05:35	29.8	65.3	55.6
Vera Rubin Ridge	1877	mcam09822	L0-6, R0-6	**Table Mountain 2x1**	12:13:30	30.0	91.4	61.9
Vera Rubin Ridge	1879	mcam09830	L0-6, R0-6	**Natal Stereo**	11:55:32	29.8	33.6	27.2
Vera Rubin Ridge	1885	mcam09853	L0-6, R0-6	**Hexriver Stereo**	11:46:09	30.0	37.4	7.5
Vera Rubin Ridge	1891	mcam09888	L0356	**VRR Region 8**	12:05:00	29.7	89.1	82.9
Vera Rubin Ridge	1893	mcam09909	L0-6, R0-6	**Drakensberg DRT Stereo**	12:36:08	30.9	40.7	30.4

Vera Rubin Ridge	1893	mcam09911	L0-6, R0-6	**Kamden 1x2**	12:44:51	31.6	77.4	53.0
Vera Rubin Ridge	1899	mcam09933	L0-6, R0-6	**Farr 2x1**	12:02:10	29.5	87.4	59.5
Vera Rubin Ridge	1899	mcam09934	L0-6, R0-6	**Muck**	12:05:41	29.5	47.9	44.4
Vera Rubin Ridge	1902	mcam09948	L0-6, R0-6	**Corrie**	12:20:53	29.8	54.6	25.8
Vera Rubin Ridge	1905	mcam09994	L0-6, R0-6	**Oban Laphroaig**	12:58:29	32.6	47.2	20.7
Vera Rubin Ridge	1906	mcam10003	L0-6, R0-6	**Holyrood Haddo House**	12:25:26	29.9	49.3	40.1
Vera Rubin Ridge	1909	mcam10012	L0356	**Lerwick 5x1**	12:07:20	29.1	89.9	71.4
Vera Rubin Ridge	1925	mcam10043	L0-6, R0-6	**Assynt Stereo L1x2 R1x4**	12:13:33	28.3	60.2	36.6
Vera Rubin Ridge	1936	mcam10107	L0-6, R0-6	**Unst Ross of Mull 2x1**	12:51:08	29.9	48.8	19.0
Vera Rubin Ridge	1939	mcam10132	L0-6, R0-6	**Bowmore Stereo L2x1 R3x1**	12:24:44	27.5	84.5	57.1
Vera Rubin Ridge	1940	mcam10139	L0-6, R0-6	**Mallaig Stereo L1x2 R1x3**	11:58:29	26.7	69.8	47.4
Vera Rubin Ridge	1940	mcam10141	L0-6, R0-6	**Clay Unit L3x1 R11x1**	12:18:06	27.1	91.9	67.0
Vera Rubin Ridge	1945	mcam10162	L0-6, R0-6	**Loch Gairloch**	11:53:33	26.3	55.9	33.2
Vera Rubin Ridge	1950	mcam10202	L0-6, R0-6	**Balmedie Stereo 2x1**	12:53:56	28.9	40.9	12.2
Vera Rubin Ridge	1955	mcam10220	L0356	**Kildonan 5x1**	11:53:40	25.1	82.0	105.2
Vera Rubin Ridge	1959	mcam10243	L0-6, R0-6	**Cocksburnpath_hara 2x1**	12:02:41	24.5	59.3	49.0
Vera Rubin Ridge	1964	mcam10267	L0-6, R0-6	**Newmachar DRT**	12:11:35	24.0	40.8	23.4
Vera Rubin Ridge	1964	mcam10269	L0-6, R0-6	**St Kilda**	12:19:06	24.3	39.8	31.4
Vera Rubin Ridge	1964	mcam10270	L0-6, R0-6	**Benbecula**	12:21:05	24.4	48.4	28.1
Vera Rubin Ridge	1967	mcam10287	L0-6, R0-6	**Loch Ba**	12:42:28	25.6	73.3	64.2
Vera Rubin Ridge	1967	mcam10288	L0-6, R0-6	**Lake Orcadie DRT**	12:46:12	26.0	33.9	27.9
Vera Rubin Ridge	1970	mcam10306	L0-6, R0-6	**Ogunquit Dump R2x1**	12:07:10	23.0	38.0	22.6
Vera Rubin Ridge	1978	mcam10342	L0-6, R0-6	**Lake Orcadie Tailings**	11:23:48	23.5	33.5	11.3
Vera Rubin Ridge	1980	mcam10366	L0-6, R0-6	**Lake Orcadie 2 DRT**	12:41:01	23.7	31.8	30.1
Vera Rubin Ridge	1984	mcam10386	L0-6, R0-6	**Lake Orcadie2 Drill Hole**	11:58:28	20.7	31.7	17.9
Vera Rubin Ridge	1986	mcam10410	L0-6, R0-6	**Braemar**	12:08:07	20.5	58.8	39.0
Vera Rubin Ridge	1988	mcam10420	L0356	**Drive Direction**	11:53:55	20.1	86.7	88.7
Vera Rubin Ridge	1996	mcam10459	L0356	**Region 12**	12:30:32	20.0	82.1	85.6
Vera Rubin Ridge	1996	mcam10460	L0-6, R0-6	**Durness Stereo**	12:37:20	20.7	48.6	29.1

Vera Rubin Ridge	1998	mcam10471	L0-6	**Red Hills 4x1**	12:22:59	19.1	77.9	94.4
Vera Rubin Ridge	1998	mcam10473	L0-6, R0-6	**Red Cuillin 3x1**	12:34:23	20.1	72.9	92.5
Vera Rubin Ridge	2000	mcam10487	L0356	**Region 12 3x1**	12:01:16	17.8	78.6	93.6
Vera Rubin Ridge	2002	mcam10505	L0-6, R0-6	**VRR Region 12**	13:05:48	23.9	89.9	81.2
Vera Rubin Ridge	2002	mcam10507	L0-6, R0-6	**Sgurr of Eig & Brora**	13:14:52	25.5	51.8	26.4
Vera Rubin Ridge	2004	mcam10518	L0-6, R0-6	**Mousa Stereo**	11:41:27	17.6	62.9	45.7
Vera Rubin Ridge	2005	mcam10524	L0-6, R0-6	**Port Ellen Stereo**	12:11:05	17.0	53.4	42.3
Vera Rubin Ridge	2005	mcam10530	L12356	**Photom Antisunset 2x1**	12:59:36	22.4	72.1	54.4
Vera Rubin Ridge	2005	mcam10532	L12356	**Photom Sunset 1x2**	13:03:24	23.1	53.3	73.5
Vera Rubin Ridge	2005	mcam10533	L12356	**Photom Antisunset 2x1**	14:33:46	41.8	72.1	31.4
Vera Rubin Ridge	2005	mcam10535	L12356	**Photom Sunset 1x2**	14:37:30	42.6	53.3	95.6
Vera Rubin Ridge	2005	mcam10543	L12356	**Photom Antisunset 2x1**	15:50:13	59.6	72.1	12.8
Vera Rubin Ridge	2005	mcam10545	L12356	**Photom Sunset 1x2**	15:53:57	60.5	53.3	113.8
Vera Rubin Ridge	2005	mcam10546	L12356	**Photom Antisunset 2x1**	16:49:40	73.9	72.1	1.8
Vera Rubin Ridge	2005	mcam10548	L12356	**Photom Sunset 1x2**	16:53:34	74.9	53.3	128.2
Vera Rubin Ridge	2006	mcam10549	L12356	**Photom Antisunset 2x1**	8:19:46	57.2	72.1	121.0
Vera Rubin Ridge	2006	mcam10551	L12356	**Photom Sunset 1x2**	8:23:35	56.3	53.3	26.5
Vera Rubin Ridge	2006	mcam10552	L12356	**Photom Antisunset 2x1**	9:38:18	38.9	72.1	102.8
Vera Rubin Ridge	2006	mcam10554	L12356	**Photom Sunset 1x2**	9:42:04	38.1	53.3	32.4
Vera Rubin Ridge	2006	mcam10555	L12356	**Photom Antisunset 2x1**	11:15:11	20.0	72.1	79.7
Vera Rubin Ridge	2006	mcam10557	L12356	**Photom Sunset 1x2**	11:19:01	19.5	53.3	50.2
Vera Rubin Ridge	2006	mcam10558	L0356	**Region 13 5x1**	11:21:25	19.2	86.1	99.5
Vera Rubin Ridge	2007	mcam10560	L0-6, R0-6	**Stranraer DRT**	11:17:47	19.5	42.8	23.6
Vera Rubin Ridge	2007	mcam10561	L0-6, R0-6	**Burghead Stereo**	11:21:52	18.9	44.5	27.0
Vera Rubin Ridge	2007	mcam10562	L0-6, R0-6	**Walls Peninsula Stereo**	11:24:26	18.6	65.2	47.1
Vera Rubin Ridge	2009	mcam10581	L0-6, R0-6	**Lanark DRT**	11:20:27	18.8	42.6	37.3
Vera Rubin Ridge	2009	mcam10583	L0-6, R0-6	**Stac Fada 2x1/3x3**	11:26:47	18.0	78.7	81.2
Vera Rubin Ridge	2013	mcam10608	L0356	**CRISM Hotspot 5x1**	11:23:28	17.7	73.5	77.4
Vera Rubin Ridge	2013	mcam10610	L0-6	**Galloway 4x1**	11:29:28	17.0	88.7	92.1

Vera Rubin Ridge	2014	mcam10624	L0-6, R0-6	**Lingarabay DRT**	12:50:14	19.5	52.5	37.4
Vera Rubin Ridge	2016	mcam10636	L0-6, R0-6	**Askival Lall 1x3 Rall**	11:48:09	14.8	47.6	52.0
Vera Rubin Ridge	2023	mcam10678	L0-6, R0-6	**Waternish**	12:36:38	15.9	44.7	41.1
Vera Rubin Ridge	2025	mcam10688	L0-6, R0-6	**Cromarty Stereo**	11:38:41	13.7	37.8	29.5
Vera Rubin Ridge	2029	mcam10709	L0-6, R0-6	**Taconite Stereo**	11:46:22	12.2	73.7	75.6
Vera Rubin Ridge	2034	mcam10737	L0-6, R0-6	**Logan**	12:40:55	14.7	75.9	83.2
Vera Rubin Ridge	2036	mcam10747	L0-6, R0-6	**Britt Stereo**	12:11:25	10.5	63.9	53.5
Vera Rubin Ridge	2036	mcam10749	L0-6, R0-6	**Aurora Stereo**	12:18:04	11.1	91.5	91.9
Vera Rubin Ridge	2038	mcam10762	L0-6, R0-6	**Red Cliff 2x1**	14:14:55	35.1	81.6	68.3
Vera Rubin Ridge	2041	mcam10786	L0-6, R0-6	**Barto Lake & Homer Lake**	12:32:19	12.1	54.0	52.6
Vera Rubin Ridge	2043	mcam10810	L0-6, R0-6	**Pigeon River & Bald Eagle Lake 2x1**	11:31:18	11.1	39.1	29.3
Vera Rubin Ridge	2046	mcam10829	L0-6, R0-6	**Mud Lake Stereo**	13:01:35	17.2	48.8	54.2
Vera Rubin Ridge	2050	mcam10863	L0-6, R0-6	**Giants Range and Bilbert**	12:18:26	8.2	58.7	52.1
Vera Rubin Ridge	2050	mcam10865	L0-6, R0-6	**Floodwood DRT Stereo**	12:25:51	9.4	52.6	44.3
Vera Rubin Ridge	2056	mcam10897	L0-6, R0-6	**Duluth DRT stereo**	12:21:29	7.6	58.0	53.2
Vera Rubin Ridge	2059	mcam10916	L0-6, R0-6	**Duluth Drill Stereo**	11:32:18	8.3	55.5	50.4
Vera Rubin Ridge	2081	mcam11061	L0-6, R0-6	**Ambridge Stereo**	13:12:41	18.2	77.8	72.1
Vera Rubin Ridge	2081	mcam11063	L0-6, R0-6	**Duluth Dump Pile Stereo**	13:20:14	20.0	52.5	48.5
Vera Rubin Ridge	2091	mcam11157	L0-6, R0-6	**Caribou lake**	12:21:43	6.4	57.4	57.6
Vera Rubin Ridge	2101	mcam11212	L0-6, R0-6	**Dumbarton_rock**	11:10:11	13.6	56.0	67.4
Vera Rubin Ridge	2110	mcam11271	L0-6, R0-6	**Voyageurs Stereo**	12:58:33	16.6	31.6	34.3
Vera Rubin Ridge	2113	mcam11291	L0-6, R0-6	**Voyageurs Drill Hole**	12:09:53	9.0	28.5	20.9
Vera Rubin Ridge	2120	mcam11351	L0-6, R0-6	**Squrrofeigg Appin Brora**	12:26:12	12.2	31.8	21.8
Vera Rubin Ridge	2122	mcam11363	L0-6, R0-6	**Ailsa Craig Stereo**	12:15:54	11.4	28.2	25.5
Vera Rubin Ridge	2123	mcam11371	L0-6, R0-6	**Ailsa Craig Stereo**	11:37:47	12.2	28.2	17.1
Vera Rubin Ridge	2123	mcam11373	L0356	**Peterhead**	11:43:06	11.7	75.8	69.8
Vera Rubin Ridge	2123	mcam11374	L0356	**Taconite Crater Ejecta**	11:44:25	11.6	73.8	63.5
Vera Rubin Ridge	2124	mcam11377	L0-6, R0-6	**Lamlash Bay**	12:15:24	11.8	21.7	13.3
Vera Rubin Ridge	2132	mcam11431	L0-6, R0-6	**Dobbs Linn Stereo**	12:24:20	14.2	25.0	27.5

Vera Rubin Ridge	2135	mcam11450	L0-6, R0-6	**Stoer DRT**	12:08:44	13.6	24.6	14.6
Vera Rubin Ridge	2138	mcam11468	L0-6, R0-6	**Stoer Drill Tailings**	11:53:20	14.1	24.6	11.6
Vera Rubin Ridge	2147	mcam11535	L0-6, R0-6	**Pentland_Hills**	12:06:47	15.8	77.2	90.1
Vera Rubin Ridge	2147	mcam11536	L0-6, R0-6	**Strontian Stereo**	12:09:49	15.8	38.8	35.9
Vera Rubin Ridge	2153	mcam11593	L0-6, R0-6	**Stoer Portion**	11:42:39	17.2	25.2	14.7
Vera Rubin Ridge	2156	mcam11616	L0356	**Stoer Area**	13:05:38	23.4	50.8	44.4
Vera Rubin Ridge	2160	mcam11630	L0356	**Ben Vorlich 9x4**	11:48:07	17.9	90.9	108.7
Vera Rubin Ridge	2160	mcam11632	L0-6, R0-6	**Tayvallich 2x2**	12:30:18	19.1	47.3	66.3
Vera Rubin Ridge	2160	mcam11633	L0-6, R0-6	**Rosie**	12:35:46	19.7	90.2	108.1
Vera Rubin Ridge	2160	mcam11634	L0-6, R0-6	**Rhinns of Galloway**	12:38:18	20.0	45.7	26.4
Vera Rubin Ridge	2161	mcam11638	L0356	**Drive Direction 5x1**	14:00:50	34.2	90.9	96.1
Vera Rubin Ridge	2163	mcam11652	L0356	**Loch Eriboll 5x1**	12:31:29	19.6	90.7	106.9
Vera Rubin Ridge	2165	mcam11658	L0-6, R0-6	**Great Todday**	12:02:49	18.3	51.4	69.0
Vera Rubin Ridge	2169	mcam11680	L0-6, R0-6	**Inverness DRT**	12:13:49	19.1	26.5	31.1
Vera Rubin Ridge	2169	mcam11681	L0-6, R0-6	**Stoneyburn**	12:16:35	19.2	78.1	74.8
Vera Rubin Ridge	2171	mcam11693	L0-6, R0-6	**Inverness Tailings**	12:04:20	19.0	22.0	24.8
Vera Rubin Ridge	2171	mcam11695	L0-6, R0-6	**Loch Eriboll 2x1//4x1**	12:16:56	19.4	89.5	108.9
Vera Rubin Ridge	2217	mcam11747	L0-6, R0-6	**Inverness**	12:39:51	22.4	26.5	37.5
Vera Rubin Ridge	2222	mcam11774	L0356	**Lake Orcadie Area 2x1**	11:36:47	20.7	75.3	93.7
Vera Rubin Ridge	2225	mcam11791	L0-6, R0-6	**Highfield Drill Tailing**	11:26:28	21.3	43.5	61.6
Vera Rubin Ridge	2229	mcam11824	L0356	**Slate Islands**	11:34:42	20.3	58.4	43.4
Vera Rubin Ridge	2229	mcam11825	L0356	**Loch Ba 3x1**	11:36:06	20.2	41.4	50.5
Vera Rubin Ridge	2231	mcam11838	L0-6, R0-6	**Slate Islands**	11:59:51	19.2	58.3	48.7
Vera Rubin Ridge	2231	mcam11839	L0-6, R0-6	**Little Todday**	12:02:15	19.2	55.0	72.6
Vera Rubin Ridge	2235	mcam11884	L0356	**Falls of Clyde**	11:08:54	22.5	37.8	35.1
Vera Rubin Ridge	2246	mcam12018	L0-6, R0-6	**Highfield Dump**	12:54:52	22.0	42.4	34.9
Vera Rubin Ridge	2247	mcam12027	L0356	**Eshaness Coast 2x1**	12:17:40	17.9	63.3	75.8
Vera Rubin Ridge	2255	mcam12067	L0-6, R0-6	**Woodhill**	12:03:55	16.2	35.7	21.5
Vera Rubin Ridge	2255	mcam12069	L0-6, R0-6	**Newburgh**	12:11:17	16.4	56.8	66.2

Vera Rubin Ridge	2256	mcam12075	L0-6	**Region C 4x1**	11:29:24	17.7	84.4	80.5
Vera Rubin Ridge	2257	mcam12084	L0-6, R0-6	**Rock Hall R2x1**	10:46:44	23.8	45.9	34.1
Vera Rubin Ridge	2259	mcam12088	L0-6, R0-6	**Gometra**	11:22:22	18.0	66.9	83.9
Vera Rubin Ridge	2262	mcam12094	L0-6, R0-6	**Rock Hall Tailings**	11:56:07	15.1	43.9	58.3
Vera Rubin Ridge	2289	mcam12199	L0-6, R0-6	**Rock Hall Dump Pile**	12:02:22	10.0	36.8	51.1
Vera Rubin Ridge	2296	mcam12237	L0-6, R0-6	**Bothwell DRT**	11:31:43	11.0	46.4	59.1
Vera Rubin Ridge	2299	mcam12266	L0-6, R0-6	**Fossil Grove**	11:50:14	8.2	53.0	57.5
Vera Rubin Ridge	2300	mcam12276	L0-6, R0-6	**Linlithgow**	12:17:55	8.9	48.9	49.9
Vera Rubin Ridge	2302	mcam12294	L0-6, R0-6	**Loch_Ness DRT**	11:31:20	10.1	33.9	28.2
Vera Rubin Ridge	2302	mcam12295	L0-6, R0-6	**Loch_Skeen**	11:33:25	9.8	53.2	44.4